CARRIER CONCENTRATION-TUNED PHASE TRANSITIONS IN HIGH-T_c CUPRATES AND PEROVSKITE OXIDE INTERFACES

SHENGWEI ZENG

NATIONAL UNIVERSITY OF SINGAPORE

2014

CARRIER CONCENTRATION-TUNED PHASE TRANSITIONS IN HIGH-T_c CUPRATES AND PEROVSKITE OXIDE INTERFACES

SHENGWEI ZENG

(M.S., XIAMEN UNIVERSITY, P.R.China)

A THESIS SUBMITTED

FOR THE DEGREE OF DOCTOR OF PHILOSOPHY IN SCIENCE

DEPARTMENT OF PHYSICS

NATIONAL UNIVERSITY OF SINGAPORE

2014

DECLARATION

I hereby declare that the thesis is my original work and it has been written by me in its entirety. I have duly acknowledged all the sources of information which have been used in the thesis.

This thesis has also not been submitted for any degree in any university previously.

Shengwei Zeng

1 August 2014

Acknowledgements

I would first like to express my thanks to my supervisor Asst. Prof. Ariando. I thank him for giving me a chance to pursue PhD in NUSNNI-NanoCore. Thank him for bringing me to the field of oxides and providing me the research projects. During four-year research, he shows continuous support, guidance and belief to me. Ariando shows patience towards me when we discuss anything, including my coursework, project and experiment data. This is helpful for bringing me into the work and life in NanoCore, especially during the initial stage of my PhD. Without his support this research work would not at all have possible to realize.

I would like to thank Prof. T. Venky Venkatesan. Thank Venky for his support and assistance in my research. Venky is enthusiastic in research and is knowledgeable. Every meeting with him, he could always give some amazing ideas to explain the current data and perform the future experiments. Venky never stop thinking and learning, he always brings this notebook during the discussion and writes down what he is not clear. Venky's attitude to work inspired me during the PhD period and will continue to inspire me even beyond this period.

I would like to thank Dr. Wang Xiao, Dr. Lv Weiming, Dr. Huang Zhen, Dr. Liu Zhiqi, Dr. Zhao Yongliang, for their continuous assistance in my research and life, especially at the initial stage in NanoCore.

Thank Dr. Jian Linke, Dr. K. Gopinadhan, Dr. Sankar Dhar, Dr. Anil Annadi, Dr. Mallikarjunarao Motapothula, Li Changjian, Dr. Chen Jianqiang, Sun Lin, H. J. Harsan Ma, Amar Srivastava, Dr. Arkajit Roy Barman, Dr. S. Saha, Tarapada Sarkar, Dr. Guo Rui, Michal Marcin Dykas, Han Kun, Zhou Weixiong, Zhang Lingchao, Wan Dongyang, Teo Ngee Hong, Syed Abdulrahim Syed Nizar and all other NanoCore members, for their assistance of my experiments. I am really happy to be colleague of all these wonderful guys.

I would like to thank Prof. Ding Jun, Bao Nina, Dr. T. S. Herng, Zhang Bangmin, Lv Wenlai, Huang Lisen in Department of Materials Science and Engineering for their assistance in my experiments.

I would like to thank Asst. Prof. Andrivo Rusydi, Yin Xinmao in Singapore Synchrotron Light Source for their collaboration with the experiments on our samples. Thank Dr. Yang Ping for his help in XRD measurements.

I would like to thank Assoc. Prof. Chen Wei, Dr. Mao Hongying in Department of Physics for their help in XPS measurements.

Finally and most importantly, I would like to thank my family, my parents, my sister and brothers. Without them, I do not have the courage to pursue my PhD.

Table of Contents

DECLARATION ..... **I**

Acknowledgements ..... **II**

Table of Contents ..... **III**

Abstract ..... **VI**

List of Publications ..... **VIII**

List of Tables ..... **X**

List of Figures ..... **XI**

List of symbols ..... **XVI**

Chapter 1 Introduction **1**

1.1 Chemical and electric field-effect doping 1

1.2 High-Tc superconductors 4

1.2.1 Crystallographic structure 4

1.2.2 Phase diagram 5

1.2.3 Electron-hole asymmetry 7

1.2.4 Quantum phase transition 8

1.3 Perovskite oxide interface 10

1.3.1 ABO_3 perovskite oxides 10

1.3.2 The emergence of the $LaAlO_3/SrTiO_3$ interface 13

1.3.3 Origin of the conductivity in $LaAlO_3/SrTiO_3$ interfaces 13

1.4 Motivation and outline 15

Chapter 2 Sample Preparation and Characterization Techniques **17**

2.1 Film deposition using pulsed laser deposition system 17

2.2 Sample characterization techniques 20

2.2.1 X-ray diffraction 20

2.2.2 Atomic force microscopy 22

2.2.3 Electrical transport measurement 24

2.2.3.1 Resistivity measurement 25

2.2.3.2 Hall effect measurement 27

2.2.3.3 Magnetoresistance measurement 29

2.2.4 Magnetic measurement 30

2.3 Atomic control of substrate surface 30

2.4 Device fabrication 32

Chapter 3 Doping Electrons and Holes into $YBa_2Cu_3O_y$ System 35

3.1 Introduction 35

3.2 Ambipolar conduction in $Y_{0.38}La_{0.62}(Ba_{1.64}La_{0.36})Cu_3O_y$ 37

3.2.1 Experimental procedure 37

3.2.2 Structural characterization using X-ray diffraction 38

3.2.3 Resistivity and Hall-effect measurements 39

3.2.4 'Phase diagram' 46

3.2.5 Summary 47

3.3 The influence of La substitution and oxygen reduction in ambipolar cuprate $Y_{0.38}La_{0.62}(Ba_{2-x}La_x)Cu_3O_y$ 48

3.3.1 Experimental procedure 48

3.3.2 Structural characterization using X-ray diffraction 49

3.3.3 Electrical transport and magnetization measurements 53

3.3.4 Summary 58

3.4 Metallic behaviour in electron-doped $Pr(Ba_{2-x}Pr_x)Cu_3O_y$ 59

3.4.1 Introduction 59

3.4.2 Resistivity and Hall-effect measurements 60

3.4.3 Summary 63

Chapter 4 Superconductor-insulator transition in an electron-doped cuprate $Pr_{2-x}Ce_xCuO_4$ 64

4.1 Introduction 64

4.2 Experimental 67

4.2.1 Field effect device using an ionic liquid as a dielectric material 67

4.2.2 Thin film growth 68

4.2.3 Device preparation 72

4.2.4 Transport measurements 75

4.3 Results of electrical transport measurement 77

4.3.1 Superconductor-insulator transition in an underdoped thin film 77

4.3.2 Phase diagram 81

4.3.3 Hall effects 83

4.3.4 Quantum phase transition 85

4.3.5 Magnetic field-induced superconductor-insulator transitions in superconducting EDLTs 87

4.3.6 Fermionic excitations 90

4.4 Summary 92

Chapter 5 Ionic liquid-assisted electric field effect in oxide heterostructures 93

5.1 Introduction 93
5.2 Patterning of $LaAlO_3/SrTiO_3$ 2DEG 95
5.2.1 Thin film growth 96
5.2.2 Patterning 97
5.2.3 Electrical Transport on the patterned LAO/STO interface 98
5.3 Ionic liquid-assisted electric field effect 100
5.3.1 Measurement setup 100
5.3.2 Interface-surface coupling 102
5.3.3 Gate-induced metal-insulator transition 104
5.3.4 Transistor operation in $LaAlO_3/SrTiO_3$ 2DEG 108
5.3.5 Enhancement of mobility 112
5.3.6 Quantum oscillation 117
5.4 Summary 120
Chapter 6 Summary and future directions 122
6.1 Summary 122
6.1.1 Ambipolar conductivity in YBCO system 122
6.1.2 Superconductor-insulator transition in electron-doped PCCO 123
6.1.3 Field effect in LAO/STO interface 123
6.2 Future directions 124

Bibliography 126

Abstract

In this thesis, we investigated the modulation of charge carriers and the resultant phase transitions in high-T_c cuprate superconductors and perovskite oxide interfaces by chemical and electric field effect doping. Generally, by tuning the carrier densities, evolution from p-type superconductors to n-type metals in a single cuprate system, quasi-continuous superconductor-insulator transition in an electron-doped cuprate and metal-insulator transition in $LaAlO_3/SrTiO_3$ interface were induced.

Investigation of inherent n-p asymmetry (symmetry) in ambipolar cuprates, in which both electrons and holes can be doped into a single parent Mott insulator, is important to reveal the mechanism of high-T_c superconductivity. By doping La and modifying the oxygen composition in $YBa_2Cu_3O_y$ system, ambipolar $Y_{0.38}La_{0.62}(Ba_{2-x}La_x)Cu_3O_y$ thin films were synthesized by pulsed laser deposition system. The structure and electrical transport properties were investigated by X-ray diffraction and physical properties measurement system. It was found that by reducing oxygen composition, the $Y_{0.38}La_{0.62}(Ba_{1.64}La_{0.36})Cu_3O_y$ thin films evolved from hole-doped superconducting phases to electron-doped metallic phases, and showed *n-p* asymmetric transport properties. Ambipolar $Y_{0.38}La_{0.62}(Ba_{2-x}La_x)Cu_3O_y$ thin films with La substitution for Ba of $0.14 \leq x \leq 0.66$ were also synthesized. The resistivity and carrier density as a function of La doing levels were measured. The n-type samples with higher La doping levels showed lower electron density, which could probably be attributed to the charge compensation caused by an increase of oxygen content. This suggests that a balance between the La composition and the achievable lowest oxygen composition is critical to obtain high electron density in YBCO system.

A comparison of carrier density-tuned superconductor-insulator transitions (SITs) between electron- and hole-doped sides is also crucial to understand the origin of cuprates and reveal n-p asymmetry (symmetry) in cuprates. Although SITs induced by changing carrier density in hole-doped cuprates $La_{2-x}Sr_xCuO_4$ and $YBa_2Cu_3O_7$ have been demonstrated, SITs in electron-

doped cuprates have not observed. We performed electric field effect using electronic double layer transistor (EDLT) configuration, to quasi-continuously tune the carrier density in an electron-doped cuprate $Pr_{2-x}Ce_xCuO_4$ and cause a two-dimensional SIT. The low upper critical field in this system allowed us to perform magnetic field-induced SITs in superconducting EDLTs. Finite-size scaling analysis indicates that SITs induced both by electric and magnetic fields are quantum phase transitions and the transitions are governed by percolation effects-quantum mechanical in the former and classical in the latter case. Compared to the hole-doped cuprates the SITs in electron-doped system occurred at critical sheet resistances much lower than the pair quantum resistance $R_Q=h/(2e)^2$=6.45 kΩ, suggesting the existence of fermionic excitations at the insulating side near SITs, as opposed to the preservation of bosons which is suggested in hole-doped cuprates.

Investigating the tuning of the electrical transport properties in $LaAlO_3/SrTiO_3$ (LAO/STO) interface may help to understand the origin of its conductivity and to explore the potential applications. We used electric field effect in EDLT configuration to modulate the transport properties in initially conducting LAO/STO interface. LAO/STO interfaces were patterned into Hall-bar devices by photolithography and using amorphous AlN as hard mask, and it was found that the interfaces were still clean after patterning process. Field effect was performed on the patterned LAO/STO device. The conducting state of the interface was immediately changed by covering ionic liquid, suggesting an interface-surface coupling caused by the polar nature of LAO layer. By applying gate voltages, reversible metal-insulator transitions and field-effect transistor operation in LAO/STO 2DEG were observed. These indicate that the carrier in the interface could be reversible accumulated and depleted. Moreover, enhancement of mobility due to the depletion of carrier density, and Shubnikov-de Hass oscillations of the conductance due to the mobility enhancement were observed. These results suggest that ionic liquid-assisted field effect could be an important avenue to explore quantum phenomena in LAO/STO interfaces.

List of Publications

1 Z.Q. Liu, D.P. Leusink, X. Wang, W.M. Lu, K. Gopinadhan, A. Annadi, Y.L. Zhao, X.H. Huang, S. W. Zeng, Z. Huang, A. Srivastava, S. Dhar, T. Venkatesan and Ariando, "Metal-Insulator Transition in $SrTiO_{3-x}$ Thin Film Induced by Frozen-out Carriers", *Physical Review Letter* **107**, 146802 (2011)**.**

2 Y. L. Zhao, W. M. Lv, Z. Q. Liu, S. W. Zeng, M. Motapothula, S. Dhar, Ariando, Q. Wang and T. Venkatesan, "Variable Range Hopping in TiO2 insulating layers for oxide electronic devices", *AIP Advances* **2**, 012129 (2012).

3 Z. Q. Liu, W. M. Lu, X. Wang, Z. Huang, A. Annadi, S. W. Zeng, T. Venkatesan and Ariando, "Magnetic-field induced resistivity minimum with in-plane linear magnetoresistance of the Fermi liquid in $SrTiO_{3-x}$ single crystals", *Physical Review B* **85**, 155114 (2012).

4 S. W. Zeng, X. Wang, W. M. Lu, Z. Huang, M. Motapothula, Z.Q. Liu, Y.L. Zhao, A. Annadi, S. Dhar, H. Mao, W. Chen, T. Venkatesan and Ariando, "Metallic state in La-doped $YBa_2Cu_3O_y$ thin films with n-type charge carriers", *Physical Reviews B* **86**, 045124 (2012).

5 S. W. Zeng, Z. Huang, X. Wang, W. M. Lu, Z.Q. Liu, B. M. Zhang, S. Dhar, T. Venkatesan, Ariando, "The influence of La substitution and oxygen reduction in ambipolar La-doped $YBa_2Cu_3O_y$ thin films", *Superconductor Science and Technology* **25**, 124003 (2012).

6 Z. Q. Liu, Y. Ming, W. M. Lu, Z. Huang, X. Wang, B. M. Zhang, C.J. Li, K. Gopinadhan, S. W. Zeng, A. Annadi, Y.P. Feng, T. Venkatesan, Ariando, "Tailoring electronic properties of the $SrRuO_3$ thin films in $SrRuO_3/LaAlO_3$ superlattices", *Applied Physics Letters* **101**, 223105 (2012).

7 A. Annadi, Q. Zhang, X. Renshaw Wang, N. Tuzla, K. Gopinadhan, W.M. Lu, A. Roy Barman, Z.Q. Liu, A. Srivastava, S. Saha, Y.L. Zhao, S.W. Zeng, S. Dhar, E. Olsson, B. Gu, S. Yunoki, S. Maekawa, H. Hilgenkamp, T. Venkatesan, Ariando, "Anisotropic two dimensional electron gas at the LaAlO3/SrTiO3 (110) interface", *Nature Communication* **4**, 1838 (2013).

8 Z. Q. Liu, C.J. Li, W.M. Lu, X.H. Huang, Z. Huang, S. W. Zeng, X.P. Qiu, L.S. Huang, A. Annadi, J.S. Chen, J.M.D. Coey, T. Venkatesan, Ariando, Origin of the two dimensional electron gas at $LaAlO_3/SrTiO_3$ interfaces: The role of oxygen vacancies and electronic reconstruction. *Physcal Review X* **3**, 021010 (2013).

9 Z. Huang, X. Wang, Z. Q. Liu, W.M. Lu, S. W. Zeng, A. Annadi, W. L. Tan, X. P. Qiu, Y. L. Zhao, M. Salluzzo, J. M. D. Coey, T. Venkatesan, Ariando, "Conducting channel at $LaAlO_3/SrTiO_3$ heterostructures", *Physcal Reviews B* **88**, 161107(R) (2013).

10 Z. Q. Liu, L. Sun, Z. Huang, C. J. Li, S. W. Zeng, K. Han, W. M. Lü, T Venkatesan, and Ariando, "Dominant role of oxygen vacancies in electrical properties of unannealed LaAlO3/SrTiO3 interfaces"**,** *Journal of Applied Physics* **115**, 054303 (2014).

11 Z. Q. Liu, W. Lu, S. W. Zeng, J. W. Deng, Z. Huang, C. J. Li, M. Motapothula, W. M. Lü, L. Sun, K. Han, J. Q. Zhong, P. Yang, N. N. Bao, W. Chen, J. S. Chen, Y.P. Feng, J. M. D. Coey, T. Venkatesan and Ariando, "Bandgap control of the oxygen-vacancy-induced two dimensional electron gas in $SrTiO_3$", *Advanced Materials Interfaces* **1**, 1400155 (2014)**.**

12 L. S. Huang, J. F. Hu, B. Y. Zong, S. W. Zeng, Ariando and J. S. Chen, "Magnetic properties of L10-FePt/Fe exchange-coupled composite nanodots", *Journal of Physics D: Applied Physics* **47**, 245001 (2014)**.**

13 Xinmao YIN, Shengwei ZENG, G. BASKARAN, Iman SANTOSO, Teguh Citra ASMARA, Xiaojiang, Yu, Caozheng DIAO, Ping YANG, Mark B. H. BREESE, T. VENKATESAN, ARIANDO and Andrivo RUSYDI, "Evolutions of "mid-gap" states and electronic structures of ambipolar cuprates", (submitted).

14 S. W. Zeng, Z. Huang, W. M. Lv, N. N. Bao, K. Gopinadhan, L. K. Jian, T. S. Herng, Y. L. Zhao, P. Yang, J. Ding, T. Venkatesan and Ariando, "Two-dimensional superconductor-insulator quantum phase transitions in an electron-doped cuprate", (submitted).

Conferences

1. *Metallic state in La-doped $YBa_2Cu_3O_y$ thin films with n-type charge carriers*, S. W. Zeng, X. Wang, W. M. Lü, Z. Huang, M. Motapothula, Z. Q. Liu, Y. L. Zhao, A. Annadi, S. Dhar, T. Venkatesan, and Ariando. American Physical Society (APS) March Meeting, February 27-March 2, 2012; Boston, USA.
2. *Doping electrons and holes into La-doped $YBa_2Cu_3O_y$ thin films*, S. W. Zeng, X. Wang, W. M. Lv, Z. Huang, Z. Q. Liu, Y. L. Zhao, A. Annadi, T. Venkatesan, Ariando. International Conference on Materials for Advanced Technologies 2013 (ICMAT 2013), July 1– July 5, 2013, Singapore.
3. *Metallic state in La-doped $YBa_2Cu_3O_y$ thin films with n-type charge carriers*, S. W. Zeng, X. Wang, W. M. Lü, Z. Huang, M. Motapothula, Z. Q. Liu, Y. L. Zhao, A. Annadi, S. Dhar, T. Venkatesan, and Ariando. 5^{th} MRS-S Conference on Advanced Materials, March 20-22, 2012, Singapore.
4. *Liquid-gated superconductor-insulator transition in an electron-doped cuprate*, Shengwei Zeng, Zhen Huang, Nina Bao, Weiming Lv, Zhiqi Liu, T. S. Herng, K. Gopinadhan, Linke Jian, J. Ding, T. Venkatesan, Ariando, American Physical Society (APS) March Meeting, March 3-7, 2014; Denver, USA.

List of Tables

Table 2. 1 Parameters used for thin film growth using pulsed laser deposition. 19

List of Figures

Figure 1.1 Schematic diagram of an electric field effect device 3

Figure 1.2 Crystal structures of (a) $YBa_2Cu_3O_{6+x}$, (b) $La_{2-x}Sr_xCuO_4$, (c) $Nd_{2-x}Ce_xCuO_4$. [33]. 5

Figure 1.3 (a) Phase diagram for the electron-doped $Nd_{2-x}Ce_xCuO_4$ and the hole-doped $La_{2-x}Sr_xCuO_4$ [40]. (b) Phase diagram for the hole-doped $YBa_2Cu_3O_{6+x}$ [32]. 6

Figure 1.4 Phase diagram and possible quantum critical points (●) in cuprates [44]. Dotted line is the temperature T^* below which pseudogap appears. 9

Figure 1.5 Sketch of cubic ABO_3 perovskite structure..... 11

Figure 2.1 Schematic diagram of a pulsed laser deposition setup. 17

Figure 2.2 RHEED intensity oscillations for 15 uc LAO grown on STO (100). Inset is the RHEED pattern for STO (100) before deposition. 19

Figure 2.3 (a) Schematic geometry of X-ray diffraction. (b) ω-scan (c) θ-2θ scan..... 21

Figure 2.4 X-ray diffraction patterns of $YBa_2Cu_3O_y$ for (a) ω-scan (b) θ-2θ scan..... 22

Figure 2.5 Schematic diagram of an atomic force microscopy 23

Figure 2.6 AFM image of $La_{1.85}Sr_{0.15}CuO_4$ on $SrTiO_3$ (100) substrate grown at temperature of 720 ^oC and oxygen pressure of 20 mTorr..... 24

Figure 2.7 (a) Schematic diagram of the van der Pauw measurement geometry. (b) Linear geometry. Yellow rectangular on the sample in (b) indicates metal contact on the sample.... 26

Figure 2.8 Resistivity as a function of temperature for a 250 nm $YBa_2Cu_3O_7$ thin film grown on $LaAlO_3$ (100) substrate. The film was grown at 760 ^oC and oxygen pressure of 200 mTorr, than then post-annealed at 550 ^oC in 1-atm oxygen for 30 min. 27

Figure 2.9 (a) Schematic diagram of Hall effect measurement. (b) Hall resistance as a function of magnetic field for a LAO/STO interface grown on $NdGaO_3$ (110) substrate..... 28

Figure 2.10 *m-T* curve for YBCO thin film grown on LAO substrates..... 30

Figure 2.11 (a) AFM image of a TiO_2-terminated $SrTiO_3$ (100) substrate, (b) Step height profile corresponds to $SrTiO_3$, (c) $LaAlO_3$ (100), (d) $DyScO_3$ (110). 32

Figure 2.12 Schematic overview of pattern transfer from a mask to photoresist on sample.. 33

Figure 2.13 Schematic overview for patterning thin film. (a) Use etching technique (b) Use amorphous insulator as hard mask. 34

Figure 3.1 X-ray diffraction patterns of $Y_{0.38}La_{0.62}(Ba_{1.64}La_{0.36})Cu_3O_y$ thin films. Inset: (005) peaks. 39

Figure 3.2 The in-plane resistivity (ρ_{ab}) as a function of temperature for p-type and n-type $Y_{0.38}La_{0.62}(Ba_{1.64}La_{0.36})Cu_3O_y$ thin films. The samples were labelled by the hole (p) and electron (n) doping at 300 K (per Cu atom), which is obtained by Hall measurement. Inset of panel (d) is the temperature derivative of ρ_{ab} for sample with n=0.087. 41

Figure 3.3 In-plane resistivity of n-type samples as a function of T^2 for the same data shown in Figure 3.2(c)-(d). Solid line is the fitting to the data. Arrows indicate the T where ρ_{ab} deviates from Fermi-liquid behaviour. 42

Figure 3.4 The Hall coefficient R_H of p-type (a) and n-type (b) $Y_{0.38}La_{0.62}(Ba_{1.64}La_{0.36})Cu_3O_y$ thin films as function of temperature..... 44

Figure 3.5 XPS spectra of electron-doped n=0.034 and hole doped p=0.055 thin films at 300 K for Cu 2p core levels..... 45

Figure 3.6 Superconductivity transition temperature T_c, temperature with minimum resistivity T_{min}, c-lattice parameter d and quadratic scattering rate A_2 as a function of carriers density at 300 K. T_{min} is obtained by calculating the derivatives $d\rho_{ab}/dT$ and is the temperature when $d\rho_{ab}/dT=0$. A_2 is obtained from fitting $\rho_{ab}(T)=\rho_0+A_2T^2$ to data within $\rho_{ab} \propto T^2$ region shown in Figure 3.3..... 47

Figure 3.7 (a) XRD θ-2θ patterns of p-type $Y_{0.38}La_{0.62}(Ba_{2-x}La_x)Cu_3O_y$ thin films with x=0.14, 0.36, 0.56. (b) (006) peaks and substrate (002) peaks. (c) c-axis lattice constants, d, as a function of x for p-type samples. 51

Figure 3.8 (006) peaks of thin films and (002) peaks of substrates with x=0.14, 0.36 and 0.56 annealed in oxygen ambient and vacuum. 52

Figure 3.9 Rocking curves on (005) peaks of $Y_{0.38}La_{0.62}(Ba_{2-x}La_x)Cu_3O_y$ thin films with different x for (a) p-type samples and (b) n-type samples. 52

Figure 3.10 Reciprocal space mappings around (a) $(002)_{HL}$, (b) $(002)_{KL}$, (c) $(103)_{HL}$, and (d) $(013)_{KL}$ are indexed in the lattice with a, b, and c for a p-type $Y_{0.38}La_{0.62}(Ba_{2-x}La_x)Cu_3O_y$ thin film with x=0.36. 53

Figure 3.11 The in-plane resistivity (ρ_{ab}) as a function of temperature for p-type $Y_{0.38}La_{0.62}(Ba_{2-x}La_x)Cu_3O_y$ thin films with different x. 54

Figure 3.12 The magnetic moment as a function of temperature for p-type $Y_{0.38}La_{0.62}(Ba_{2-x}La_x)Cu_3O_y$ thin films with different x. 55

Figure 3.13 ρ_{ab} as a function of temperature for n-type $Y_{0.38}La_{0.62}(Ba_{2-x}La_x)Cu_3O_y$ thin films with different x. 56

Figure 3.14 T_c, carrier density at 300 K (n_{300K}) and in-plane resistivity at 300 K (ρ_{300K}) as a function of x for n-type and p-type $Y_{0.38}La_{0.62}(Ba_{2-x}La_x)Cu_3O_y$ thin films. 58

Figure 3.15 (a) In-plane resistivity ρ_{ab} as a function of temperature for $PrBa_2Cu_3O_y$ thin films annealed in oxygen and vacuum. (b) Hall resistance at T=300 K as a function of magnetic field..... 61

Figure 3.16 In-plane resistivity as a function of temperature for electron-doped $Pr(Ba_{2-x}Pr_x)Cu_3O_y$ thin films with different x. 62

Figure 4.1. (a) Schematic diagram of the operation of ionic liquid-based electronic double layer transistors (EDLT). (b) Optical micrograph of a typical device in our study and the measurement circuit. (c) Schematic diagram of the cross section of EDLT device. ……..68

Figure 4.2 (a) Logarithmic-scale resistivity as a function of temperature for $Pr_{2-x}Ce_xCuO_4$ with different Ce doping level x. (b) Linear-scale resistivity-temperature curve for $Pr_{2-x}Ce_xCuO_4$ with optimal Ce doping level x=0.15. 69

Figure 4.3 Critical temperature T_c for $Pr_{2-x}Ce_xCuO_4$ as a function of Ce doping level x. The red-circle data is extracted from ref.[165] and the black square is our data. 70

Figure 4.4. X-ray data for the $Pr_{1.9}Ce_{0.1}CuO_4$ film. The wavelength of X-ray is λ=1.538 Å. (a) Finite-thickness oscillations in the vicinity of the (006) diffraction peak (2θ/ω coupled scan). (b) Finite-thickness oscillations in low-angle X-ray reflectivity (XRR). 70

Figure 4.5. Atomic force microscopy (AFM) image of the surface of ultrathin PCCO/PCO heterostructures. Smooth surface and high crystal quality of thin films is observed with root-mean-square (RMS) roughness of less than 0.44 nm and without granularity and secondary-phase precipitates. 72

Figure 4.6. Schematic overview of the device preparation of (a) single terminated STO substrate, (b) photoresist applied on bare substrate by spin coating, (c) photoresist exposed to

UV light and developed, (d) deposition of *a*-AlN by PLD at room temperature, (e) lift off and removal of photoresist and AlN on top, (f) deposition of PCCO thin film by PLD, the film on *a*-AlN is insulator, (g) second-time photolithography, photoresist applied, (h) photoresist exposed to UV light and developed, (i) deposition of gold by thermal evaporation, (j) lift off and removal of photoresist and gold on top, (k) schematic diagram of the operation of a fabricated EDLT device, and (l) microscopic top view of a fabricated device. 74

Figure 4.7. A small droplet of an ionic liquid was put onto the sample and covered both the conducting channel and the gate electrode. Then, a thin glass plate was put on top of the liquid droplet. 75

Figure 4.8. Resistance as a function of time after applying a gate voltage. (a)V_G=0.5 V (b) V_G=2.2 V..... 76

Figure 4.9. Gate voltage (V_G) dependence of the leakage current (I_G). 77

Figure 4.10. (a) The logarithmic-scale sheet resistance vs temperature (*R*-*T*) curves at various gate voltages for the PCCO sample. (b) The linear-scale *R*-*T* curves at the superconducting region and insulating region near the SIT. (c) The *R*-*T* curves at V_G=3.0 V for various magnetic field applied perpendicular to the CuO_2 plane. 78

Figure 4.11. *R*-*T* curves at higher V_G of 2.69~3.9 V for the PCCO sample. 79

Figure 4.12. (a) R_s-*T* curves for an EDLT device before and after gating experiments. Inset: (b) R_s-*T* curves at various V_G. 81

Figure 4.13. The induced carrier concentration, *x*, as a function of the measured sheet resistance, R_s, at 180 K. 82

Figure 4.14. (a) Critical temperature T_c as a function of carrier concentration *x* for electric field effect and chemical doping. T_c~*x* for chemical doping is extracted from ref.[165] and the highest T_c at *x*=0.15 is normalized to the one from field effect doping. (b) The color plot of the *R*-*T* and *x*. Different colors represent different sheet resistances. The red triangle is T_c... 83

Figure 4.15. Hall resistance (R_{xy}) as a function of magnetic field at T=150 K for different gate voltages..... 85

Figure 4.16. (a) Normalized Hal number (n_H) as a function of gate voltage. (b) n_H as a function of carrier concentration. 85

Figure 4.17. Isotherms of sheet resistance as a function of carrier concentration at *T* ranging from 2.2 to 6 K. Inset: Finite size scaling analysis of the same data. 87

Figure 4.18. (a) *R*-*T* curves at V_G=2.75, 3.0 and 3.2 V, corresponding to the underdoped, optimally doped and overdoped states, respectively. After the measurement of the overdoped curve at V_G=3.2 V, the V_G was reduced to lower value of 2.75 V to obtain the underdoped state, and then measure *R*-*T* curve. (b), (c), (d) are the *R*-*T* curves at various magnetic field for different V_G. The applied magnetic field is perpendicular to the CuO_2 plane. 88

Figure 4.19. Magnetoresistances at (a) V_G=2.75 V, (b) V_G=3.0 V, (c) V_G=3.2 V, corresponding to underdoped, optimally doped and overdoped states (*x*=0.132, 0.15 and 0.153), respectively. The measurements were done at four different *T* points which are lower than the T_c. Insets show the R_s as a function of $|B-B_c|/T^{1/vz}$. The data can be fitted by finite size scaling function assuming *vz*=1.4 for three doping levels. (d) Critical sheet resistance, R_c, normal-state sheet resistance, R_n, and critical magnetic field, B_c, as a function of carrier

concentrations which are corresponding to different V_G. R_c and B_c are the resistances and magnetic fields at the points where the resistance isotherms cross each other. R_n is the resistance obtained at onset of superconductivity and zero B. 89

Figure 5.1 RHEED oscillations during the deposition of 20-uc LAO on a STO (100) substrate. 97

Figure 5.2 (a) Optical micrograph of a Hall-bar pattern on STO using amorphous AlN as the mask. Atomic force microscopy images for (b) 5 uc, (c) 10 uc, (d) 20 uc LAO grown patterned STO substrates, measured in the region of Hall bar channel. 98

Figure 5.3 Sheet resistance R_s as a function of temperature for 6 uc $LaAlO_3/SrTiO_3$ interfaces. The unpatterned sample was obtained by direct deposition of $LaAlO_3$ on bare $SrTiO_3$ substrate. Patterned 1 and Patterned 2 are two Hall-bar devices on a $SrTiO_3$ substrate. 99

Figure 5.4 Sheet carrier density n_s and carrier mobility μ_H as a function of temperature for 6 uc $LaAlO_3/SrTiO_3$ interfaces, for unpatterned and patterned samples. 100

Figure 5.5 (a) Device with a small droplet of silver paint covering the lateral gate electrode. (b) Device with an ionic liquid droplet covering the Hall-bar channel and gate electrode. The measurement circuit is also shown in (a)..... 101

Figure 5.6 Current-voltage (*I-V*) characteristics of a 10 uc LAO/STO Hall-bar device with/without ionic liquid (IL) droplet on top of the LAO surface. The measurements were performed in a two-probe method and at T=300 K. The inset is the microscopic image of the device with ionic liquid on top of the surface. During the measurement, the voltage is applied between the drain and source probes. There is no Al wire connection between the Hall-bar channels and the gate electrodes, in contrast to gating measurement shown in Figure 5.5.. 102

Figure 5.7 Resistance as a function of time for a 10 uc LAO/STO Hall-bar device with ionic liquid droplet on top of LAO surface. The resistance was measured in four-probe method. 103

Figure 5.8 Schematic diagram illustrating the effect of ionic liquid on the polarization field in LAO layer. Due to the accumulation of anions on the LAO surface, the polarization field in the LAO layer covered by ionic liquid is reduced (indicated by small arrow), compared to that without ionic liquid (indicated by larger arrow)..... 104

Figure 5.9 (a) Resistance as a function of gate voltage (V_G) for a 10 uc LAO/STO interface for three scan cycles. (b) Resistance as a function V_G for different temperatures, taken with decreasing V_G. The measurement was performed in a two-probe method and with a scan speed of 25 mV/s. 105

Figure 5.10 Schematic diagram of the band structures of LAO/STO heterostructures. (a) Without IL on top of LAO, (b) V_G>0 V, (c) V_G<0 V..... 106

Figure 5.11 Leakage current (I_G) as a function of gate voltage (V_G). 107

Figure 5.12 (a) Resistance and (b) gate voltage (V_G) as a function of time. 108

Figure 5.13 Gate voltage-dependent I_{DS}-V_{DS} characteristics of a 10uc LAO/STO device at different temperature measured in two-probe method. All data are taken with increasing V_{DS}. The black circles are the co-ordinates (V_p, $I_{DS,sat}$) on the respective curve, which indicate the saturation of I_{DS} with increasing V_{DS}. $I_{DS,sat}$ is the current at V_{DS}=V_P..... 110

Figure 5.14 $(I_{DS})^{1/2}$ as a function of V_G for different temperature, showing quadratic dependence of I_{DS} on V_G in the saturation region. The I_{DS} is taken at V_{DS}=5 V from Figure 5.13. 111

Figure 5.15 Gate voltage-dependent *I-V* characteristics of a 10uc LAO/STO device at T=300 K, measured in four-probe method. 112

Figure 5.16 (a) Sheet resistance R_s as a function of temperature T for 10 uc LAO/STO interface. (b) Sheet carrier density n_s and mobility μ_H as a function of temperature. 113

Figure 5.17 (a) The linear-scale sheet resistance vs temperature (R_s-T) curves at various gate voltages. (b) The logarithmic-scale R_s-T curves at low temperature. The black square is the data without ionic liquid (IL) on top of the sample. 114

Figure 5.18 The n_s (a) and μ_H (b) as a function of temperature at various V_G. Inset of (a) is the n_s at 180 K as a function of V_G. The black square is the data without IL on top of the sample. 116

Figure 5.19 (a) The n_s and μ_H as a function of V_G at 2 K. The data for sample without IL is also shown. (b) μ_H as a function of n_s 117

Figure 5.20 Liquid-gated modulation of the Shubnikov-de Hass oscillations. (a) Variation of resistance $\Delta R=R(B)-R(0)$ as a function of magnetic field B. (b) Numerical derivative dR/dB as a function of the inverse of magnetic field. The dash line indicates the shift of the main oscillation peak. 118

Figure 5.21 Temperature dependence of the SdH oscillations at V_G=0 V. (a) Sheet resistance as a function of magnetic field for different temperatures. (b) Oscillatory component of the sheet resistance as a function of the inverse of magnetic field. (c) The amplitude of the oscillation at B=8.25 T as a function of temperature. The black squares are the experimental data and the red curve is the fitting line. 119

Figure 5.22 Hall resistance R_H as a function of magnetic field B for V_G from 3 to -1.5 V (a) and from 1 to -0.4 V (b). The black line in (a) is guide for eye, to indicate nonlinear Hall effect. The black square is the data without ionic liquid on top of the sample..... 120

List of symbols

B	Magnetic field
M	Magnetization
K	Kelvin
e	elementary charge
MR	Magnetoresistance
R	Resistance
R_s	Sheet resistance
R_c	Critical sheet resistance
R_Q	Pair quantum resistance
R_H	Hall coefficient
ρ	Resistivity
ρ_{ab}	In-plane resistivity
±	Conductivity
T	Temperature
T_c	Critical temperature
T_{min}	Temperature with minimum resistivity
I	Current
V	Voltage
V_G	Gate voltage
μ_H	Mobility
n_s	Sheet carrier density
d	lattice constant
uc	Unit cell
P_{O2}	Oxygen partial pressure
PLD	Pulsed laser deposition
PPMS	Physical properties measurement system
SQUID	Superconducting quantum interference device
XRD	X-ray diffraction

Chapter 1 Introduction

1.1 Chemical and electric field-effect doping

Modulating the charge carriers in a material could cause the change of electrical properties and the resultant phase transitions such as insulator to semiconductor, insulator to metal or superconductor transitions. The usual method to introduce charge carriers into a parent material is chemical doping, in which one element in the material is partially substituted by another which possesses different valence states. This method has been widely used in semiconductors such as Si, GaAs, GaN and ZnO [1]. For example, doping charge carriers in quadrivalent Si could be induced using pentavalent P (phosphorus) and trivalent B (boron). For the P doping, since P has 5 outer electrons and Si has 4 outer electrons, P substitution for Si leaves one electron free and it serves as a negative charge carrier. At this doping state, Si is an n-type or electron-doped semiconductor. In contrast, since B has 3 outer electrons, B substitution for Si leave one hole (electron vacancy) free. Electrons can move and sit at the hole sites, so that the holes are mobile and move in the opposite direction to the movement of the electrons. In this case, the holes serve as positive charge carriers and Si is p-type or hole-doped semiconductor. Electronic and optoelectronic devices based on n-type and p-type semiconductors have been an important part of modern industries and have changed many aspects of our lives.

Chemical doping has also played an essential role in complex oxides such as high-T_c cuprate superconductors and manganite oxides, since it could cause new phase transitions from the parent compounds [2-4]. For example, in cuprate oxide $La_{2-x}Sr_xCuO_4$ (LSCO), Sr^{2+} substitution for La^{3+} in parent compound La_2CuO_4 will induce holes and thereby the change of LSCO from Mott insulator to high-T_c superconductor and then normal metal [2]. Right now, cuprates hold the highest record (~164 K) of critical temperature among all the superconductors. In manganite oxide $La_{1-x}Sr_xMnO_3$ (LSMO), Sr^{2+} substitution for La^{3+} in

$LaMnO_3$ will cause the change of LSMO from antiferromagnetic insulator to magnetic metal [3, 4].

Even though chemical-doping method is very successful, it has some drawbacks. It is not tunable, which means that for each doping level, a new sample must be synthesized. This causes difficulty in the studies in which quasi-continuous modulation of carrier density is required, such as superconductor-insulator transition. Moreover, element substitution induces disorder or alters the level of disorder in a material. In some cases, the difference of ion radii between two elements is large, and thus, the solubility very small. This may cause local inhomogeneity or mixed phases if the element is substituted at large ratio.

Electric field-effect doping is another method for the introduction of charge carriers [5, 6]. Compared with chemical doping, field-effect doping has some advantages such as it is reversible, quasi-continuous and structure-fixed. Generally, in a field-effect device, a dielectric insulator is grown on top of the thin film (in some cases the dielectric insulator is used as substrates for the deposition of thin films), as is shown in Figure 1.1. When an external electric field is applied to the dielectric insulator, the insulator is polarized and it can attract or repel charge carrier in the thin film. This will create a thin charge accumulation or depletion layer at the surface of thin film. By controlling the gate voltage (electric field), the carrier density of thin film can be modified as finely as desired. The conventional dielectric materials in this field are SiO_2, high-dielectric constant materials such as Al_2O_3, HfO_2 and $SrTiO_3$ and ferroelectric oxides such as $Pb(Zr,Ti)O_3$ (PZT). Using these conventional dielectric materials, electric field has been applied to modify the carrier densities and the resultant transport properties in complex oxide such as cuprate superconductor [5-7] and manganite oxides [8]. Moreover, electric field effect has also been applied to control the carrier density of two-dimensional electron gas in interfaces or heterostructures, which is not accessible by chemical doping. For example, electric field has been used to tune the carrier density to control the ground state in $LaAlO_3/SrTiO_3$ interfaces [9, 10] and to control the quantum transports in ZnMgO/ZnO heterostructures [11].

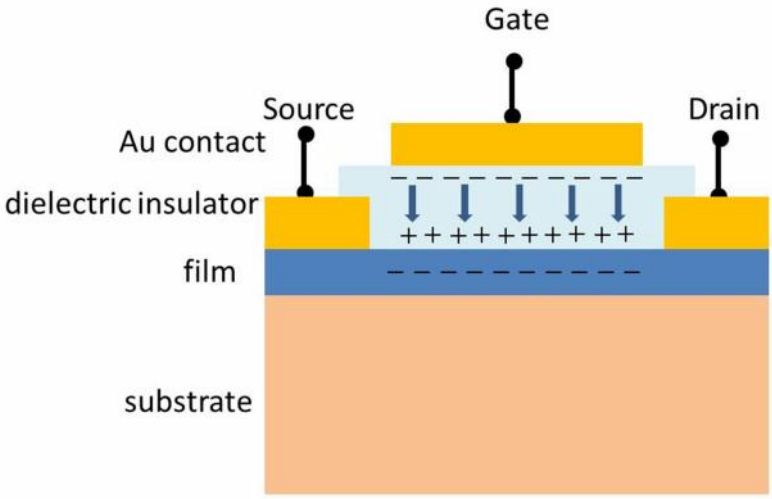

Figure 1.1 Schematic diagram of an electric field effect device

The carrier density obtained by field-effect doping using conventional dielectric materials, however, is far from what is expected to induce superconductivity in non-superconducting materials, due to the relatively low dielectric constants. Therefore, this method has been limited only to the slight modulation of the critical temperature of cuprate superconductors [6]. Recently, using ionic liquids and polymer electrolytes as the dielectric materials in electronic double layer transistors (EDLTs), it has been shown that the carrier density induced by field effect could be as high as 10^{15} cm^{-2} [12, 13], at which many of the interesting physical properties occur in complex oxides. Owing to the change of the large amount of carrier densities, EDLT have been used to induce insulator-to-metal transition in ZnO [12], induce superconductivity in $SrTiO_3$, ZrNCl, $KTaO_3$ and MoS_2 [14-17], induce room temperature ferromagnetism in Co-doped TiO_2 [18], control the electronic phases in manganite [19, 20], delocalize bulk carrier and suppress the metal-to-insulator transition in VO_2 [21, 22] and induce superconductor-insulator transition in hole-doped cuprates $La_{2-x}Sr_xCuO_4$ and $YBa_2Cu_3O_{7-x}$ [23-26]. These suggest the importance of ionic liquid-assisted electric field effect in charge doping both from fundamental and applied perspectives.

1.2 High-Tc superconductors

1.2.1 Crystallographic structure

The discovery of the cuprate superconductor in 1986 was considered as a milestone in the history of superconductors [27]. It was the first material system which possessed a critical temperature (T_c) higher than the boiling point (77 K) of liquid Nitrogen [28] and held the highest record (~164 K) of T_c among all the superconductors [29]. There are several families of cuprate superconductors, but they have a similar crystallographic structure: layered structure with a stacking sequence of perovskite-like copper-oxide (CuO_2) layers and charge-reservoir blocks. Figure 1.2(a) shows the crystal structure of a typical cuprate $YBa_2Cu_3O_{6+x}$ (YBCO). There are two CuO_2 planes forming two CuO_5 pyramids with apical oxygens in the middle of the unit cell, and BaO and CuO layers at the two sides. It is widely accepted that charge carriers move within CuO_2 planes, and the other layers serve as charge reservoirs to dope carriers onto the CuO_2 planes. The CuO_2 planes are weakly coupled and determine the conducting and superconducting properties of cuprates. In $YBa_2Cu_3O_{6+x}$, the structure and physical properties depend considerably on the oxygen content in CuO chains. At $x\approx1$, YBCO is in an orthorhombic phase with lattice parameters of a=3.82 Å, b=3.88 Å and c=11.68 Å, and it has highest T_c of ~90 K [30, 31]. With decreasing x, b decreases, a and c increase, and the structures change from orthorhombic phase to tetragonal phase at $x\leq0.4$. At x=0, all the oxygen in CuO chains are removed out of the compound and the lattice parameters at this state are a=b=3.86 Å and c=11.82 Å [30, 31]. Meanwhile, carrier density in CuO_2 plane and T_c go down with decreasing x, and the metallic phase transforms into the antiferromagnetic insulating phase at $x\leq0.4$ [32], as is shown in Figure 1.3.

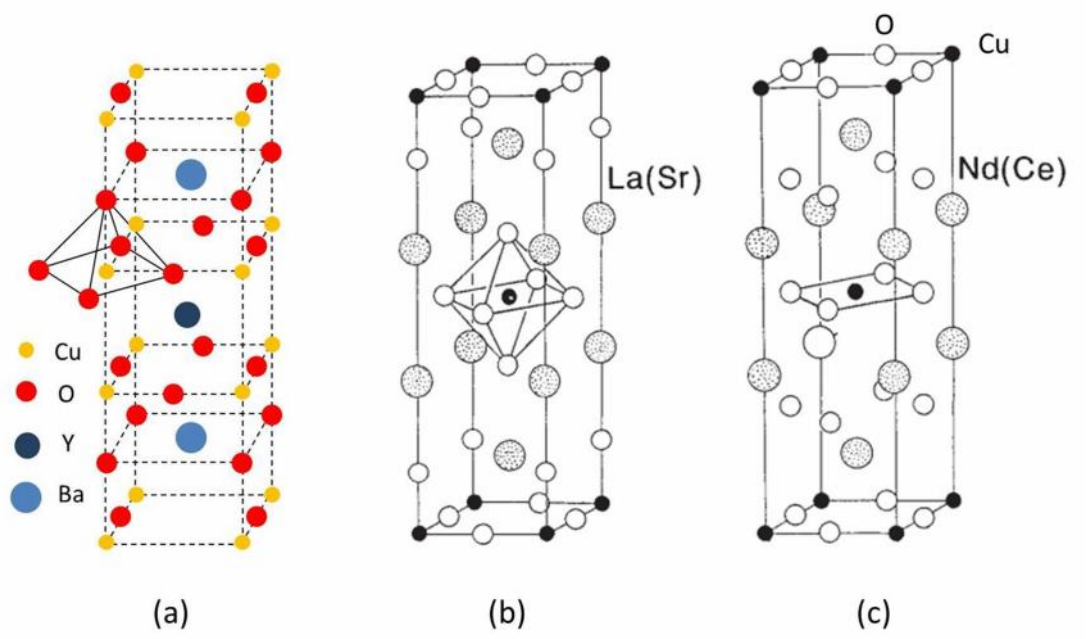

Figure 1.2 Crystal structures of (a) $YBa_2Cu_3O_{6+x}$, (b) $La_{2-x}Sr_xCuO_4$, (c) $Nd_{2-x}Ce_xCuO_4$. [33]

Figure 1.2(b) and (c) shows the crystal structures of 214-type cuprates $La_{2-x}Sr_xCuO_4$ (LSCO) and $Nd_{2-x}Ce_xCuO_{4-\delta}$ (NCCO) [33]. Cuprates similar to LSCO are $La_{2-x}M_xCuO_4$, where M=Sr, Ba or Ca, and similar to NCCO are $M_{2-x}Ce_xCuO_{4-\delta}$, where M=La, Nd, Pr or Sm. The charge carriers in LSCO are holes and in NCCO are electrons. Even though they belong to the same 214-type cuprates because of their stoichiometry of the elements, they exhibit different crystal structures. LSCO has T-phase structure with CuO_6 octahedra and apical oxygen atoms, while NCCO has T'-phase structure with CuO_4 squares and without apical oxygen atoms. The lattice parameters of NCCO and LSCO are a=3.95 Å, c=12.07 Å and a=3.78 Å, c=13.2 Å, respectively [33, 34]. One can see that CuO_4 squares in T'-phase structure is considerably expanded and the c axis is shrunk, compared with those in T-phase structure.

1.2.2 Phase diagram

High-T_c superconductivity in cuprates results from charge doping into the parent Mott insulators. Similar to semiconductors, based on the types of their charge carriers, the cuprate oxides can be divided into two classes. The first one is the hole-doped cuprates, in which the

charge carriers are holes (electron vacancies, p-type carriers). Most of cuprates are hole-doped, such as $La_{2-x}M_xCuO_4$ (M=Sr, Ba or Ca) [35, 36] and YBCO [28]. In LSCO, since the valence state of divalent Sr^{2+} is lower than that of trivalent La^{3+}, Sr^{2+} substitution for La^{3+} in parent Mott insulator La_2CuO_4 can introduce holes and induce p-type superconductivity in LSCO with T_c≈38 K at x=0.15 [35, 36]. In $YBa_2Cu_3O_{6+x}$ reducing O^{2-} cause reduction of hole density, and for x=0, $YBa_2Cu_3O_6$ is at undoped state. The second one is electron-doped cuprate, in which the charge carriers are electrons (n-type carriers). The typical n-type cuprates are $M_{2-x}Ce_xCuO_{4-\delta}$ (M=La, Nd, Pr or Sm) [33, 34, 37] and infinite-layer compounds such as $S_{1-x}M_xCuO_2$ (M=Nd and La) [38, 39]. In NCCO, and tetravalent Ce^{4+} substitution for trivalent Nd^{3+} in parent insulator Nd_2CuO_4 can introduce electrons and induces n-type superconductivity in NCCO with T_c≈24 K at x=0.15 [33, 34].

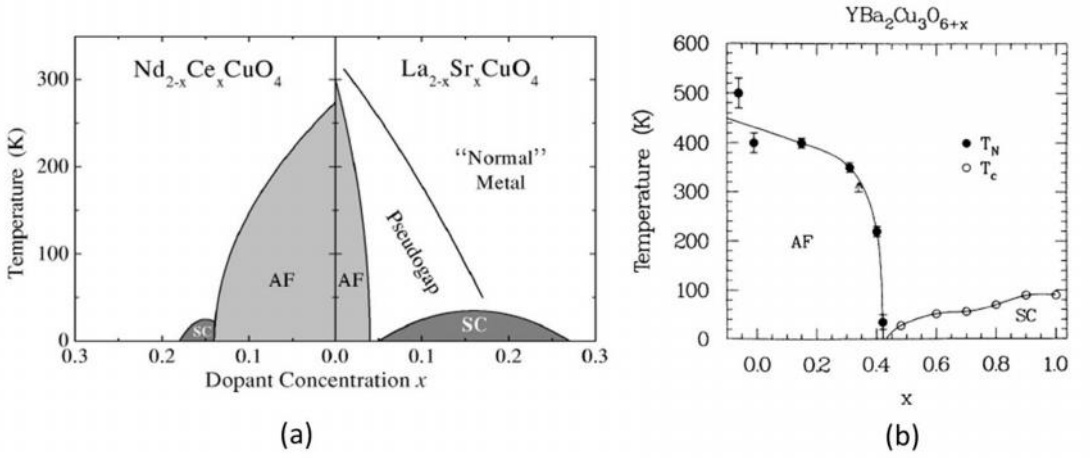

Figure 1.3 (a) Phase diagram for the electron-doped $Nd_{2-x}Ce_xCuO_4$ and the hole-doped $La_{2-x}Sr_xCuO_4$ [40]. (b) Phase diagram for the hole-doped $YBa_2Cu_3O_{6+x}$ [32].

Figure 1.3 shows the phase diagrams for NCCO, LSCO and YBCO, they share general evolution [32, 40]. The undoped cuprates are antiferromagnetic (AF) Mott insulators. With increasing doping, the Neel temperatures (T_N) decrease down to zero and the AF phases vanish, and then superconducting domes appear. Within the dome, T_c increases first and decreases as the doping is increased, with highest T_c at x≈0.15 electron/hole per planar Cu.

Finally, superconductivity disappears and normal metallic behaviour emerges at higher doping.

According to BCS theory, an energy gap emerges at superconducting state and disappears at temperature above T_c. However, in cuprate superconductors, the energy gap is still observed above T_c, which is considered as pseudogap (Figure 1.3(a) and Figure 1.4). The origin of pseudogap is still not clear [41-44]. In some of the theories, pseudogap is considered to be closely related to the superconducting gap. Local Cooper pairs are pre-formed at the temperature T^* below which pseudogap occurs. However, at this temperature range, superconductivity is not observed since there is no global phase coherence due to large phase fluctuations. Reducing temperature below T_c where global phase coherence is established, superconducting state is observed and the pseudogap evolves into superconducting gap. Therefore, pseudogap is considered as a precursor of superconductivity. Another theory proposes that pseudogap competes with superconductivity. In this case, the pseudogap persists down to the temperature lower than T_c. T^* line (dotted line in Figure 1.4) passes through the T_c line and drops to zero at a point the pseudogap state vanishes. This point is considered as a quantum critical point. Pseudogap has been observed in hole-doped cuprates through various measurements [41-43]. However, whether it exists in electron-doped cuprates is still under debate [45-49].

1.2.3 Electron-hole asymmetry

While the cuprates show common features in both hole- and electron-doped compounds, such as relatively high T_c, general evolution in phase diagram and presence of CuO_2 layers in their crystal structures, they also show dissimilarities in phase diagram, magnetic, superconducting, normal-state transport and electronic state properties. For the phase diagram of 214-compounds, AF order vanishes for a slight hole doping and the phase diagram shows a wide superconducting range at hole-doped side. At electron-doped side, however, AF order persists up to a high electron doping level, almost up to the optimal doping level and the phase

diagram shows a narrow superconducting range [49]. Compared to hole-doped cuprates, electron-doped ones show much lower upper critical magnetic field H_{c2} [50, 51]. For normal-state transport, the properties depend on the type of carriers, for example, in-plane normal-state resistivity exhibits quadratic temperature dependence for n-type cuprates [52] while linear temperature dependence is seen for p-type cuprates at optimal doping [53, 54]. In p-type LSCO at low doping level, electronic states appear near ($\pi/2$, $\pi/2$) in momentum space, however, in n-type NCCO at low doping level, electronic states appear near (π, 0) [55, 56]. Moreover, chemical potential shift monotonously increases with increasing electron doping for NCCO, however, chemical potential shift is suppressed in the underdoped region for LSCO [57]. Such investigation of electron- and hole-doping asymmetry (symmetry) in cuprates should help in understanding the origin of the cuprate superconductors [58, 59].

1.2.4 Quantum phase transition

Quantum phase transition (QPT) is the phase transition between the ground states of a physical system governed by quantum fluctuations. It could be tuned by external control parameters. In cuprate superconductors, the control parameter could be the doping. Figure 1.4 shows the possible quantum critical points (QCPs), across which QPT between two phases occurs [44]. Starting from the undoped compound, as the doping increases, one can find the first QCP where AF state vanishes and the second QCP where superconductivity develops. It has been suggested that these two QCPs can be combined into one or AF state vanishes at doping level higher than that where superconductivity develop [60]. The latter case may occur in electron-doped cuprates since the AF order can persist up to almost optimal doping level (Figure 1.4). The third QCP sits just beyond the optimum doping point within the superconducting dome and it is related to the competition between pseudogap state and superconducting state. This QCP has been suggested by the electrical transport measurement. The QPTs occurred in both of electron-doped $Pr_{2-x}Ce_xCuO_4$ and hole-doped $La_{2-x}Sr_xCuO_4$ and $Bi_2Sr_{2-x}La_xCuO_{6+\delta}$ [61-63], which is evidenced by the observation of a Hall coefficient anomaly [61, 63] and a thermopower anomaly [62]. These anomalies appear near optimum

doping level and coincident with the collapse of the pseudogap states. The last point is the one where superconductivity disappears and Fermi-liquid metal develops, which may be related to the changes of Fermi surface topology [44].

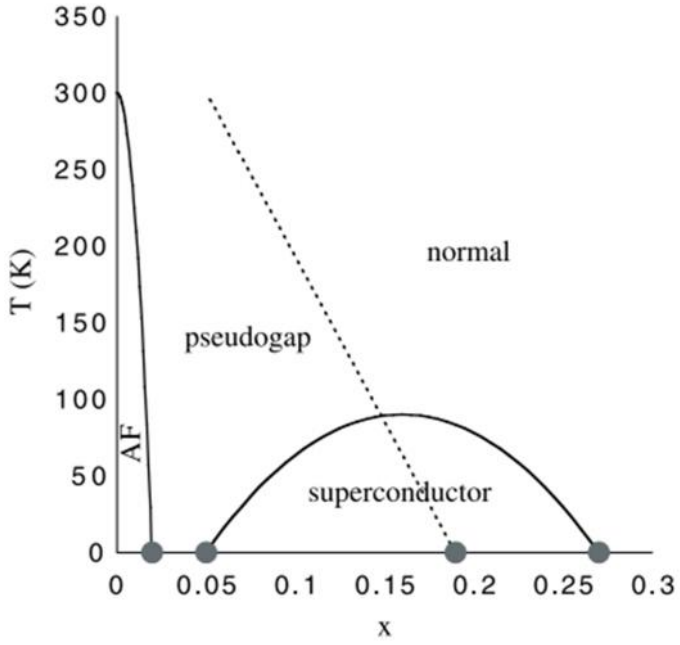

Figure 1.4 Phase diagram and possible quantum critical points (●) in cuprates [44]. Dotted line is the temperature *T** below which pseudogap appears.

Near the QCP where superconductivity develops, superconductor-insulator transition (SIT) occurs if the doping level is varied. It is proposed that SIT at the limit of zero temperature and two dimensions is an example of a QPT [64-66]. The QPT could be suggested by finite-size scaling analysis based on finite temperature data, which requires the quasi-continuous tuning of the control parameter (carrier density in Figure 1.4) to precisely determine the critical point [23, 24, 67-69]. For the carrier density-tuned SIT, it is difficult to realize from chemical doping since there is experimental uncertainty of element composition when synthesize a compound. Moreover, in order to get different carrier densities, one needs to synthesize a serial of samples. The sample quality may vary with different samples and thereby the measurement data could not reveal its evolution with carrier densities. However, for the electric field-effect doping, one can work with a single sample and tune carrier densities as finely as desired only by controlling the gate voltage. Therefore, field-effect doping could be

an advisable method for the study of SIT. In cuprates, electric field-tuned SITs have been realized in hole-doped LSCO and YBCO, and they have been considered as two-dimensional QPTs via finite size scaling analysis [23, 24, 26]. Electric field-tuned SITs have also been observed in other materials such as amorphous Bi film [68], $LaAlO_3/SrTiO_3$ interface [9]. Besides the carrier density, SITs can be induced by other external control parameters such as disorder (film thickness) and magnetic field. For example, disorder-tuned SITs have been observed in amorphous Bi, Pb and Al films [70-72], Mo-C films [73], FeSe thin films [74], and magnetic field-tuned SITs in NCCO film [75], YBCO single crystal [76], LSCO films [77], InO_x films [78-81], Pb films [82], FeSe thin films [74], amorphous MoGe films [67, 83].

1.3 Perovskite oxide interface

1.3.1 ABO_3 perovskite oxides

Perovskite oxide is a class of complex oxides which can be described by the general formula of ABO_3. In this formula, 'A' is an alkaline earth metal (Be, Mg, Ca, Sr, Ba, Ra) or rare earth metal (Sc, Y, La, Gd, Dy) element, 'B' is a transition metal (Sc, Ti, V, Mn, Fe) or a poor metal (Al, Ga, Pb, Sn, Tl, In) element, and 'O' is the oxygen element. The perovskite oxides have a cubic or pseudo-cubic structure, with a stack of alternating layers of AO and BO_2 along the [001] direction. The typical materials are $SrTiO_3$, $LaAlO_3$, $LaTiO_3$, $DyScO_3$, $NdGaO_3$, and so on. The cuprate superconductors as have been shown above are also members of the perovskite families. Figure 1.5 shows a schematic cubic structure of ABO_3 oxides. In terms of symmetry, this structure has the 'B' cation in a 6-fold coordination, surrounded by 'O' anion in the form of octahedral and the 'A' cation in a 12-fold coordination. In this structure, cation 'A' is generally larger in size than cation 'B', and anion 'O' bonds to both 'A' and 'B' cations.

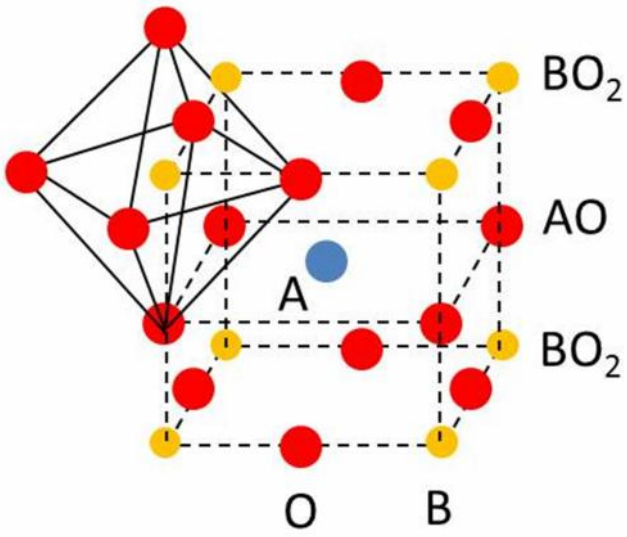

Figure 1.5 Sketch of cubic ABO_3 perovskite structure.

Along the [001] direction, the structure of ABO_3 perovskite can be considered as a stack of alternating sublayers of AO and BO_2. Depending on the valence of the cations and the total charge states in the sublayers, the perovskite can be classified into polar and non-polar materials. For example, since both of the valence states of La ion and Al ion are 3+, $LaAlO_3$ is a polar material with a stack of positively charged $(LaO)^{1+}$ and negatively charged $(AlO_2)^{1-}$ sublayers. Since the valence states of Sr and Ti ions are 3+ and 4+, respectively, $SrTiO_3$ is a non-polar material with a stack of neutral $(SrO)^0$ and $(TiO_2)^0$ sublayers. Combination of polar and non-polar perovskite oxides can lead to intriguing properties at the interface which are not observed in the bulk constituents.

Owing to various selections of A- and B-cations, the sensitivity of structure transitions, and the subtle interactions between charge, orbital, and spin degree of freedom, perovskite materials can exhibit a wide class of physical properties. For example, for various A-site cations, $SrTiO_3$ is a quantum paraelectric and insulating material, while $BaTiO_3$ is a ferroelectric material. For various B-site cations, $SrRuO_3$ is a ferromagnetic material, while $SrMnO_3$ is an antiferromagnetic material. Moreover, $SrTiO_3$ is a band insulator with a band

gap of around 3.2 eV while $LaTiO_3$ is a Mott insulator with Mott-Hubbard gap of around 0.2 eV. Through charge doping, insulating $SrTiO_3$ and $LaTiO_3$ can be tuned to be metallic behavior in $La_{1-x}Sr_xTiO_3$. Antiferromagnetic $SrMnO_3$ and $LaMnO_3$ can be tuned to be magnetic in $La_{1-x}Sr_xMnO_3$. Moreover, in cuprate parent insulators which have a perovskite-like structure, charge doping can cause high-T_c superconductivity. These examples may provide avenues to search for new and muli-properties in perovskite oxides by modifying the interplay between charge, spin and orbital degree of freedom of metal cations.

$SrTiO_3$ and $LaAlO_3$ are the perovskite oxides which have been studied intensively since their interfaces have been demonstrated to show many intriguing properties. $SrTiO_3$ has a cubic structure with a lattice constant of 3.905 Å at room temperature. With decreasing temperature, several structure transitions occur such as a cubic to tetragonal phase transition at ~105 K, a tetragonal to orthorhombic phase transition at ~60 K and another orthorhombic to rhombohedral phase transition at ~30 K [84-86]. $SrTiO_3$ has a dielectric constant value of ~300 at room temperature, increasing to a few thousands at low temperature [87]. Thus, it is an ideal material as a gate dielectric in oxide-based electric field-effect devices. $SrTiO_3$ is a band insulator with a band gap of 3.2 eV. However, oxygen vacancies and doping can cause conductivity in $SrTiO_3$, and even superconductivity [88-91]. Oxygen vacancies can be induced by thermal annealing in vacuum, ion milling and bombardment of high-energy plasma produced by pulsed laser irradiation. Charge doping can be induced by La substitution for Sr, and Nd substitution for Ti. In contrast, for another band insulator $LaAlO_3$ which has a band gap of 5.6 eV, it is difficult to create oxygen vacancies. $LaAlO_3$ has a rhombahedral structure at room temperature and transforms into a cubic structure at temperature above 875 K [92, 93]. For simplicity, $LaAlO_3$ can be regarded as cubic (pseudocubic) at room temperature and has a lattice parameter of 3.79 Å. Both $SrTiO_3$ and $LaAlO_3$ serve as important substrates for the growth of many oxide thin films, such as high-T_c cuprates and manganites.

1.3.2 The emergence of the $LaAlO_3/SrTiO_3$ interface

Due to their band gaps or Mott-Hubbard gaps, most of perovskite oxides are insulating in bulk materials without chemical doping, being either band insulators or Mott insulators. However, when some of these oxides are brought together, conductivity would emerge at their interface. A typical example is the conductivity at the interface between $LaAlO_3$ (LAO) and $SrTiO_3$ (STO), which was first found by Ohtomo *et al*. in 2004 [94]. In their experiment, a two-dimensional electron gas (2DEG) formed as LAO was atomic-scale layer by layer deposited on TiO_2 terminated STO. This stimulated a substantial body of work to search for its origin and other novel properties. It has been shown that the interface exhibited other various electronic and magnetic phases such as a tunable metal-insulator ground state [95], 2D superconductivity [96], magnetic ground state [97], and an electronic phase separation [98], 2D quantum oscillations [99-101], spin-orbit interaction [102-104], coexistence of mutually exclusive superconductivity and magnetism [105-107] and high-T_c cuprate-like superconducting gap [108]. These phenomena provide new insights for understanding the nature of electronic and magnetic properties in strongly correlated oxide compound.

1.3.3 Origin of the conductivity in $LaAlO_3/SrTiO_3$ interfaces

There are at least three models to explain the possible mechanism of conducting LAO/STO interface. The first model, which is a commonly believed one, is interface electronic reconstruction [94, 109, 110]. LAO is a polar material stacked by positively charged $(LaO)^+$ and negatively charged $(AlO_2)^-$, while STO is a non-polar material stacked by the neutral $(SrO)^0$ and $(TiO_2)^0$. When LAO is layer-by-layer grown on STO, there will be a potential across the LAO and it diverges with increasing LAO thickness. In order to avoid such polarization catastrophe, an electronic reconstruction is needed, in which 0.5 electrons per LAO uc are transferred from LAO into the interface. This mechanism was strongly supported by the observation that a critical thickness of LAO grown on (100)-oriented STO is needed to obtained conducting interface [95]. When the thickness of LAO is larger than 3 uc and the

built in potential (0.9 eV/uc) exceeds the STO bandgap of 3.2 eV, a 2DEG occurs at the interface. Such polarization discontinuity has also recently been observed at the interface when LAO was grown on (110)-oriented STO [111].

The second model is the intermixing of Ti/Al or La/Sr at the interface [112, 113]. This could be possible since the intermixing causes the chemical doping in LAO or STO, for example, La-doped STO, and thereby causes conductivity. However, intermixing could not explain that the interface is still insulating when LAO is grown on SrO terminated STO [94, 109]. Moreover, interfaces between STO/LAO, formed from STO film grown on LAO substrate in which intermixing is expected, show insulating behavior [114]. From TEM studies [109], it has been found that LAO/STO interfaces are very sharp, showing little intermixing. These observations suggest that intermixing should be excluded as a reason for conduction at a high-quality interface.

The third possible mechanism is creation of oxygen vacancies in STO substrates during the deposition process [115-118]. The oxygen vacancies can be further demonstrated in the conducting interfaces when amorphous LAO, and even amorphous STO, yttria-stabilized zirconia (YSZ), $YAlO_3$ and Al_2O_3 were deposited on STO substrates [119, 120]. The creation of oxygen vacancies can be induced by the bombardment of high-energy plasma on STO substrates and/or chemical reaction in which oxygen in STO is extracted by overlayers.

Note that these three models should not work independently. One cannot conclude completely a single mechanism, and there is the possibility that multiple mechanisms operate together in these interface. Moreover, each mechanism may dominate in each specific case. Comprehensive study by Liu *et al.* in our laboratory demonstrates that the conductivity is dominated by oxygen vacancies when the LAO overlayer is amorphous, and by both oxygen vacancies and polarization catastrophe in unannealed crystalline LAO/STO heterostructures, and only by polarization catastrophe in oxygen-annealed crystalline LAO/STO heterostructures [121]. For this reason, a critical thickness of 4 uc is needed to induce

conductivity in oxygen-annealed crystalline LAO/STO, while in as-grown sample, the critical thickness can be less than 4 uc [122].

1.4 Motivation and outline

Chapter 2 give an introduction on experimental thin film preparation and characterization techniques.

Even though high-T_c cuprate superconductors show some symmetric features in both hole- and electron-doped compounds, they also exhibit asymmetric properties. Investigation of n-p asymmetry (symmetry) in cuprates is important to reveal the mechanisms of high-T_c superconductivity [58, 59]. However, the typical n-p asymmetry (symmetry) investigations are based on the cuprates with different crystallographic structure such as NCCO (T' structure) and LSCO (T structure). Moreover, these materials have different parent Mott insulators (Nd_2CuO_4 for NCCO and La_2CuO_4 for LSCO), and thus, exhibit different properties even without doping [123]. Therefore, it is desirable to synthesize an ambipolar cuprate in which electrons and holes can be doped into a single Mott insulator without changing the crystallographic structure and address the inherent n-p asymmetry (symmetry). Using pulsed laser deposition (PLD) system, we try to synthesize ambipolar La-doped YBCO thin films. P-type thin films with high carrier density shows superconductivity and n-type thin films show metallic behaviour. The n-type film at optimally reduced condition shows a carrier density as high as ~2.87×10^{21} cm^{-3}, which is at the near edge of superconducting dome. Moreover, inherent n-p asymmetric (symmetric) investigation is conducted up to a higher doping level. This part is discussed in Chapter 3.

Superconductor-insulator transitions have been observed in various materials and induced by various control parameters such as disorder, magnetic field and carrier concentration. In cuprate superconductors, since the superconductivity is induced by doping charge carriers into parent insulator, carrier density-tuned SIT is of particular interest. Using the method of ionic liquid-assisted electric field effect doping, carrier density-tuned SITs have been

observed in hole-doped cuprate LSCO and YBCO [23, 24, 26]. However, carrier-tuned SIT in electron-doped cuprate has not been observed. Understanding the nature of carrier-tuned SIT in electron-doped cuprate is crucial to understand the origin of high T_c superconductivity and also n-p asymmetry. We synthesized ultrathin electron-doped $Pr_{2-x}Ce_xCuO_4$ films and fabricated EDLT devices. By applying electric field, the electron density could be tuned quasi-continuously and SIT could be induced. Moreover, owing to the low upper critical field in $Pr_{2-x}Ce_xCuO_4$ system, we performed magnetic field-induced SITs in the superconducting EDLTs. This part is shown in Chapter 4.

The LAO/STO interface exhibits various novel properties such as conductivity, superconductivity and magnetism, which are not observed in its bulk constituents. Modulation of its conductivity could help in understanding of the origin of such properties and explore its potential applications. We demonstrate the modulation of electrical transport properties in LAO/STO interface by electric field effect using EDLT configuration. Metallic-insulating phase transition can be induced in initially metallic samples, and this effect can be used for reversible resistive switching devices. Field-effect transistor operation is also demonstrated in this two-dimensional gas. These results suggest the potential application of perovskite oxide interface. Moreover, the electron mobility can be enhanced by reducing the carrier density. Due to the enhancement of mobility, we can observe quantum oscillations of the conductance at the liquid-gated LAO/STO interface. This part is shown in Chapter 5.

Chapter 6 shows the summary and future directions of this thesis.

Chapter 2 Sample Preparation and Characterization Techniques

2.1 Film deposition using pulsed laser deposition system

We use pulsed laser deposition (PLD) system to grow oxide thin films and heterostructures in our lab. PLD has turned out to be a good technique to synthesize oxide thin films with the same stoichiometry as the targets, high crystalline quality and relatively flat surface. Figure 2.1 shows the schematic diagram of a PLD setup with in-situ reflection high energy electron diffraction (RHEED). Before deposition of thin films, the chamber is pumped down to a base pressure of 10^{-9} Torr by using a turbo molecular pump. Depending on the material of interest, the pressure in the chamber can be controlled under various ambiences (e.g. O_2, O_3, N_2, Ar etc.). The substrate is attached onto the heater whose temperature can be controlled from room temperature to ~800 ^{o}C. During deposition, a pulsed laser beam is focused onto a target and generates a high-energy plasma plume. The material flux provided by the plume will accumulate at the surface of the substrate and then form the desired thin films. The distance between the substrate and target is >5 cm and can be controlled by moving the heater up and down. The laser used in this work is a Lambda Physik Excimer KrF UV laser with wavelength of 248 nm. The area of the laser spot is ~2x3 mm^2 and the laser energy intensity on the target is 1-2 J/cm^2.

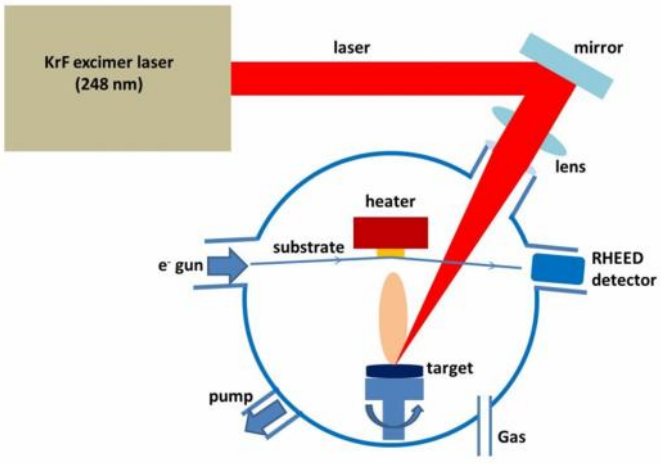

Figure 2.1 Schematic diagram of a pulsed laser deposition setup.

RHEED is used to *in-situ* monitor the thin film growth. A RHEED system generally consists of an electron gun and detector with a phosphor florescent screen. During the characterization, an electron beam is emitted from RHEED gun, incident onto the substrate surface with a low grazing angle, and then reflected and diffracted into the detector. The reflection and diffraction beams are then collected by a florescent screen. Since the incident angle is very low, only the top few atomic layers contribute to the diffraction pattern. This enables the measurement of the surface properties. Inset of Figure 2.2 shows a typical RHEED pattern for STO (100). The main spot (specular spot) inside the rectangle is from the reflection electron beam and collection of its intensity provides information of the film growth. The intensity of the specular spot is roughly proportional to the surface flatness. High intensity suggests smooth surfaces while low intensity suggests rough surface. During the deposition, the intensity of the selected area of specular spot is integrated and shown as a function of time (Figure 2.2). In the layer-by-layer growth mode, at the start of deposition, the intensity decreases down to the lowest value at which half of monolayer is completed. This is because the surface roughness increases and reaches its maximum when the substrate is half covered by the deposited materials, corresponding to the appearance of a large number of pits on the surface. After that the intensity gradually increases until the finish of one monolayer growth, since the adatoms diffuse into those pits to complete the growth of the latter half layer. Such process is repeated as the thin film growth continues and the corresponding intensity oscillations are obtained. Figure 2.2 shows the RHEED intensity oscillations for 15-monolayer LAO grown on STO (100). Clear oscillations of reflection intensity indicate a prefect layer-by-layer growth. One oscillation represents the growth of one monolayer LAO.

For the growth of La-doped $YBa_2Cu_3O_y$ and $Pr_{2-x}Ce_xCuO_4$ as will be shown in Chapter 3 and 4, RHEED intensity oscillations are not observed, probably due to the high deposition oxygen pressure which is required to obtain the CuO_2 plane in cuprates. For this reason, we used scanning electron microscope (SEM), X-ray reflectivity (XRR) and Profiler to characterize the film thickness. Table 2.1 shows the parameters used for the growth of various materials in

this thesis, including deposition temperature (T_{dep}), deposition oxygen pressure (P_{dep}), energy intensity on the target (E_{spot}), laser frequency (f) and the thickness characterization. The detailed growth process will be shown in following chapter separately.

The thin films in the PLD process can be grown from single crystalline or polycrystalline targets. In the thesis, for the growth of $LaAlO_3$ and $SrTiO_3$, we use commercially obtained single crystalline targets. For the growth of high-T_c cuprate superconductors, we use polycrystalline targets which can be prepared using pure cation oxide powders. For example, the $YBa_2Cu_3O_y$ target can be made by mixing, sintering and then disk-like shaping of Y_2O_3, La_2O_3, $BaCO_3$ and CuO. The detailed preparation of target will be separately demonstrated in the following chapters.

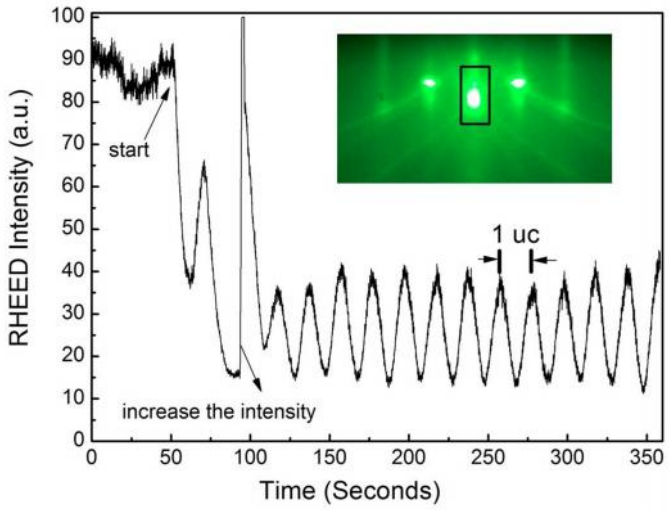

Figure 2.2 RHEED intensity oscillations for 15 uc LAO grown on STO (100). Inset is the RHEED pattern for STO (100) before deposition.

Table 2. 1 Parameters used for thin film growth using pulsed laser deposition.

Material	T_{dep} (^oC)	P_{dep} (Torr)	E_{spot} (J/cm^2)	f (Hz)	Thickness characterization
La-doped $YBa_2Cu_3O_y$	760	2×10^{-1}	1.7	4	SEM, XRR, Profiler
$Pr_{2-x}Ce_xCuO_4$	790	2×10^{-1}	1.7	2	SEM, XRR, Profiler
$LaAlO_3$	740	2×10^{-3}	1.7	2	RHEED

2.2 Sample characterization techniques

2.2.1 X-ray diffraction

X-ray diffraction (XRD) is one of the most powerful techniques to characterize the material structure. Figure 2.3(a) schematically shows the geometry of XRD, illustrating the geometrical relationship between the XRD and the crystal plane separation distance. The incident X-ray beams having the same wave phase are diffracted on each crystal plane. The length difference between the beams is the total length of line BC and line CD. When the length of line BC and CD is equal to a multiple times of the wavelength of the incident X-ray, the diffracted beam intensity is strong enough to be detected and the intensity will show a peak at certain incident angle position. Otherwise, the resultant diffracted wave phases will offset each other and there will be no intensity peak. In general, the position of the constructive diffraction is described by the Bragg equation:

$$2d\sin\theta = n\lambda, \qquad \text{Equation (2-1)}$$

where d is the spacing between the crystal planes, θ is the X-ray incident angle, λ is the wavelength of the X-ray, n is an arbitrary integer defined by the order of diffraction. The main parameters of XRD measurements are the intensity peak (Bragg peak) position and full width at half maximum (FWHM), which are used to determine the lattice parameter and the crystallinity of the films, respectively.

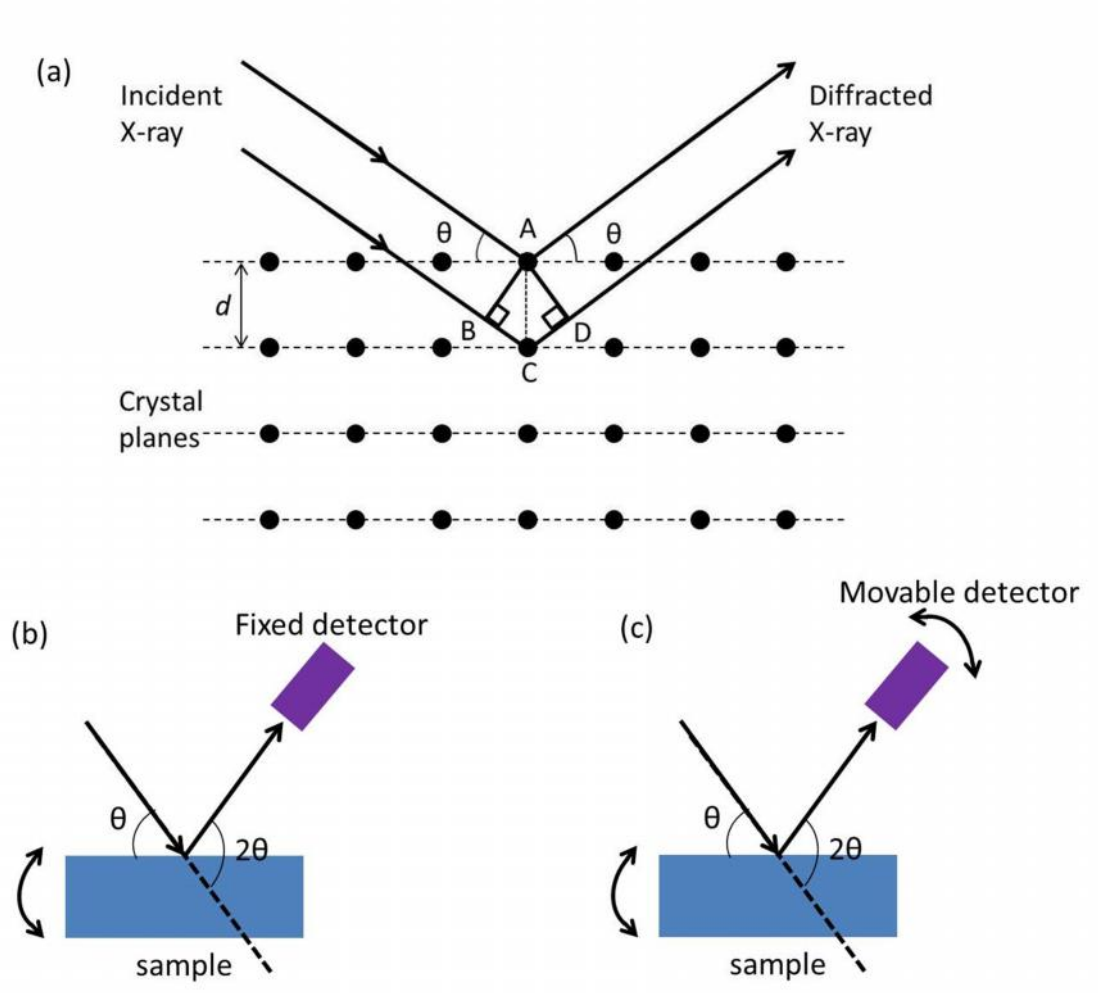

Figure 2.3 (a) Schematic geometry of X-ray diffraction. (b) ω-scan (c) θ-2θ scan

There are two conventional XRD scan modes, ω-scan (Figure 2.3(b)) and θ-2θ scan (Figure 2.3(c)). For the ω-scan (rocking curve), the X-ray source and detector are fixed at certain angles, but the sample is rotated slightly around the Bragg peak. During this measurement, the diffraction intensity as a function of angle ω is collected. It should be noted that ω is the angle θ shown in the figure. Since only the sample is rocked, which means that only the incident angle varies, the intensity in ω-scan is sensitive to angular variation. Therefore, the FWHM of ω-scan reveals the flatness of crystal planes and can be used to determine the crystalline quality. Figure 2.4(a) shows an example of rocking curve on (005) peak of $YBa_2Cu_3O_y$ (YBCO). In this measurement, the detector is fixed at 2θ=38.56^o while the sample is rotated over ±2^o at the incident angle of θ=19.28^o. The FWHM is 0.36^o. For the θ-2θ scan, the source

is fixed, but both the sample and the detector are rotated. If the sample rotates over an angle of θ, then the detector will rotate over 2θ at the same time. During the measurements, the diffraction intensity as a function of 2θ is collected. The intensity peak position is used to calculate the *c*-axis lattice parameters and chemical composition of thin films, and also to characterize the strain states. In contrast to ω scan, the FWHM of θ-2θ scan reveals the interplanar distance variation. Figure 2.4(b) shows an example of θ-2θ scan of YBCO film grown on $SrTiO_3$ (001) substrate. The (00*l*) peaks of the thin films are clearly observed, where *l* is integer. The (00*l*) peak positions are corresponding to the ones calculated by the Bragg equation, assuming that the *c*-axis lattice constant of YBCO is 11.68 Å and wavelength of X-ray is 1.5406 Å.

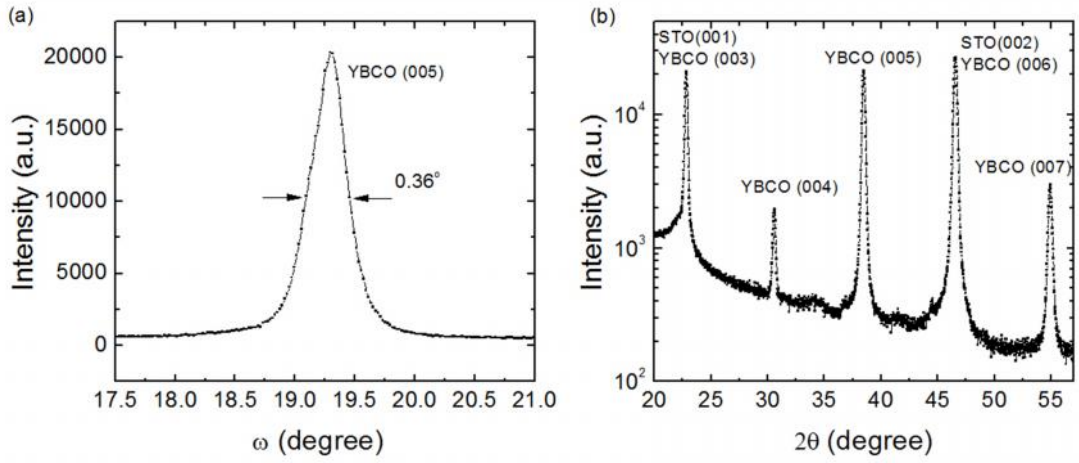

Figure 2.4 X-ray diffraction patterns of $YBa_2Cu_3O_y$ for (a) ω-scan (b) θ-2θ scan.

In this thesis, the XRD measurements were done using Bruker D8 Discover in NUSNNI-NanoCore and PANalytical X'pert in Physics Department. In some cases, the measurements were done using X-ray Demonstration and Development (XDD) beamline at Singapore Synchrotron Light Source (SSLS), which will be described in the following chapters.

2.2.2 Atomic force microscopy

Atomic force microscopy (AFM) is used to characterize the sample surface. Figure 2.5 shows the schematic diagram of an AFM setup. Generally, an AFM consists of a tip, laser and

photodiode detector. During the measurement, the tip is scanned on the sample surface, a laser beam a shone on the backside of the cantilever and is reflected into the photo detector. The tip displacement resulting from tip-sample surface interaction force is amplified by the laser and the morphology of the sample surface is obtained by analysing the relative light intensity.

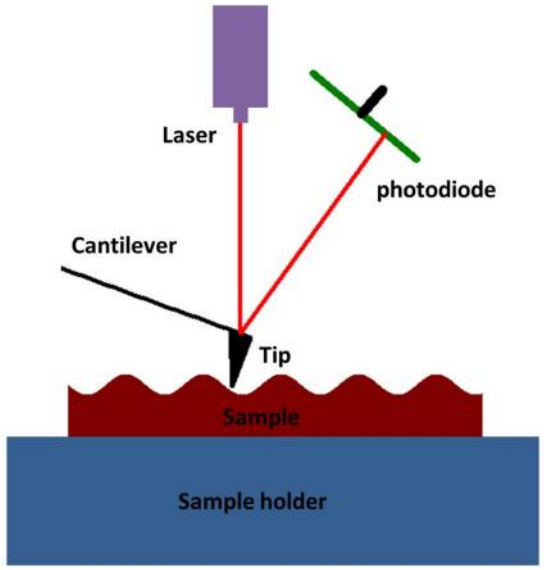

Figure 2.5 Schematic diagram of an atomic force microscopy

The primary operation modes for mapping the sample morphology are contact and tapping modes. In contact mode, the tip is directly in contact with the sample surface and the cantilever is deflected by the van der Waals forces between the tip and sample surface. The morphology is mapped by variation of reflected laser intensity caused by cantilever deflection. In tapping mode, the cantilever is driven to oscillate at a constant frequency close to its resonance frequency. The oscillation amplitude and phase are affected by the sample morphology, which causes the deflection of cantilever, enabling the mapping of the surface.

In this thesis, we use Agilent 5500 AFM and tapping mode to characterize our samples. We present an example in Figure 2.6, showing the surface image of $La_{1.85}Sr_{0.15}CuO_4$ on $SrTiO_3$ (100) substrate grown at temperature of 720 ^{o}C and oxygen pressure of 20 mTorr. Stacks of

assembled short nanorods can be clearly seen. Note that $La_{1.85}Sr_{0.15}CuO_4$ is normally grown at high oxygen pressure of 200 mTorr to enable the construction of CuO_2 plane, and thus, occurrence of superconductivity. Under this condition, the surface is flat and without nanorods. From the transport measurement, this sample is highly insulating. The transport property and the observation of nanorods suggest the lack of CuO_2 planes in this sample.

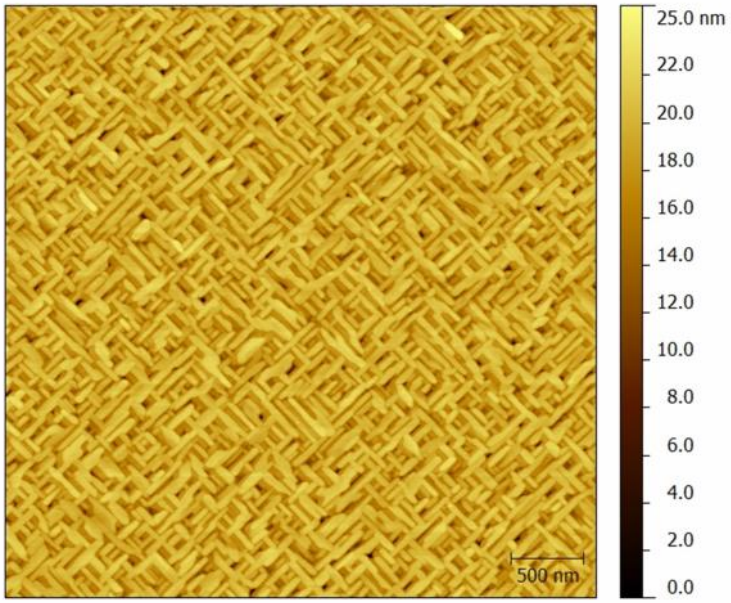

Figure 2.6 AFM image of $La_{1.85}Sr_{0.15}CuO_4$ on $SrTiO_3$ (100) substrate grown at temperature of 720 ^oC and oxygen pressure of 20 mTorr.

2.2.3 Electrical transport measurement

Electrical transport is the main measurement technique used in this thesis. We use a Quantum Design Physical Property Measurement System (PPMS) to characterize electrical transport properties. The temperature can be varied from 2 to 400 K and the magnetic field from 0 to 9 T. Generally, there are three types of measurements in transport studies: temperature dependent resistivity (*R*-*T* curve), magnetoresistance (MR) and Hall effect.

2.2.3.1 Resistivity measurement

The resistivity measurement can be performed using four-probe method in order to remove contact resistance, and can be in van der Pauw or linear geometries. Figure 2.7(a) shows a typical van der Pauw measurement geometry. A current is applied along one edge of the sample (I_{12}) and the voltage across the opposite edge (V_{34}) is measured, which gives a resistance of $R_{12,34}=V_{34}/I_{12}$. Similarly, another resistance $R_{13,24}=V_{24}/I_{13}$ can also be obtained, in which the current I_{13} is perpendicular to I_{12}. The intrinsic sheet resistance (R_s) of the sample can be calculated from the van der Pauw equation:

$$e^{-\pi R_{12,34}/R_s} + e^{-\pi R_{13,24}/R_s} = 1 \qquad \text{Equation (2-2)}$$

Assuming that $R_{13,24}= R_{12,34}=R$, the sheet resistance can be simplified as

$$R_s = \frac{\pi R}{\ln 2} \qquad \text{Equation (2-3)}$$

For a sample with a thickness of d, the resistivity ρ can be obtained by

$$\rho = R_s \times d = \frac{d\pi R}{\ln 2} \qquad \text{Equation (2-4)}$$

It should be noted that in some cases, $R_{13,24}$ is different from $R_{12,34}$, and thus, R_s can only be numerically calculated by van der Pauw equation. Van der Pauw method has been widely used to characterize the electrical transport properties of oxide heterostructures.

In the linear measurement geometry, a rectangular sample with a large ratio of length to width is required in order to ensure a uniform current across the sample. At some cases for accurate calculation of resistivity and sheet resistance, a micrometer-scale Hall bar is fabricated. Figure 2.7(b) shows the linear geometry of resistivity measurement. A current is applied along the long dimension and the voltage difference between two electrodes is measured. The resistivity can be calculated by

$$\circ = \frac{R \cdot d \cdot w}{l} \ , \qquad \text{Equation (2-5)}$$

where R is the measured resistance, d the thickness, w the width and l the distance between two voltage probes. The product $A=d \cdot w$ is the cross-section area.

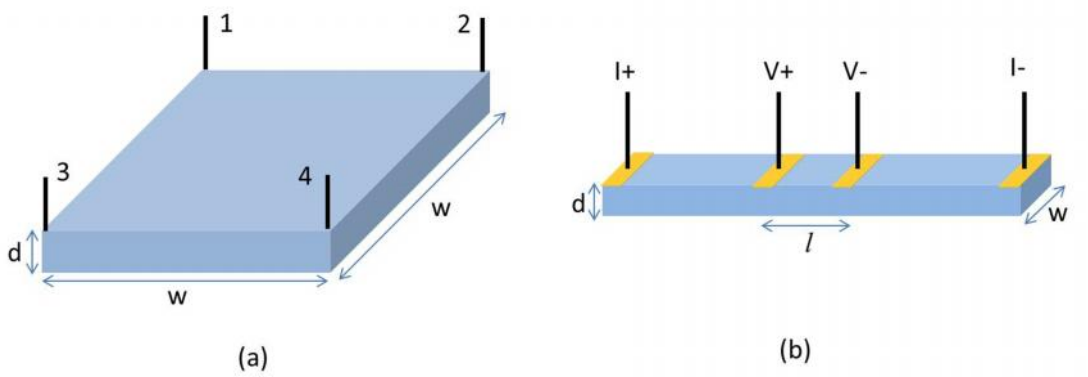

Figure 2.7 (a) Schematic diagram of the van der Pauw measurement geometry. (b) Linear geometry. Yellow rectangular on the sample in (b) indicates metal contact on the sample.

In the thesis, for the measurement of oxide interfaces, the electrode contact to the sample is done by direct Al ultrasonic wire bonding. For the thin films, the contact is done by direct Al wire bonding, or by deposition of Cr/Au (10/70 nm) layers and then wire bonding. Since electronic phase transitions may occur, and thereby the electrical transport properties will change as the sample is cooled down to low temperature, it is desirable to measure resistivity-temperature *(R-T)* curves. This can be done in the PPMS system. As an example, we show *R-T* curve of the typical high-T_c superconductor YBCO in Figure 2.8. This was measured in the linear geometry with Cr/Au electrode contacts. One can see that the resistivity sharply drop to zero at T_c=88 K, indicating the superconducting phase transition.

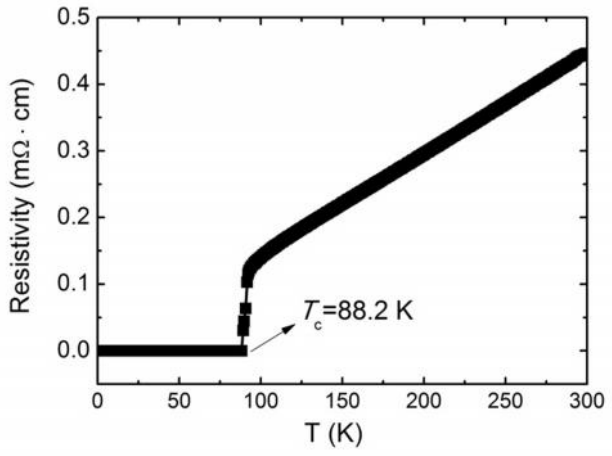

Figure 2.8 Resistivity as a function of temperature for a 250 nm $YBa_2Cu_3O_7$ thin film grown on $LaAlO_3$ (100) substrate. The film was grown at 760 ^oC and oxygen pressure of 200 mTorr, than then post-annealed at 550 ^oC in 1-atm oxygen for 30 min.

2.2.3.2 Hall effect measurement

Hall effect measurement is commonly used to determine the carrier density and types of charge carriers (electron or hole). Figure 2.9(a) shows schematic geometry of the Hall effect measurement. A current is passed across the sample under magnetic field perpendicular to the sample and current direction. Due to Lorentz force generated by magnetic field, the moving carriers deviate from their straight path and accumulate on lateral edges of the sample. The direction of the carriers depends on their polarity, i.e. negative or positive. As a result, the charge accumulation induces a potential difference across the sample and transverse to the current. This potential difference is called Hall voltage V_H, and for only one type of charge carrier in a sample, it is given by

$$V_H = -\frac{IB}{ned} \qquad \text{Equation (2-6)}$$

where I is the current, B the magnetic field, n the carrier density, e the elementary charge and d the thickness of the sample. From equation (2-6), we can define the Hall coefficient as

$$R_H = -\frac{1}{ne} = \frac{V_H d}{IB} = \frac{Rd}{B}\ , \qquad \text{Equation (2-7)}$$

where $R=V_H/I$ is the measured Hall resistance. Therefore, the carrier density can be determined by measuring *R*, *d* and *B*. Equation (2-7) can also be rewritten as

$$R = -\frac{B}{ned} \qquad \text{Equation (2-8)}$$

and therefore, it can be seen that Hall resistance is proportional to the applied magnetic field. Generally, Hall resistance as a function of magnetic field is measured and linearly fitted, and then the slope is obtained. This slope is used to determine the carrier density and types of carriers.

For a two-dimensional system, equation (2-8) can be expressed as

$$R_s = -\frac{B}{n_s e}\ , \qquad \text{Equation (2-9)}$$

where R_s is the sheet resistance and n_s he sheet carrier density.

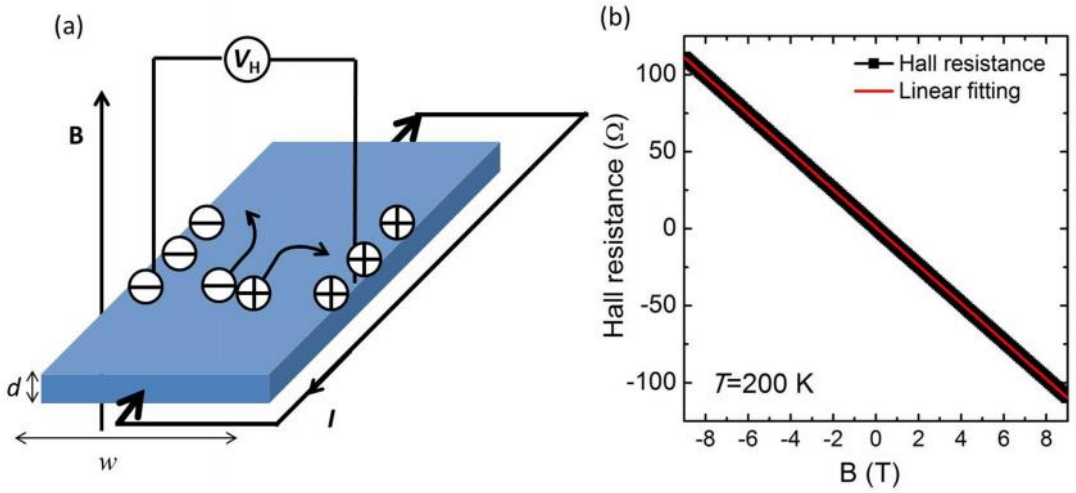

Figure 2.9 (a) Schematic diagram of Hall effect measurement. (b) Hall resistance as a function of magnetic field for a LAO/STO interface grown on $NdGaO_3$ (110) substrate.

In the measurement, we can use van der Pauw or Hall bar geometries. For the van der Pauw geometry (Figure 2.7(a)), the current is applied between 1 and 4, and the Hall resistance is

measured between 3 and 2. In Figure 2.9(b), we show the Hall effect of a LAO/STO interface grown on $NdGaO_3$ (110) substrates, measured by van der Pauw method [124]. One can see that Hall resistance is a perfect linear function of magnetic field. A charge carrier of an electron type and a sheet carrier density of 5×10^{13} cm^{-2} can be determined by linear fitting of the data. For the Hall bar geometry, devices with patterns are required, which will be presented in Chapter 4 and Chapter 5.

From the sample resistance and carrier density, the carrier mobility can be obtained. For a two-dimensional system, the carrier mobility μ_H is

$$\mu_H = \frac{1}{n_s e R_s} , \qquad \text{Equation (2-10)}$$

where μ_H is also called Hall mobility. Mobility characterizes the ability of carrier movement through a sample. Semiconductors with high mobility could be used to fabricate high-performance devices such as transistors. High mobility allows the search of quantum phenomena such as quantum Hall effects in two-dimensional materials.

2.2.3.3 Magnetoresistance measurement

Magnetoresistance (MR) measurement is the study of resistance under magnetic field. For a thin film and two-dimensional system, MRs include the in-plane and out-of-plane MR with magnetic field parallel and perpendicular to the surface, respectively. Mathematically MR is defined as

$$MR = \frac{R(B) - R(0)}{R(0)} \times 100\% \qquad \text{Equation (2-11)}$$

where R(B) and R(0) are the resistances measured with and without applying magnetic field, respectively.

2.2.4 Magnetic measurement

The Quantum Design Superconducting Quantum Interference Device-Vibrating Sample Magnetometer (SQUID-VSM) system can be used to characterize the magnetic properties of samples. The magnetic field can be tuned from 0 to 7 T and temperature from 2 to 400 K. The magnetic moment of a sample can be measured as a function of temperature (*m*-*T*) and magnetic field (*m*-*H*). In this thesis, SQUID-VSM is mainly used to measure the *m*-*T* curve of a superconductor, confirming the superconducting state and determining the T_c. Due to the Meissner effect, a magnetic field is expelled from a superconductor during its transition to the superconducting state. Therefore, strong diamagnetism is observed if the temperature is lower than T_c. Figure 2.10 shows a typical *m*-*T* curve for YBCO thin film. A clear and sharp diamagnetic transition is seen at T_c~90 K, corresponds to the T_c observed in resistance measurement.

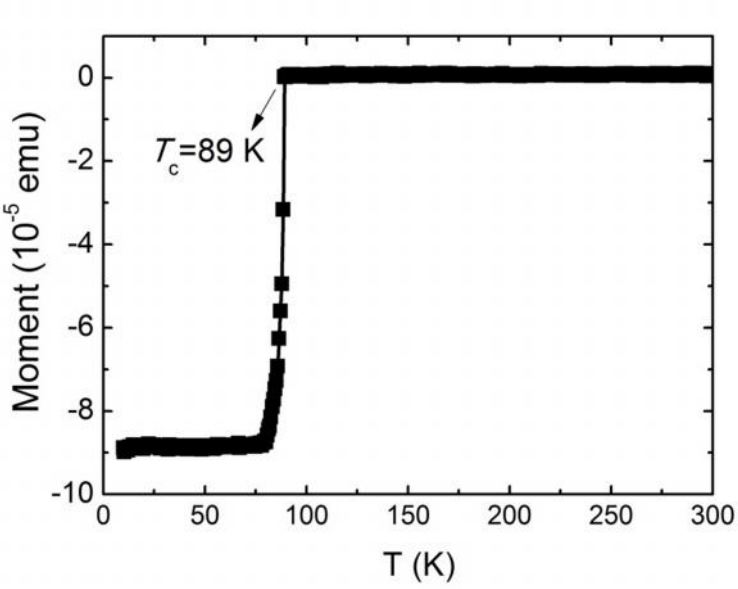

Figure 2.10 *m*-*T* curve for YBCO thin film grown on LAO substrates.

2.3 Atomic control of substrate surface

Smooth substrate surfaces terminated with a single atomic plane are essential for improving the epitaxial growth of films, especially for the two-dimensional layer-by-layer growth. In

addition, new electronic properties in heterostructures or interfaces based on atomically flat substrates may be unexpectedly observed. For example, LAO grown TiO_2-terminated STO has been shown to be highly metallic and superconducting [94, 96]. STO is the most commonly used substrate mainly because of the ability to prepare a single terminated surface. It could be achieved through acid etching and annealing techniques [125]. Firstly, STO substrates are ultrasonic treated in deionized water for 10 minutes and then dried by nitrogen gas. Secondly, the dried substrates are ultrasonically treated in buffered hydrofluoric acid solution for 30 seconds, and again dried by nitrogen gas. Finally, they are annealed in a furnace at 950 °C for 1.5 hours in air with a ramping up rate of 3 °C/min and ramping down rate of 5 °C/min. Figure 2.11(a) and (b) show the AFM image of TiO_2-terminated STO and step height profile. Clear terraces with 1 uc step height (3.905 Å) are observed.

The thermal treatment can also be applied to other substrates such as LAO (100), $DyScO_3$ (110), $NdGaO_3$ (110) and $(LaAlO_3)_{0.3}(Sr_2AlTaO_6)_{0.7}$ (100) to obtain single terminated surfaces [126-130]. Figure 2.11(c) and (d) show the surface morphology of $LaAlO_3$ (100) and $DyScO_3$ (110) treated in our lab. For LAO (100), it was annealed at 1050 °C for 2.5 hours in air with a ramping up rate of 5 °C/min and ramping down rate of 3 °C/min. For $DyScO_3$ (110), it was annealed at 1150 °C for 2.5 hours in air with the same ramping rates.

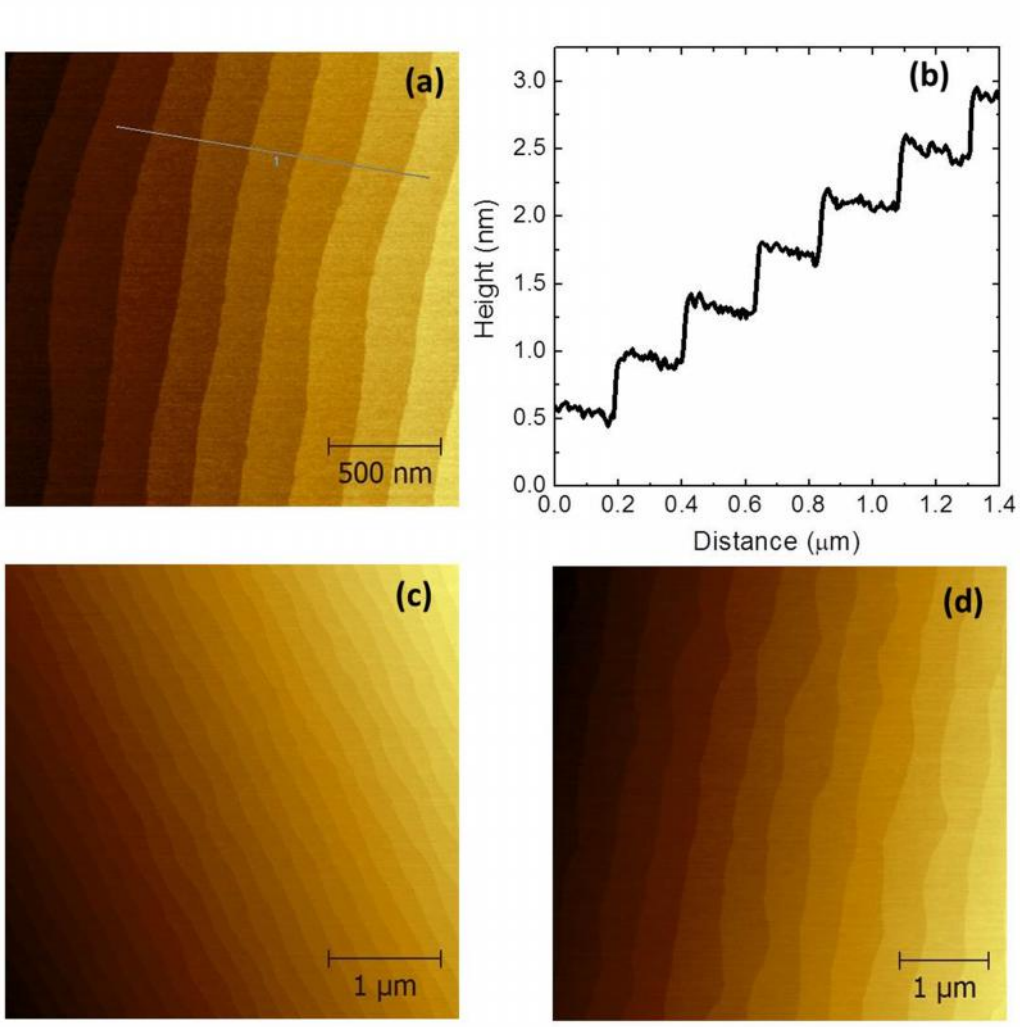

Figure 2.11 (a) AFM image of a TiO_2-terminated $SrTiO_3$ (100) substrate, (b) Step height profile corresponds to $SrTiO_3$, (c) $LaAlO_3$ (100), (d) $DyScO_3$ (110).

2.4 Device fabrication

As is discussed above, in order to accurately determine resistivity and sheet resistance, a Hall-bar device with a large length to width ratio is required. This is especially important for the determination of critical resistance in superconductor-insulator transition in this thesis. The patterning of Hall-bar device can be realized by the transfer of pattern on a mask to the wafer through lithography technique. As is shown in Figure 2.12, a layer of photoresist (it is positive photoresist in this example) is spin coated on the wafer, put under the mask and then illuminated by UV light. The photoresist in the areas not covered by the mask is exposed to

UV radiation, and thereby certain chemical/texture changes occur after the exposure. The photoresist in these areas becomes easily dissolvable in certain solvent. After removing the exposed photoresist, a pattern which is the same to the mask is transferred onto the photoresist layer.

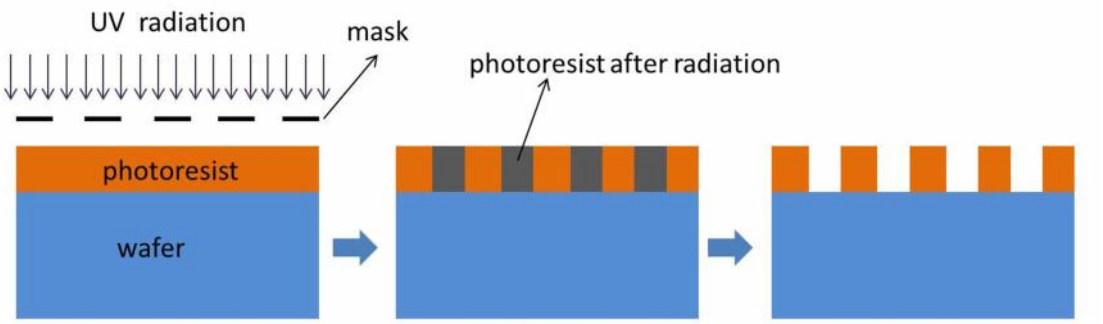

Figure 2.12 Schematic overview of pattern transfer from a mask to photoresist on sample.

The pattern on photoresist is then transferred to the thin film. The most common method is the removal of the thin film in selective area using etching techniques such as Ar-ion milling, as is shown in Figure 2.13(a). However, for substrates such as STO and TiO_2, they can be induced to be conducting by ion milling. Ion milling could not be used to pattern thin films grown on these substrates. The patterning can be realized by using an amorphous insulator as the hard mask. As is shown in Figure 2.13(b), before deposition of the thin film, an amorphous insulator such as Al_2O_3 or AlN is deposited on selective areas. The thin film is then grown on the whole substrate. If the thin film on the amorphous insulator is highly insulating, a well-defined pattern of thin film will form on the substrates. After patterning of thin films, deposition of metal electrode can also be done by photolithography and thermal evaporation. The detailed device process and the device structures for cuprate ultrathin film and LAO/STO in this thesis will be presented in chapter 4 and chapter 5, respectively.

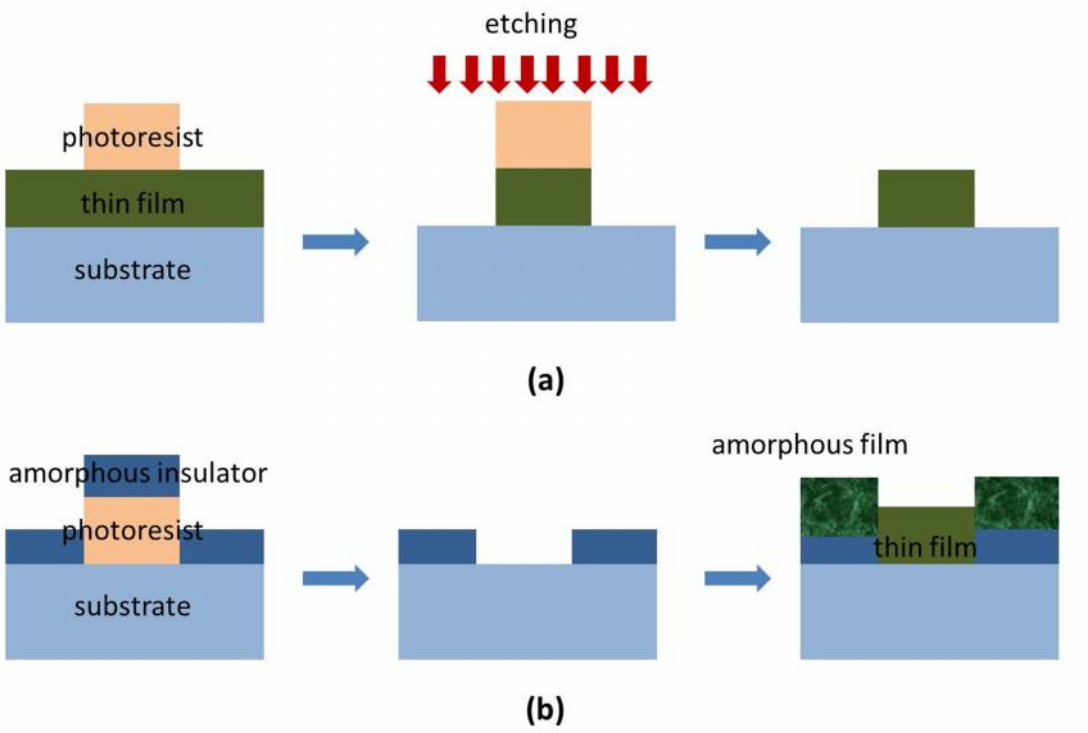

Figure 2.13 Schematic overview for patterning thin film. (a) Use etching technique (b) Use amorphous insulator as hard mask.

Chapter 3 Doping Electrons and Holes into $YBa_2Cu_3O_y$ System

In this chapter, we showed the synthesis of thin films, investigation of structure, magnetic, transport properties in ambipolar YBCO system in which both electrons and holes can be doped. By doping La and modifying the oxygen composition, $Y_{0.38}La_{0.62}(Ba_{1.64}La_{0.36})Cu_3O_y$ thin films were tuned to evolve from hole-doped superconducting phases to electron-doped metallic phases, and showed *n-p* asymmetric transport properties. Compared with the typical n-type PCCO, it is suggested that our n-type sample with highest carrier density of ~2.8×10^{21} cm^{-3} is at the very edge of the superconducting dome. In order to study the influence of La composition on ambipolar $Y_{0.38}La_{0.62}(Ba_{2-x}La_x)Cu_3O_y$ thin films, samples with La substitution for Ba of $0.14\leq x\leq0.66$ were synthesized. The resistivity and carrier density of p-type and n-type samples as a function of La doing levels were measured and compared. $Pr(Ba_{2-x}Pr_x)Cu_3O_y$ thin films were also synthesized and metallic behaviours in n-type samples were also observed.

3.1 Introduction

High-T_c superconductivity in cuprates could be induced by doping either holes (p-type) or electrons (n-type) into Mott insulators. Investigations of electron- and hole-doping asymmetry (symmetry) in cuprates should help to further our understanding of the cuprate superconductors [58, 59]. However, the typical n-p asymmetry (symmetry) investigations thus far are based on the cuprates with different crystallographic structure such as NCCO (T' structure) and LSCO (T structure). Moreover, these materials have different parent Mott insulators (Nd_2CuO_4 for NCCO and La_2CuO_4 for LSCO), and thus, exhibit different properties even without doping [123]. Therefore, it is desirable to dope electrons and holes into a single Mott insulator without changing the crystallographic structure and address the inherent n-p asymmetry (symmetry) in both sides of such 'ambipolar' cuprate.

In order to obtain ambipolar cuprates, one way is to change a material from p-type to n-type through the reduction of holes and increase of electrons, and vice versa. According to this

method, the $YBa_2Cu_3O_y$ (YBCO) system is one of the cuprates which possibly exhibits ambipolar superconductivity. The as-grown YBCO sample is a p-type superconductor with T_c of around 90 K and the oxygen composition is around 7 (y≈7). The reduction of oxygen composition in Cu-O chain causes the decrease in the hole concentration in the CuO_2 plane [30, 31]. Moreover, the substitution of trivalent elements such as La at Ba-site results in a destruction of T_c [131-134]. The destruction of T_c is attributed to the decrease in hole concentration caused by the introduction of donor electrons when La^{3+} is substituted for Ba^{2+}. Therefore, La substitution for Ba combined with the reduction of oxygen could induce the shift of available doping from hole to electron. This could open an avenue for searching an ambipolar cuprate.

In this way, Segawa *et al*. obtained ambipolar cuprate in single-crystal $Y_{1-z}La_z(Ba_{2-x}La_x)Cu_3O_y$ (x=0.26, z=0.62) with charge carriers ranging from 7% of holes per Cu to 2% of electrons per Cu [135]. Holes and electrons in this compound were obtained by varying the oxygen composition. It was also found that $Y_{0.38}La_{0.62}(Ba_{1.74}La_{0.26})Cu_3O_y$ exhibits asymmetric behaviour in magnetic ground states and transport properties between electron- and hole-doped sides [136]. However, this asymmetric comparison was limited to insulating state near the zero-doping region due to low carrier density in n-type samples. Recently, an electrochemical technique was used to remove oxygen in pure YBCO thin films and achieve n-type metallic state [137]. However, carrier density of the n-type state was still low (2.5×10^{20} cm^{-3}) and the metallic state was only observed above 120 K. Therefore, in order to fully investigate the *n-p* asymmetry (symmetry), more heavily electron-doped materials in YBCO system, which exhibit metallic and even superconducting behaviour, are desirable.

Experimentally, effective reduction of the as-grown materials is necessary to dope n-type carriers in cuprates [33, 135]. In general, the bulk single crystals are annealed at high temperature (850-1080 ^oC) in low oxygen partial pressure (P_{O2}) for tens of hours to several days. For the thin-film growth, oxygen can be removed uniformly and efficiently with post-annealing for several tens of minutes, since oxygen diffusion along the c-axis is much easier

and the diffusion lengths are comparable to the film thickness [49]. As is discussed above, besides the reduction of oxygen, La substitution for Ba in YBCO is expected to provide additional electrons. One can expect that more electrons can be doped by increasing the La content in $Y_{0.38}La_{0.62}(Ba_{2-x}La_x)Cu_3O_y$ and efficiently removing oxygen using thin-film growth method.

In this chapter, using PLD method, we grow the ambipolar cuprate $Y_{0.38}La_{0.62}(Ba_{2-x}La_x)Cu_3O_y$ and $Pr(Ba_{2-x}Pr_x)Cu_3O_y$ thin films and shift the materials from p-type superconducting to n-type metallic states.

3.2 Ambipolar conduction in $Y_{0.38}La_{0.62}(Ba_{1.64}La_{0.36})Cu_3O_y$

In this section, we grow the $Y_{0.38}La_{0.62}(Ba_{1.64}La_{0.36})Cu_3O_y$ thin films with La composition substituted for Ba of 0.36. By post-annealing in various P_{O2} and vacuum, hole- and electron-doped thin films with different carrier densities were obtained. At optimally reduced condition, a metallic n-type sample showed resistivity below Mott limit and a recorded electron density of ~2.87×10^{21} cm^{-3} at 300 K. The electrical transport properties upon changing carrier doping levels were investigated and show different behaviour between hole- and electron-doped sides.

3.2.1 Experimental procedure

The ceramic targets were prepared using the pure cation oxides powders of Y_2O_3 (99.999%), La_2O_3 (99.999%), $BaCO_3$ (99.997%) and CuO (99.9999%). These powders were weighed and mixed according to the chemical formula of $Y_{0.38}La_{0.62}(Ba_{1.64}La_{0.36})Cu_3O_y$. The mixture was then annealed at 850, 900, 900 ^oC for 10 h respectively, in air with regrinding before each annealing. Finally, the powder was pressed into disk-shaped pellet and sintered at 980 ^oC for 20 h in air. Thin films with thickness of ~260 nm were grown on (001) $LaAlO_3$ (LAO) substrates by a PLD system using the as-prepared target. LAO is used because it is fairly difficult to create oxygen vacancies inside, which is important for n-type thin films annealed

in vacuum. The deposition T and P_{O2} for all samples were 760 ^{o}C and 200 mTorr, respectively. Since we cannot measure accurately the oxygen content, we label the films annealed at different conditions by carriers per planar Cu atom which is determined by the carrier densities (from Hall measurements) and volume of primitive cell of YBCO. Three p-type samples with carrier densities (at 300 K) of p=0.019, 0.034, 0.055 holes/Cu were obtained by *in situ* postannealing in the PLD chamber at 560 ^{o}C for 20 min in P_{O2}=0.02, 0.2 and 3 Torr, respectively. P-type samples with higher carrier doping of p=0.068 and 0.145 holes/Cu were obtained by re-annealing in a tube furnace at 600 ^{o}C for 30 min in air and P_{O2}=760 Torr, respectively. N-type samples with carrier densities of n=0.02, 0.029, 0.034, 0.038 electrons/Cu were obtained by *in situ* postannealing at 640 ^{o}C in vacuum (P_{O2} <10^{-5} Torr) for 10, 30, 50 and 80 min, respectively, and then cooling down to room temperature at 30 ^{o}C/ min. In order to obtain higher electron doping of n=0.087 and 0.166, the samples annealed for 80 min were re-annealed in vacuum at 380 ^{o}C with a ramp rate of 30 ^{o}C/min for 0 min (cooled down immediately when T=380 ^{o}C) and 10 min, respectively. Note that this re-annealing process is critical for reduction of oxygen as confirmed by expansion of the c-axis (Figure 3.1 and Figure 3.6). The crystallographic structure of the thin films was measured by X-ray diffraction. The transport property measurements were made using a Quantum Design PPMS at temperatures ranging from 2 to 400 K. The resistivity was measured by four-probe method and Hall effects by Van der Pauw geometry with the applied magnetic field swept from -5 to 5 T.

3.2.2 Structural characterization using X-ray diffraction

Figure 3.1 shows the θ-2θ XRD patterns of four $Y_{0.38}La_{0.62}(Ba_{1.64}La_{0.36})Cu_3O_y$ samples annealed in air and vacuum. Only (00l) peaks of thin films and LAO substrates (indicated with S(00l)) were clearly observed, where l is an integer, confirming the c-axis oriented epitaxial growth. The c-axis lattice constant, d, of the sample annealed in air was determined to be 11.728±0.002 Å which is less than that of the as-grown (in air) crystal $Y_{0.38}La_{0.62}(Ba_{1.74}La_{0.26})Cu_3O_y$ (11.763 Å) [135]. This indicates that our samples have larger La

composition substituting for Ba and thus, possess smaller *d*, which is in fair agreement with the established empirical relation [131, 132]. In these earlier reports, it has been shown that *d* in $Y(Ba_{2-x}La_x)Cu_3O_7$ decreases as La composition is increased. As is shown in the inset of Figure 3.1, (00*l*) peaks of the samples annealed in vacuum shift to smaller angles, compared with that of sample annealed in air, suggesting an expansion of the c-axis. It is known that *d* of $YBa_2Cu_3O_y$ increases as *y* decreases [30, 31]. This supports the fact that oxygen was removed as $Y_{0.38}La_{0.62}(Ba_{1.64}La_{0.36})Cu_3O_y$ films were annealed in low P_{O2} and vaccum.

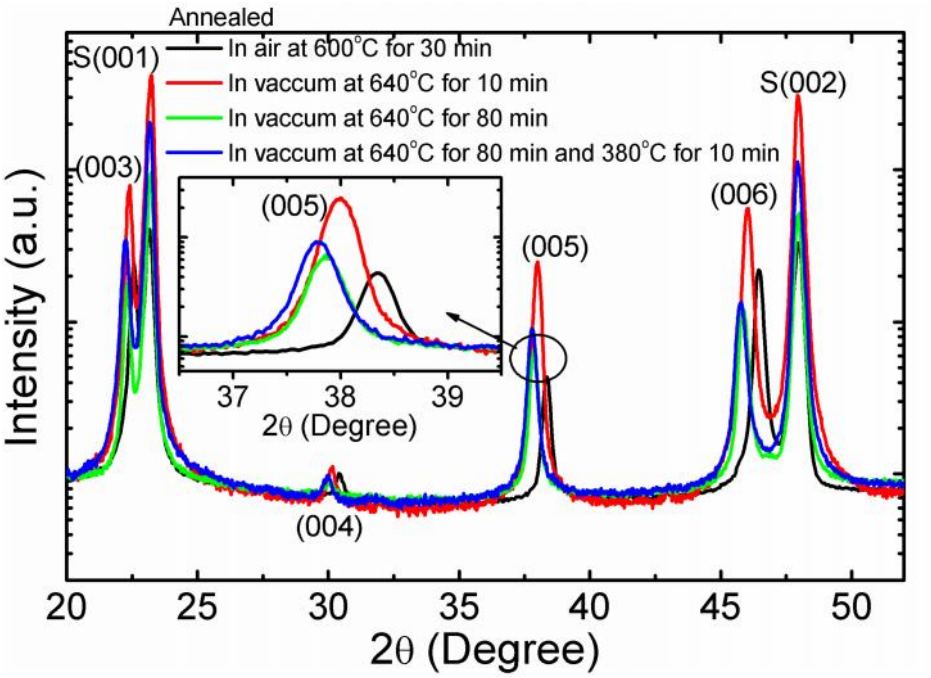

Figure 3.1 X-ray diffraction patterns of $Y_{0.38}La_{0.62}(Ba_{1.64}La_{0.36})Cu_3O_y$ thin films. Inset: (005) peaks.

3.2.3 Resistivity and Hall-effect measurements

Figure 3.2(a)-(d) show the evolution of the *T* dependence of the in-plane resistivity (ρ_{ab}) upon changing carrier doping levels at 300 K. The p- and n-type charge carriers were confirmed by Hall effects measurements in Figure 3.4. Samples with high hole-doping level show superconductivity, for example, sample with p=0.145 exhibits zero-resistance T_c of ~35 K. As *p* decreases, and thus the oxygen content in the sample reduces, T_c decreases and ρ_{ab} increases, the samples show evolution from superconductors to insulators (Figure 3.2(a)-(b)). To further

reduce oxygen content and obtain electron doping, thin films were annealed in vacuum. For low doping level, n=0.02, the sample exhibits insulating behaviour (Figure 3.2 (b)). As n increases, ρ_{ab} goes down and the samples show metallic behaviour at high T (Figure 3.2(c)-(d)), although ρ_{ab} shows an upturn at low T. In a quasi-two-dimensional system, the Mott limit for metallic transport requires that the resistivity should satisfy the condition $\rho_{ab} \leq hd/e^2$, where h is the Planck constant, e is elementary charge and d is the interlayer distance of two-dimensional system [138]. This suggests a condition $\rho_{ab} \leq 0.82$ mΩcm for metallic conduction in YBCO system with a distance between CuO_2 planes of 0.318 nm. Therefore, for n-type samples with n<0.087, the magnitude of ρ_{ab} within metallic region is above the Mott limit. Moreover, the metallic behaviour is already established at low doping level of n=0.02 (3.46×10^{20} cm^{-3}) near Mott insulating state [136] and electron-electron scatterings are dominant in transport behaviour which will be discussed in the following text. These suggest a bad metal behaviour at low doping levels in n-type La-doped YBCO system [139-141]. However, the sample with the highest electron doping level of n=0.166 is obviously metallic since ρ_{ab} is below the Mott limit from ~300 K down to the lowest T measured. The ρ_{ab} of the sample with n=0.166 (~0.88 mΩ·cm at 300 K), to the best of our knowledge, is the lowest resistivity in n-type YBCO system [135-137]. The low ρ_{ab} observed here could be due to the high carrier density, which will be shown below.

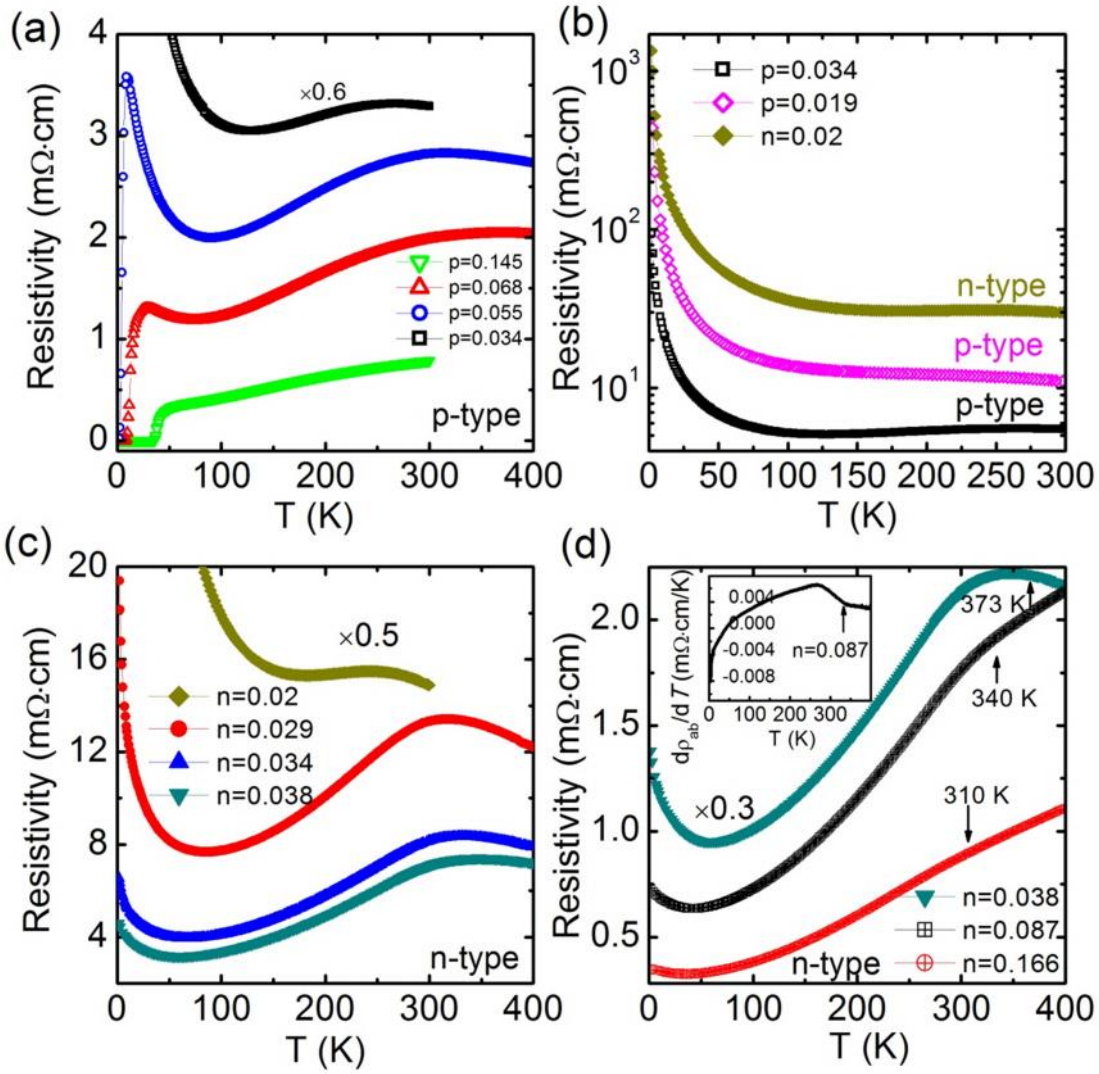

Figure 3.2 The in-plane resistivity (ρ_{ab}) as a function of temperature for p-type and n-type $Y_{0.38}La_{0.62}(Ba_{1.64}La_{0.36})Cu_3O_y$ thin films. The samples were labelled by the hole (p) and electron (n) doping at 300 K (per Cu atom), which is obtained by Hall measurement. Inset of panel (d) is the temperature derivative of ρ_{ab} for sample with n=0.087.

Figure 3.3 shows ρ_{ab} of n-type samples as a function of T^2. One can see that in a moderate-temperature range, ρ_{ab} is approximately proportional to T^2, indicating a Fermi-liquid (FL) behaviour due to electron-electron scattering [52]. Resistivity in a FL system can be described by the equation $\rho_{ab}(T)=\rho_0+A_2T^2$, where A_2 is the quadratic scattering rate. By fitting the data to this equation, we can obtain A_2 for various doping levels (Figure 3.6). It can be seen that A_2 decreases rapidly from ~8.6×10^{-5} mΩ·cm·K^{-2} to ~7.5×10^{-6} mΩ·cm·K^{-2} with increasing electron doping. This behaviour of A_2 is similar to those in NCCO as electron doping increases [142]. Interestingly, the magnitude of A_2 in our films are of the order of 10^{-6} ~ 10^{-5}

$m\Omega \cdot cm \cdot K^{-2}$ which is comparable to those in NCCO [52, 142]. The similarity in evolution and magnitude of A_2 between $Y_{0.38}La_{0.62}(Ba_{1.64}La_{0.36})Cu_3O_y$ and NCCO hints at the possibility that the electron-electron scattering in n-type cuprates is governed by essentially the same physics, regardless of the different crystallographic structures. As is marked by arrows, the FL regimes shift to lower T as the electron doping increases. It has been demonstrated that the ground state of heavily overdoped n-type cuprates is dominated by FL behaviour [143]. The shift of FL regimes probably suggests the same ground state in n-type YBCO system if electrons are overdoped. In contrast, the quadratic dependence with T of ρ_{ab} is not observed in p-type samples.

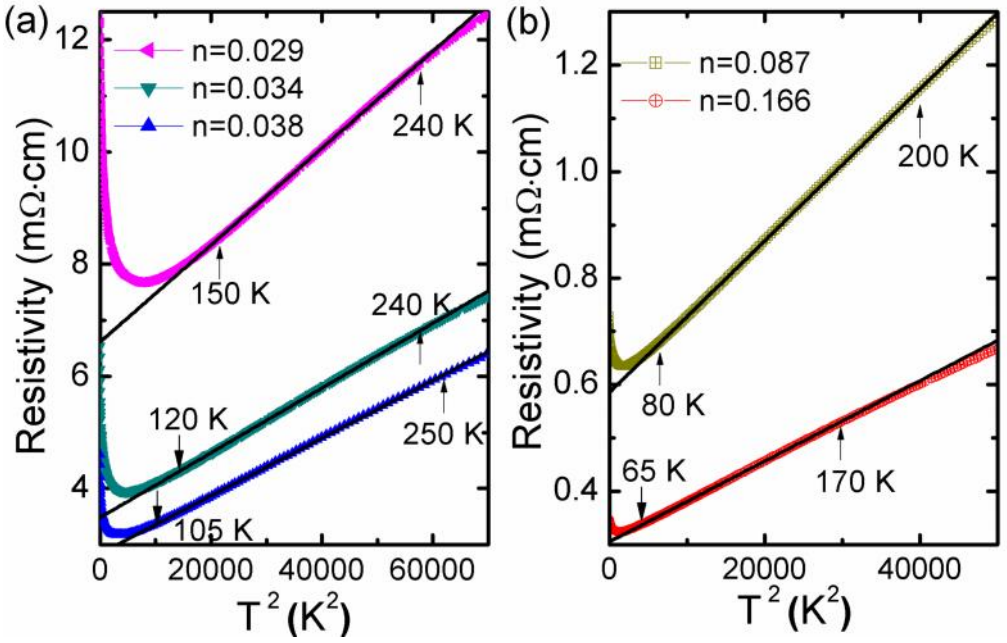

Figure 3.3 In-plane resistivity of n-type samples as a function of T^2 for the same data shown in Figure 3.2(c)-(d). Solid line is the fitting to the data. Arrows indicate the T where ρ_{ab} deviates from Fermi-liquid behaviour.

At T above ~250 K, weakening of the quadratic dependence of ρ_{ab} is observed for electron-doped samples [52]. ρ_{ab} even saturates and becomes non-metallic at higher T for doping $n \leq 0.038$, as is shown in Figure 3.2. For n=0.087 and n=0.166, ρ_{ab} tends to saturate at higher T although it is metallic up to 400 K. The saturation of ρ_{ab} can also be observed in p-type samples. On close examination, for samples with $n \geq 0.038$, ρ_{ab} begins to decrease rapidly at

around the T marked by arrow (T_ρ) with decreasing T. T_ρ can be obtained by the T derivative of ρ_{ab} and is around the T where $d\rho_{ab}/dT$ starts to increase [144], as is shown in the inset of Figure 3.2(d).The steep decrease of ρ_{ab} is also observed in underdoped $Nd_{2-x}Ce_xCuO_4$ with x=0.025-0.075 and is related to the formation of pseudogap confirmed by optical spectra [144, 145]. In $Nd_{2-x}Ce_xCuO_4$, T_ρ decreases as x increases and disappears at optimal doping of x=0.15. In our samples, T_ρ also decreases with increasing electron doping. Importantly, the anomalies in ρ_{ab} become less noticeable at higher electron doping which is similar to NCCO. Whether the pseudogap begins to evolve below T_ρ requires further investigation by optical spectroscopy. Nevertheless, the anomalies in ρ_{ab} of n-type films suggest the possibility of its being a precursor of superconductivity.

Figure 3.4 shows the Hall coefficients (R_H). The samples annealed in vacuum exhibit negative R_H all the way below 300 K, indicating electron doping. The electron density of optimally reduced sample is ~2.87×10^{21} cm^{-3} (R_H ~ -0.00217 cm^3/C) at 300 K which is one order of magnitude higher than those in $Y_{0.38}La_{0.62}(Ba_{1.74}La_{0.26})Cu_3O_y$ single crystal (~2.2×10^{20} cm^{-3}, R_H ~ -0.028 cm^3/C) [135] and pure YBCO film (~2.5×10^{20} cm^{-3}) [137]. The magnitude of R_H in the insulating film with n=0.02 (R_H ~ -0.018 cm^3/C at 300 K) increases more sharply at low T, which is similar to that of the single crystal with near electron doping (R_H ~ -0.028 cm^3/C at 300 K) [135]. Furthermore, ρ_{ab} at 300 K of our thin film exhibits similar value (~ 29 mΩ·cm) to that in single crystal (~ 30 mΩ·cm) at this similar doping level [135]. These suggest that the crystal quality of our thin films is comparable to that of single crystal. As is shown in Figure 3.6, d continuously increases by hole depletion and electron doping across the zero-doping state, although it is moderate at higher electron-doping region, which indicates that electrons were continuously doped as oxygen was removed. Therefore, high carrier density and low ρ_{ab} in n-type thin films are caused by electron doping.

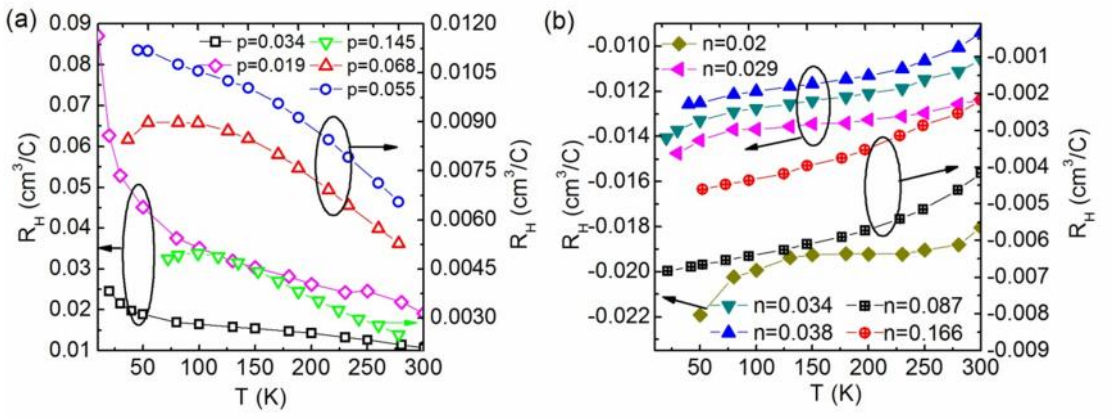

Figure 3.4 The Hall coefficient R_H of p-type (a) and n-type (b) $Y_{0.38}La_{0.62}(Ba_{1.64}La_{0.36})Cu_3O_y$ thin films as function of temperature.

To further indicate that electrons in our films predominantly originate from the intrinsic doping, not from random defects, we performed the core level x-ray photoemission spectroscopy (XPS) measurements. Figure 3.5 shows the XPS spectra of electron-doped n=0.034 and hole doped p=0.055 thin films taken at 300 K for Cu 2p core levels. The width of the main peak (at ~933 eV) of the Cu 2p core level spectrum for n-type film is found to be narrower than that for p-type film, suggesting the replacement of Cu^{2+} by Cu^{+} since the main peak of Cu^{+} is known to be sharper than that of Cu^{2+} [146]. Moreover, the intensity of the charge-transfer satellite (at ~943 eV) for n-type film is weaker than that for p-type film also suggests the replacement of Cu^{2+} by Cu^{+} since satellite peak has been observed in Cu^{2+} compounds but not in Cu^{+} compounds [146]. These results further indicate that electrons are indeed doped into thin films when annealed in vacuum in the way one would expect and not due to some random defects [146]. From the discussion above, the high carrier density and low in-plane resistivity of n-type samples are indeed caused by electron doping with reduction of oxygen.

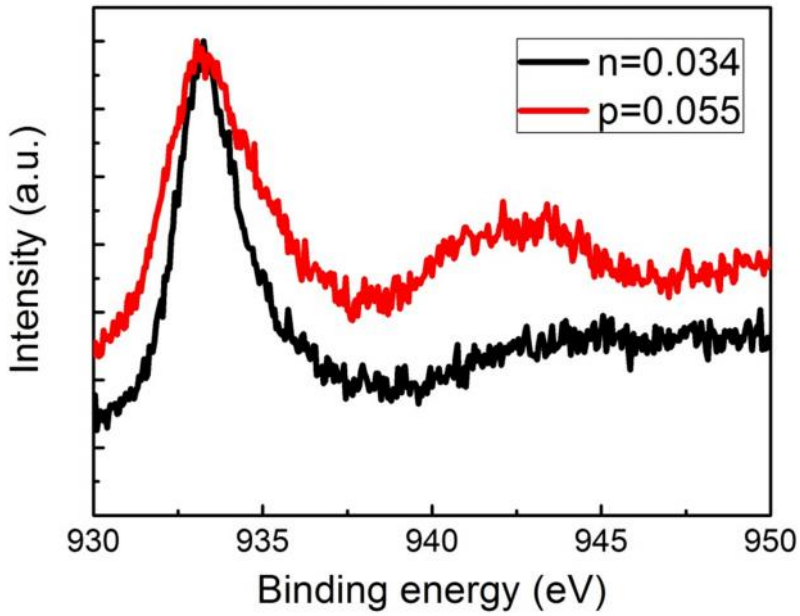

Figure 3.5 XPS spectra of electron-doped n=0.034 and hole doped p=0.055 thin films at 300 K for Cu 2p core levels.

To put the electron density measured by us in perspective, we compare our results with those in the typical n-type cuprates $Pr_{2-x}Ce_xCuO_4$ (PCCO). PCCO with x=0.12, which starts to exhibit superconductivity, shows a carrier density of ~4.6×10^{21} cm^{-3} (R_H ~ -0.0014 cm^3/C) at 300 K [49]. Therefore, the electron density (~2.87×10^{21} cm^{-3}) of the optimally reduced thin film in our work is close to that of the underdoped PCCO with x=0.12. Moreover, PCCO with x=0.1 shows metallic behaviour from room temperature down to ~70 K and below this temperature it shows insulating behaviour due to weak localization [147]. It has been observed that the temperature below which underdoped n-type cuprates show insulating behaviour decreases with increasing doping levels [144]. For our thin films, at the highest electron doping level, the metallic behaviour persists from 400 K down to lower temperature of ~38 K (Figure 3.3(d)). These observations suggest that our n-type thin films are at the very edge of the superconducting dome.

3.2.4 'Phase diagram'

In Figure 3.6, we compare T_c, temperature with minimum resistivity T_{min}, d and A_2 as a function of carrier density at 300 K (n_{300K}) for both n- and p-type thin films. This could be considered as a phase diagram. The existence of T_{min} is found in all samples with metallic state, even in superconducting p-type samples, in which ρ_{ab} exhibits insulating-like behaviour below T_{min} with minimum ρ_{ab}. This behaviour has been investigated in underdoped cuprates but its origin is still unclear [147-149]. T_{min} was found to share the same evolution as a function of doping in both n- and p-type thin films, mainly decreasing with increasing n_{300K}. However, T_{min} decreases much more rapidly in n-type samples, from 181.8 K at $n_{300K}=3.46\times10^{20}$ cm^{-3} to 57.9 K at $n_{300K}=6.65\times10^{20}$ cm^{-3}, than that in p-type samples, from 127.7 K at $n_{300K}=5.8\times10^{20}$ cm^{-3} to 73.7 K at $n_{300K}=1.18\times10^{21}$ cm^{-3}. At higher electron doping, T_{min} exhibits a slight drop and tends to saturate. Superconductivity emerges at $n_{300K}=9.5\times10^{20}$ cm^{-3} (T_c=2 K) when T_{min}=89.7 K in p-type samples and T_c increases with decreasing T_{min}. However, superconductivity was not observed in n-type samples even if T_{min} was much lower than 89.7 K and the doping level of electrons was higher than that of holes. Interestingly, it was found that the amplitude of A_2 exhibits the same evolution as T_{min} with electron doping, suggesting an intimate relationship between electron-electron scattering and the metal-insulator transition in n-type YBCO system.

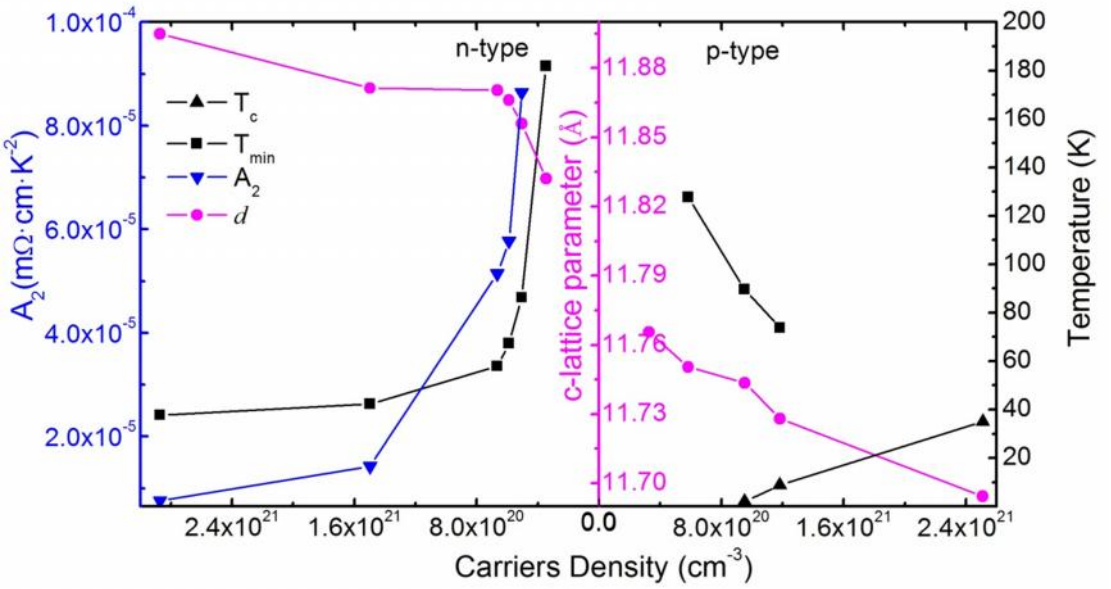

Figure 3.6 Superconductivity transition temperature T_c, temperature with minimum resistivity T_{min}, c-lattice parameter d and quadratic scattering rate A_2 as a function of carriers density at 300 K. T_{min} is obtained by calculating the derivatives $d\rho_{ab}/dT$ and is the temperature when $d\rho_{ab}/dT=0$. A_2 is obtained from fitting $\rho_{ab}(T)=\rho_0+A_2T^2$ to data within $\rho_{ab}\propto T^2$ region shown in Figure 3.3.

3.2.5 Summary

The La-doped YBCO thin films were grown by the PLD system and subsequently post-annealed in different P_{O2} and vacuum to achieve ambipolar cuprates. At high P_{O2} the sample $Y_{0.38}La_{0.62}(Ba_{0.64}La_{0.36})Cu_3O_y$ showed superconductivity and it was confirmed by Hall-effect measurements that the charge carriers were p-type. As the P_{O2} decreased, the resistances increased and the samples evolved from superconductors to insulators. This is because the reduction of P_{O2} causes the reduction of hole densities. In order to obtain n-type carriers, the samples were annealed in vacuum ($P_{O2}<10^{-5}$ torr) at different times and the n-type charge carriers were confirmed by Hall-effect measurements. As the electron densities increased, the n-type samples evolved from insulating behaviour to metallic behaviour at the moderate-temperature range. These indicate that ambipolar conductivity in YBCO system can be obtained by reduction of oxygen and introduction of La. At the optimally reduced condition, the sample showed a high electron density of ~2.8×10^{21}cm^{-3} and the ρ_{ab} below the Mott limit,

indicating the occurrence of a metallic state. The metallic samples showed quadratic T dependence on ρ_{ab} at moderate T range and resistivity anomaly at higher T. These characteristics are similar to those of the typical electron-doped cuprate NCCO and could be due to the existence of a Fermi-liquid state and pseudogap. The p-type thin films also showed metallic behaviour, but the T^2-dependent resistivity and anomaly were not observed, suggesting *n-p* asymmetry in YBCO system.

3.3 The influence of La substitution and oxygen reduction in ambipolar cuprate $Y_{0.38}La_{0.62}(Ba_{2-x}La_x)Cu_3O_y$

In section 3.2, by changing oxygen composition, p-type superconducting states and n-type metallic states with different doping levels have been obtained in $Y_{0.38}La_{0.62}(Ba_{1.64}La_{0.36})Cu_3O_y$ thin films. For n-type thin films at optimally reduced condition, the metallic behaviour was observed from 400 K down to ~38 K and the electron density is as high as $\sim 2.87\times10^{21}$ cm^{-3} at 300 K. Compared to PCCO, it can be suggested that our n-type samples are at the very edge of the superconducting dome. The higher electron density enabled the expansion of *n-p* asymmetric study to higher hole and electron doping levels. This study is based on the sample with La composition substituting Ba of 0.36. It could be expected that higher La^{3+} substitution for Ba^{2+} could introduce more electrons in YBCO system. In these ways, different La doping in YBCO gives rise to extensive interest. In this section, we synthesized both p- and n-type $Y_{0.38}La_{0.62}(Ba_{2-x}La_x)Cu_3O_y$ thin films with different x and investigated the structure and transport properties.

3.3.1 Experimental procedure

Similar to the previous section, for target preparation, pure cation oxides powders of Y_2O_3, La_2O_3, $BaCO_3$ and CuO were weighed and mixed according to the chemical formula of $Y_{0.38}La_{0.62}(Ba_{2-x}La_x)Cu_3O_y$. The mixture was then annealed at 850, 900, 900 ^oC for 10 h respectively, and at 980 ^oC for 20 h in air with regrinding between annealings. On the final annealing, the powder was pressed into disk-shaped pellet for the PLD process. Thin films

with thickness of 170-400 nm were grown on LAO (100) substrates by a PLD system using the as-prepared target. The deposition T and P_{O2} for all samples were 760 ^{o}C and 200 mTorr, respectively. P-type samples were obtained by cooling down to room T at 30 ^{o}C/min in P_{O2}=3 Torr, and then re-annealing in a tube furnace at 500 ^{o}C for 30 min in oxygen atmosphere. Effective reduction of the as-grown materials is necessary to dope n-type carriers in cuprates. The reduction of thin films was carried out by doing annealing in vacuum in PLD chamber. Since we cannot measure accurately the oxygen content, in order to get optimally reduced condition, we conducted the annealing until the resistivity stopped to decrease. In the present work, the annealing procedure includes two steps. Firstly, *in situ* post-annealing was done at 640 ^{o}C in vacuum (P_{O2} <10^{-5} Torr) for 30-80 min, depending on the thickness of the thin films, and then cooling down to room temperature at 30 ^{o}C/ min. Secondly, the samples were put into PLD chamber again and re-annealed in vacuum at 380 ^{o}C for 10-20 min with a ramp rate of 30 ^{o}C/min. Hall-effect measurements were performed for all samples and the signs of the Hall coefficients (R_H) confirmed that the charge carriers were p-type for all samples annealed in oxygen and n-type for all samples annealed in vacuum. The thickness of the thin films was determined by scanning electron microscope (SEM) image of the cross section of the samples. The crystallographic structure of the thin films was analyzed by XRD. The transport properties measurements were made using PPMS system.

3.3.2 Structural characterization using X-ray diffraction

Figure 3.7(a) shows the XRD θ-2θ patterns of p-type $Y_{0.38}La_{0.62}(Ba_{2-x}La_x)Cu_3O_y$ samples with different x. Only (00l) peaks of thin films and (00l) peaks of LAO substrates (indicated with S(00l)) were clearly observed, where l is integer, confirming the c-axis oriented epitaxial growth. From the XRD measurement, it is hard to find a second phase in the thin films. We cannot rule out the local inhomogeneity in the thin films, which means there possibly exists La-rich and La-poor phases, or the phase in which Y is substituted for Ba. If Y is substituted for Ba, there will be a phase $La(Ba_{2-x}Y_x)Cu_3O_y$, instead of $La(Ba_{2-x}La_x)Cu_3O_y$. To rule out the substitution of Y at the Ba sites, we compare the tolerance factor t of these two phases.

Tolerance factor can be used as numerical criteria of the stability of perovskite-like materials, and is defined as [131, 150]

$$t = \frac{r_{La}/3 + x r_{RE}/3 + (2-x) r_{Ba}/3 + r_O}{\sqrt{2}(r_{Cu} + r_O)}$$

for $La(Ba_{2-x}RE_x)Cu_3O_y$ system, where RE is lanthanide element such as La and Y substituted for Ba, r_{La}, r_{RE} , r_{Ba}, r_{Cu} and r_O are the radii of ions La, RE, Ba, Cu and O. Since the r_{La} is larger than r_Y, the tolerance factors in $La(Ba_{2-x}La_x)Cu_3O_y$ are higher than those in $La(Ba_{2-x}Y_x)Cu_3O_y$, suggesting that the material in which La is substituted for Ba is more stable than that Y substituted for Ba. Moreover, since r_{La} is comparable to r_{Ba}, the solubility x is very large in the system in which La is substituted for Ba [131, 150]. These mean that the substitution of La for Ba is easy and the possibility of inhomogeneity is small. Moreover, the p-type thin films show small values in full width at half-maximum (FWHM) of (005) rocking curves, 0.34^o-0.42^o for samples with $0.14 \le x \le 0.4$ and 0.74^o-0.99^o for samples with $0.46 \le x \le 0.66$, suggesting that the crystalline quality and homogeneity is good (Figure 3.9(a)). As is shown in Figure 3.7(b), (00*l*) peaks shift to larger angles as x increases, indicating a shortening of the *c*-axis. The *c*-axis lattice constants (*d*) of p-type thin films as a function of x are plotted in Figure 3.7(c). It is observed that d decreases with the increase of x monotonically, which is in fair agreement with the established empirical relation in $YBa_{2-x}La_xCu_3O_y$ polycrystalline pellets [131, 132]. This may further suggest that La is substituted for Ba at Ba-site gradually and homogeneously as x is increased in the present thin films.

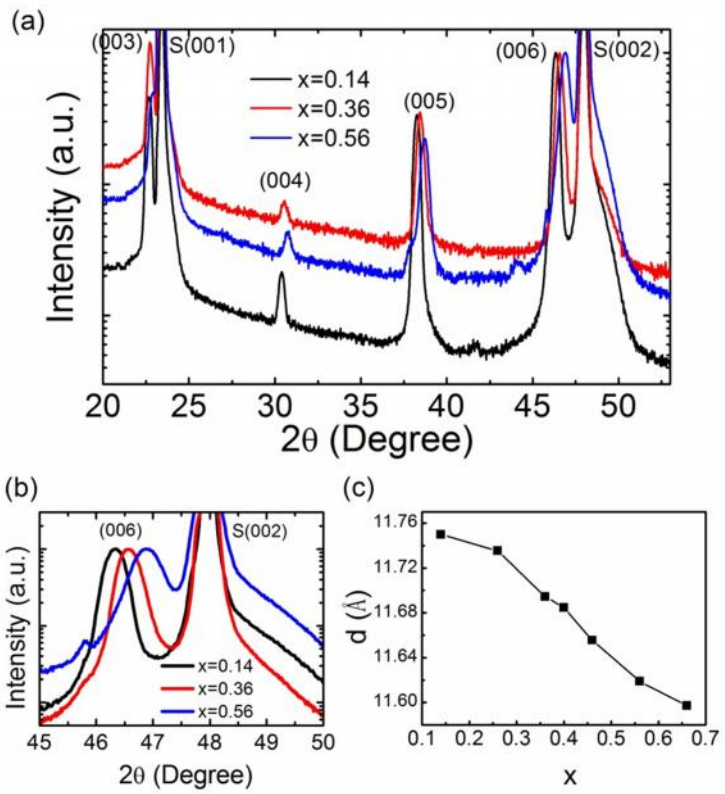

Figure 3.7 (a) XRD θ-2θ patterns of p-type $Y_{0.38}La_{0.62}(Ba_{2-x}La_x)Cu_3O_y$ thin films with x=0.14, 0.36, 0.56. (b) (006) peaks and substrate (002) peaks. (c) c-axis lattice constants, d, as a function of x for p-type samples. The scan step is 0.02°.

In order to reduce oxygen content and obtain n-type charge carriers, thin films were annealed in vacuum. Figure 3.8 shows (006) peaks for examples with x=0.14, 0.36 and 0.56 annealed in oxygen ambient and vacuum. The (006) peaks of the samples annealed in vacuum shift to smaller angles, compared with that of sample annealed in oxygen ambient, indicating an expansion of the c-axis. It is known that d of $YBa_2Cu_3O_y$ increases as y decreases [30, 31]. This supports the fact that oxygen was removed when $Y_{0.38}La_{0.62}(Ba_{2-x}La_x)Cu_3O_y$ films were annealed in vacuum. Note that the n-type thin films still show clear (00l) peaks (Figure 3.1), even though the FWHM of rocking curves show higher values compared with those of p-type thin films (Figure 3.9(b)). For example, (005) peaks of p- and n-type samples with x=0.36 show the FWHM of 0.42° and 1.3°, respectively. The increase of FWHM in n-type samples may be due to the disorder caused by oxygen vacancies.

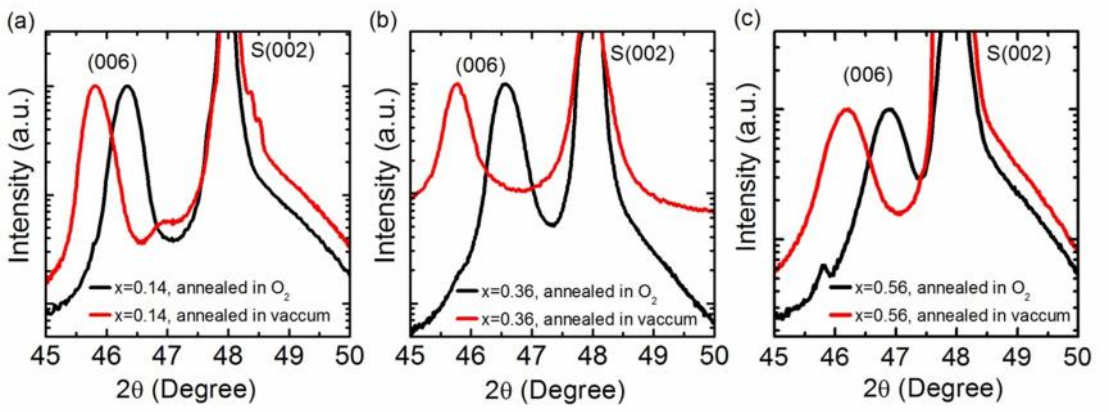

Figure 3.8 (006) peaks of thin films and (002) peaks of substrates with x=0.14, 0.36 and 0.56 annealed in oxygen ambient and vacuum.

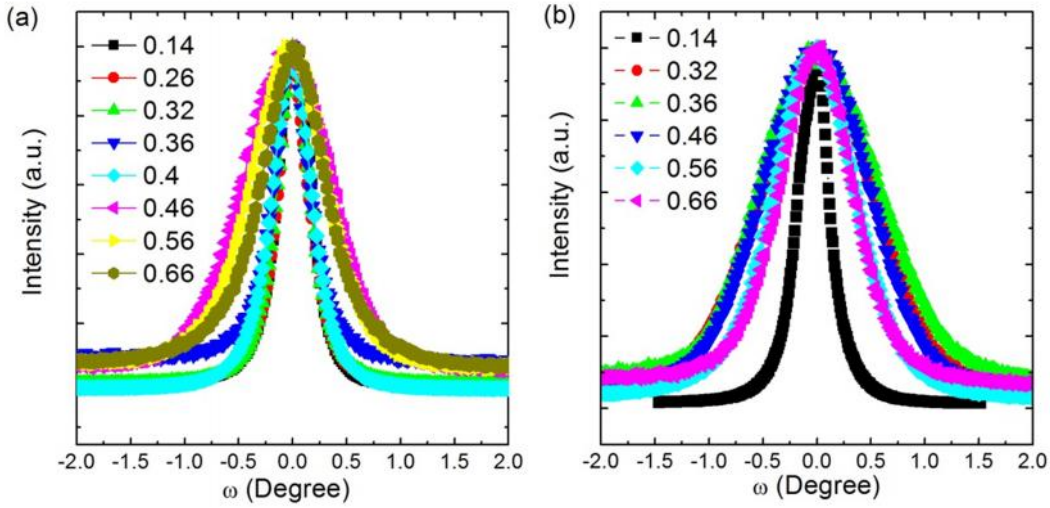

Figure 3.9 Rocking curves on (005) peaks of $Y_{0.38}La_{0.62}(Ba_{2-x}La_x)Cu_3O_y$ thin films with different *x* for (a) p-type samples and (b) n-type samples.

Figure 3.10 shows reciprocal space mappings (RSMs) for a p-type $Y_{0.38}La_{0.62}(Ba_{2-x}La_x)Cu_3O_y$ thin film with *x*=0.36, measured by coplanar diffraction geometry. This measurement was performed using X-ray Demonstration and Development (XDD) beamline at Singapore Synchrotron Light Source (SSLS). The lattice constants are based on that of LAO substrate, pseudo-cubic crystal structure with the reciprocal lattice unit (r.l.u.) of $2\pi/3.79$ Å^{-1} along H, K and L, respectively. In Figure 3.10, the RSMs around $(002)_{HL}$, $(002)_{KL}$, $(\bar{1}03)_{HL}$, and $(013)_{KL}$ for the sample are shown. From Figure 3.10(a) and (b), it can be seen that the peaks for the thin film are right below the LAO substrate peak. This means that there is no tilt between the

thin film and LAO substrate. One can see that the absolute values of H (Figure 3.10(c)) and K (Figure 3.10(d)) for the peaks of thin films are equal and they are at the same height of L. This indicates that the in-plane lattice constants, *a* and *b* for the thin film are equal, meaning that the crystal structure of the thin film is tetragonal. The La doping level of this sample is 0.36, comparable to that (x≈0.4) of polycrystalline $YBa_{2-x}La_xCu_3O_7$, at which an orthorhombic to tetragonal structure transition occurs [132].

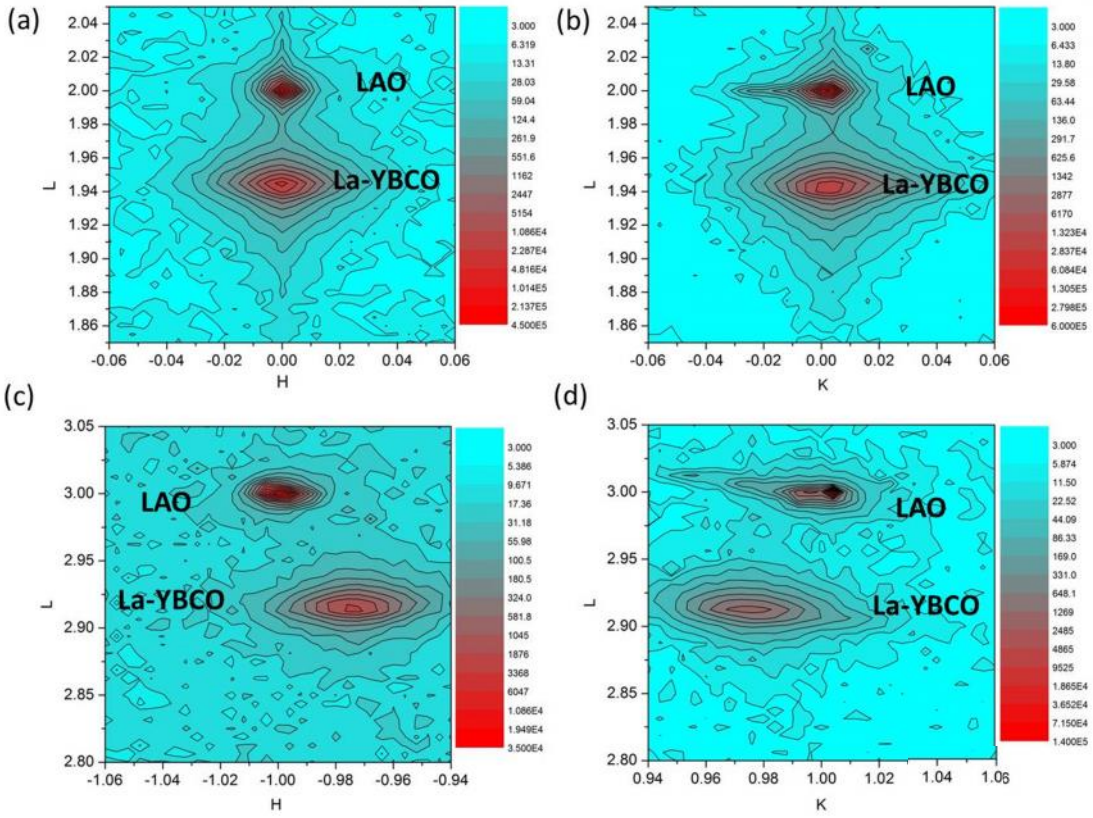

Figure 3.10 Reciprocal space mappings around (a) $(002)_{HL}$, (b) $(002)_{KL}$, (c) $(\bar{1}03)_{HL}$, and (d) $(013)_{KL}$ are indexed in the lattice with *a*, *b*, and *c* for a p-type $Y_{0.38}La_{0.62}(Ba_{2-x}La_x)Cu_3O_y$ thin film with x=0.36.

3.3.3 Electrical transport and magnetization measurements

Figure 3.11 shows the in-plane resistivity (ρ_{ab}) as a function of T for p-type thin films with different x. For x<0.46, the thin films show metallic behaviour in normal state and metal-to-superconductor transition at low T. For x≥0.46, the thin films exhibit semiconducting behaviour. As is shown in Figure 3.14, zero-resistance T_c decreases from 54.7 K at x=0.14 to

23 K at x=0.4. The in-plane resistivity at 300 K (ρ_{300K}) mainly increases as the La doping increases within the whole doping regime. The evolutions of T_c and ρ_{ab} are similar to those in polycrystalline $YBa_{2-x}La_xCu_3O_y$ [131, 132]. This can be attributed to the difference in the valence states of La^{3+} and Ba^{2+}, and thus, the substitution of La^{3+} for Ba^{2+} would introduce donor electrons which partially compensate holes within the CuO_2 planes.

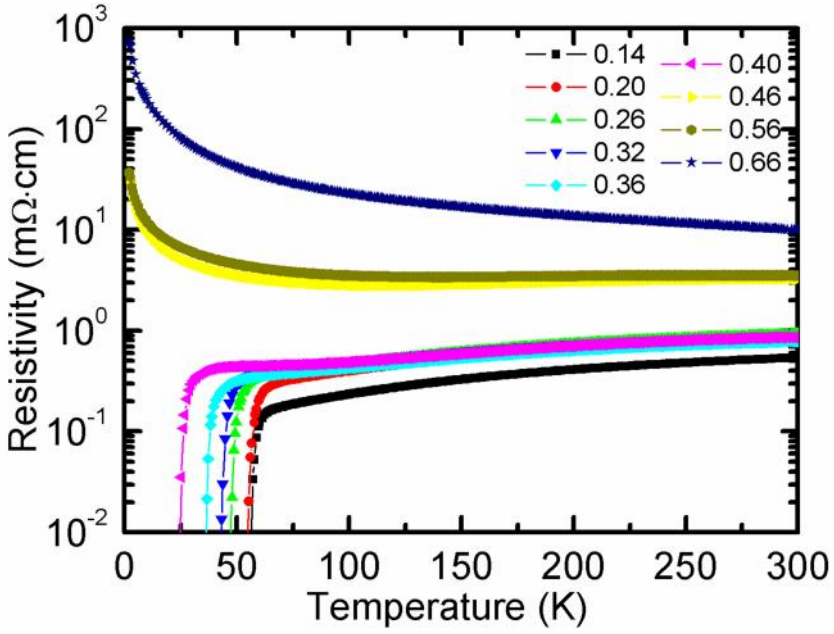

Figure 3.11 The in-plane resistivity (ρ_{ab}) as a function of temperature for p-type $Y_{0.38}La_{0.62}(Ba_{2-x}La_x)Cu_3O_y$ thin films with different *x*.

Figure 3.12 shows the magnetic moment as a function of temperature for p-type $Y_{0.38}La_{0.62}(Ba_{2-x}La_x)Cu_3O_y$ thin films with *x*=0.26, 0.32 and 0.36. Strong diamagnetic signals below T_c are clearly observed and the T_c is comparable to that observed in resistivity-temperature curves. These further confirm the superconductivity in the p-type samples.

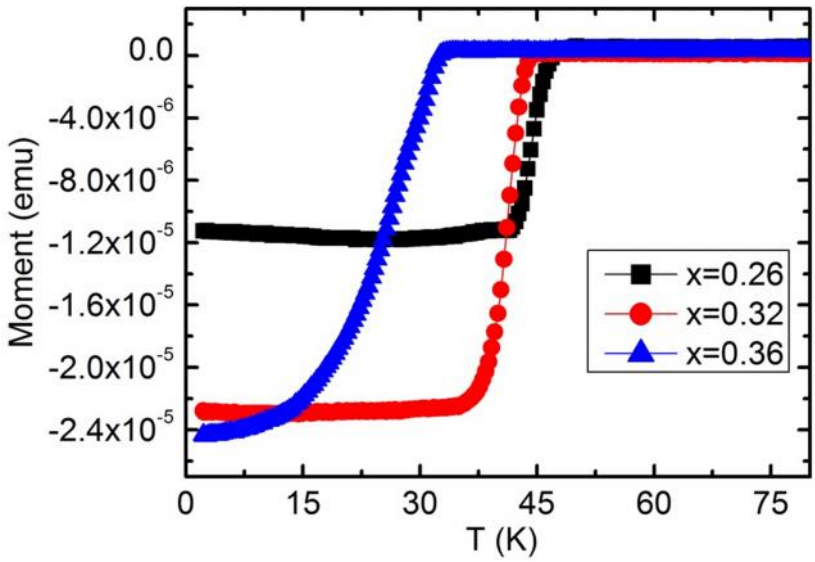

Figure 3.12 The magnetic moment as a function of temperature for p-type $Y_{0.38}La_{0.62}(Ba_{2-x}La_x)Cu_3O_y$ thin films with different *x*.

Figure 3.13 shows the ρ_{ab} as a function of *T* for n-type thin films with different *x*. The n-type charge carriers were confirmed by Hall-effect measurements which exhibited negative R_H. Within the whole doping regime, the samples show metallic behaviour at moderate *T*, although ρ_{ab} shows an upturn at low *T*. For samples with $0.32 \leq x \leq 0.46$, metallic behaviour appears within a larger *T* range, from 300 K down to ~40 K, compared to the n-type pure YBCO thin films obtained by an electrochemical technique [137]. In the n-type pure YBCO films, the metallic behaviour appears only above 120 K. As is shown in Figure 3.14, as *x* is increased the ρ_{300K} slightly decreases and reaches a minimum of ~1 mΩ·cm at x=0.36. At higher La doping level the ρ_{300K} increases sharply, going up to ~14 mΩ·cm at x=0.66. It should be expected that more electrons are introduced, and thus, resistivity decreases as the La content is increased. However, this is in contrast to the behaviour observed in the present work, which can probably be explained by the charge compensation due to an increase of oxygen content. For $Y_{0.38}La_{0.62}(Ba_{2-x}La_x)Cu_3O_y$ thin films with $x \leq 0.36$, it is easy to get low *y* and the *y* values are near the same. Therefore, electron doping is dominated by La composition and ρ_{300K} decreases with increasing *x*. However, for thin films with $x \geq 0.36$, low enough *y* cannot be achieved and the lowest *y* obtained is higher than that in thin films with

$x \leq 0.36$. Thus, the donor electrons introduced by La^{3+} are compensated by holes introduced by oxygen, which may result in the increase of ρ_{300K} for higher x. Interestingly, it has been observed that in polycrystalline $YBa_{2-x}La_xCu_3O_y$ annealed in the same oxygen ambient, y remains near 7.0 for $x \leq 0.4$, and exceeds 7.0 and increases with increasing x for $x \geq 0.4$ [132]. The La content (x=0.4) in polycrystalline $YBa_{2-x}La_xCu_3O_y$ which separate $y \approx 7.0$ and $y > 7.0$ regions is near to that (x=0.36) in the present n-type thin films which show lowest ρ_{300K}. This probably suggests that the difficulty in achieving low y in the La-rich thin films is due to the high y in the as-grown samples. Therefore, a balance between x and the achievable lowest y is critical to obtain high carrier concentration in n-type thin films. As is presented in Figure 3.14, the n-type samples with $0.32 \leq x \leq 0.46$ show low and similar ρ_{300K}, indicating that it is possible to obtain a balance between x and the lowest y within this x regime.

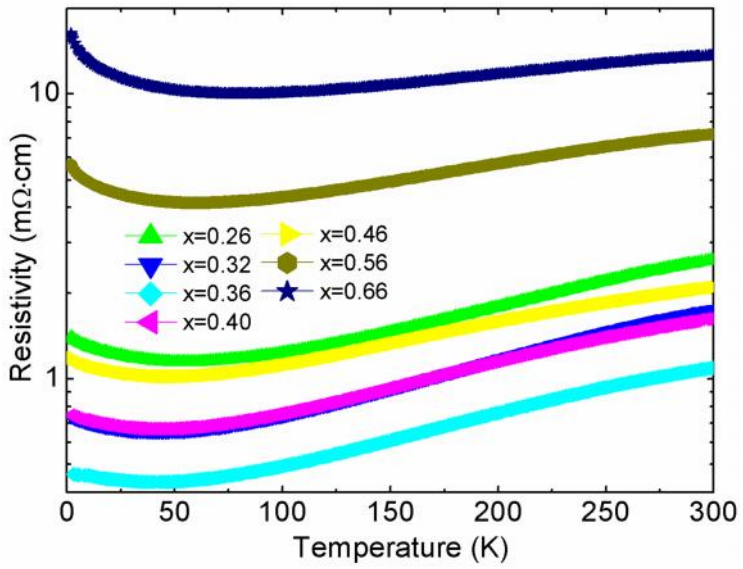

Figure 3.13 ρ_{ab} as a function of temperature for n-type $Y_{0.38}La_{0.62}(Ba_{2-x}La_x)Cu_3O_y$ thin films with different x.

The carrier densities at 300 K (n_{300K}) obtained from R_H for p- and n-type samples are also presented in Figure 3.14. As x is increased, n_{300K} shows a monotonic decrease in p-type samples and a peak region ($0.32 \leq x \leq 0.46$) in n-type samples. This behaviour could be due to the introduced donor electrons and charge compensation, which is consistent with ρ_{300K} as

was discussed above. The highest n_{300K} in n-type sample is ~3×10^{21} cm^{-3} (sample with x=0.36) which is one order of magnitude higher than those in optimally reduced $Y_{0.38}La_{0.62}(Ba_{1.74}La_{0.26})Cu_3O_y$ single crystal (~2.2×10^{20} cm^{-3}, R_H ~ -0.028 cm^3/C) [135, 136] or pure YBCO film (~2.5×10^{20} cm^{-3}) [137]. This can be also seen in the discussion of Figure 3.4. The high electron density observed here could be due to the fact explained as follow. The d of $Y_{0.38}La_{0.62}(Ba_{2-x}La_x)Cu_3O_y$ films increases with decreasing y. For films with x=0.36, d of p-type sample (annealed in oxygen and y is near 7) and n-type sample are 11.694 Å and 11.885 Å, respectively. The difference in d is ~0.19 Å which is comparable to that (~0.16 Å) in $YBa_2Cu_3O_y$ with y=7 and y=6 [9]. These indicate that y in the n-type film is near 6, which means the oxygen in Cu-O chain has been completely removed. In this way, La substitution for Ba with x=0.36 gives electron density of ~2.07×10^{21} cm^{-3} (0.36 electrons in one unit cell and the unit-cell volume of $YBa_2Cu_3O_7$ of ~173.56 $Å^3$ is used) which is slightly less than but similar to the measured value. The additional carriers which contribute to the higher measured carrier density could be as a result of the itinerant electrons induced by oxygen vacancies in CuO_2 planes. The proposal that itinerant electrons in CuO_2 planes cause conduction has been reported in electron-doped YBCO thin films [137]. Note that disorders caused by oxygen vacancies in CuO_2 planes may also result in charge localization in n-type films which will be discussed in the following text.

One may assume that further reduction could dope more electrons into $Y_{0.38}La_{0.62}(Ba_{2-x}La_x)Cu_3O_y$ thin films. However, the heavily-reduced thin films, annealed for longer time, show higher ρ_{ab} and lower n_{300K}. Although oxygen atoms in Cu-O chains are predominantly removed when samples are annealed in low-P_{O2} environment, we cannot rule out the possible oxygen vacancies in CuO_2 planes, which mean partial oxygen atoms in CuO_2 planes are also pulled out. Moreover, it is found that the heavily-reduced thin films exhibit rough surfaces due to microscopic decomposition spots. The FWHM of (005) XRD rocking curve shows larger value in the heavily-reduced thin films, suggesting degradation of crystalline quality. Therefore, the increase in ρ_{ab} for the heavily-reduced samples may be due to the disorders

caused by oxygen vacancies in CuO_2 planes and microscopic decomposition spots. The fact that disorder produced near or in the CuO_2 plane causes a serious reduction of conductivity and T_c has been observed in other cuprates [151, 152]. It is found that the n-type samples show insulating-like behaviour below the T with minimum ρ_{ab}, indicating that the electron transport suffers from a localization effect due probably to the disorder in CuO_2 planes. This behaviour has also been observed in underdoped NCCO [147, 148]. Therefore, further optimization of reduction procedure, which avoids disorder effect and decomposition, is required to reach n-type superconductivity in YBCO system.

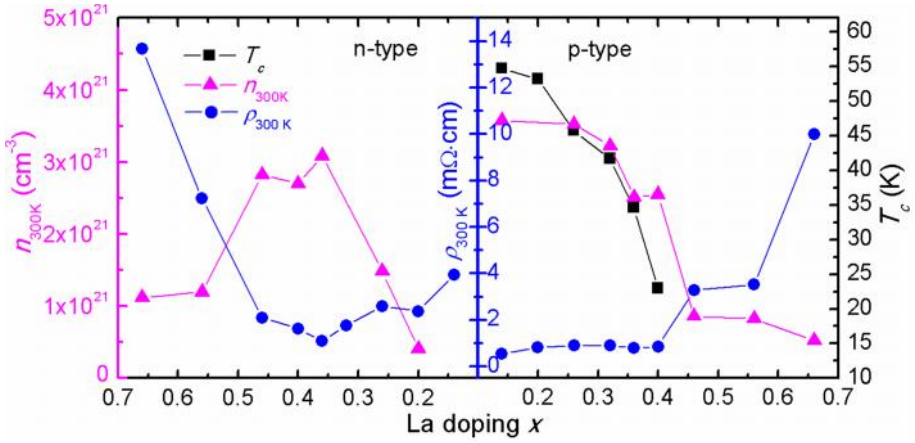

Figure 3.14 T_c, carrier density at 300 K (n_{300K}) and in-plane resistivity at 300 K (ρ_{300K}) as a function of x for n-type and p-type $Y_{0.38}La_{0.62}(Ba_{2-x}La_x)Cu_3O_y$ thin films.

3.3.4 Summary

In summary, hole- and electron-doped $Y_{0.38}La_{0.62}(Ba_{2-x}La_x)Cu_3O_y$ thin films with different x were synthesized and investigated. As x was increased the p-type samples showed a superconductor-to-insulator transition at x=0.46, an increase in ρ_{300K} and decrease in n_{300K} at room temperature, indicating that the donor electrons introduced by the substitution of La^{3+} for Ba^{2+} cancel partial holes within the CuO_2 planes. At optimally reduced condition, the n-type samples showed low ρ_{300K} and high n_{300K} for $0.32 \leq x \leq 0.46$ and relatively higher ρ_{300K} and lower n_{300K} for $x<0.32$ and $x>0.46$. The higher ρ_{300K} and lower n_{300K} in n-type samples with high La doping level could probably be attributed to the charge compensation caused by an

increase of oxygen content. The present results suggest that a balance between the La composition and the achievable lowest oxygen composition, and avoiding disorder in CuO_2 planes could be critical to induce high electron density and n-type superconductivity in La-doped YBCO system.

3.4 Metallic behaviour in electron-doped $Pr(Ba_{2-x}Pr_x)Cu_3O_y$

3.4.1 Introduction

Impurity substitution has been extensively investigated in the YBCO systems since these materials allow a much larger variation of their composition. Besides the compounds with the element substitution in the Ba sites and oxygen reduction, as were shown in last two sections, compounds with element substitution in the Y sites are also interesting and were synthesized shortly after the discovery of YBCO compound. Substitution of various lanthanide elements such as La, Nd, Sm and Eu for Y in YBCO leaves the compounds isostructure and isoelectronic, and general superconductivity with T_c ~ 90 K [153-155]. However, Pr, Ce and Tb substitutions show exceptions, suppression of T_c was observed. Among them, YBCO compound with Pr was most extensively studied since single-phase compound with Pr can be synthesized at any ratio of Pr composition, while for compounds with Ce and Tb, it is hard to obtain single-phase samples [156, 157]. In mixed $Y_{1-x}Pr_xBa_2Cu_3O_7$ compounds, T_c monotonically decreases with increasing Pr composition x, and at x≈0.6, superconductivity disappears [156, 158]. Several possible mechanisms have been proposed to explain the suppression of T_c in $Y_{1-x}Pr_xBa_2Cu_3O_7$, such as hole filling, magnetic pair breaking, hole localization, hybridization for Pr:4f-O:2p orbitals, and so on [159]. Among them, the models of hole filling and pair breaking by magnetic scattering are frequently studied and they have been indicated by experiments. In $Y_{1-x}Pr_xBa_2Cu_3O_7$, the hole concentration in the CuO_2 planes is reduced under Pr doping since Pr ion carries a valence state higher than 3^+ which Y^{3+} ion possesses. To test this hypothesis, the compounds $Y_{1-x-y}Ca_yPr_xBa_2Cu_3O_7$ were studied [160]. In this study, substitution of Pr causes the reduction of holes and thereby the reduction of T_c,

due to the higher valence states of Pr^{4+}, compared with that of Y^{3+}. However, Ca substitution has the opposite effect since Ca^{2+} has a lower valence state. Thus, at certain Pr composition, increasing the Ca composition causes an increase in T_c. However, the maximum T_c at optimal Ca doping level could not reach that in YBCO and it decreases with increasing Pr composition. This could be due to the pair-breaking effect caused by magnetic scattering of holes in CuO_2 planes on the less localized 4f moments of Pr.

From the discussion above and previous experiment [156], it is known that $PrBa_2Cu_3Oy$ (PBCO) with fully oxidization (y≈7) has much lower hole concentration than YBCO and shows insulating behaviour. Moreover, one way to obtain ambipolar cuprates is to change a material from p-type to n-type through the reduction of holes and increase of electrons, and vice versa. This has been shown in previous section in La-doped YBCO compound with La substitution for Ba. Therefore, one could expect that oxygen reduction and Pr substitution for Ba in PBCO can introduce electrons. In this section, we synthesized $Pr(Ba_{2-x}Pr_x)Cu_3O_y$ thin films with different *x*. At reduced condition, the samples are electron-doped and show metallic behaviour.

3.4.2 Resistivity and Hall-effect measurements

The experimental procedure is similar to the one in La-doped YBCO thin films, as is shown in last two sections. Briefly, the ceramic targets were prepared using the pure cation oxides powders of Pr_6O_{11}, $BaCO_3$ and CuO. Thin films were grown on LAO (100) substrates by a PLD system. The deposition temperature and oxygen pressure (P_{O2}) for all samples were 760 ^oC and 200 mTorr, respectively. P-type samples were obtained by post-annealing in oxygen and n-type samples in vacuum (P_{O2} <10^{-5} Torr) in PLD chamber. The p-type and n-type charge carriers were confirmed by Hall-effect measurements.

Figure 3.15(a) shows in-plane resistivity ρ_{ab} as a function of temperature for PBCO thin films annealed in oxygen and vacuum. The sample annealed in oxygen, as is expected, is p-type material confirmed by the positive Hall coefficient (R_H), as is shown in Figure 3.15(b). The

carrier density at 300 K is 1.59×10^{20} cm^{-3} (R_H=0.039 cm^3/C), which is much lower than that (~1×10^{22} cm^{-3}) of YBCO at optimal doping level [161]. Due to low carrier density, the sample shows highly insulating behaviour. The resistance increases sharply with decreasing temperature, and is out of measurement limit below 50 K. The PBCO film annealed in vacuum, even without Pr substitution in Ba sites, shows lower resistivity than that annealed in oxygen, and is n-type material confirmed by negative R_H (Figure 3.15(b)). A weak metallic behaviour is observed at high temperature regime and an insulating behaviour transition occurs below 195 K. The electron density at 300 K is 2.34×10^{20} cm^{-3} (R_H= -0.0267 cm^3/C). For $YBa_2Cu_3O_y$ compound, hole density decreases as the oxygen composition is reduced. At y=6, $YBa_2Cu_3O_6$ compound is considered as the parent insulator and no free charge carrier is expected. However, for $PrBa_2Cu_3O_y$ in our results, holes disappear and electrons present as oxygen is reduced. This is because the valence state of Pr is higher than 3^+, electrons introduced by Pr compensate a fraction of the holes, and thus, the hole density is low. Reducing oxygen content causes further decrease of hole density, and at certain oxygen content which is higher than 6 (y>6), holes are completely compensated. Further reducing oxygen will introduce electron in the system. This result further suggests the hole filling model for the suppression of superconductivity in PBCO system.

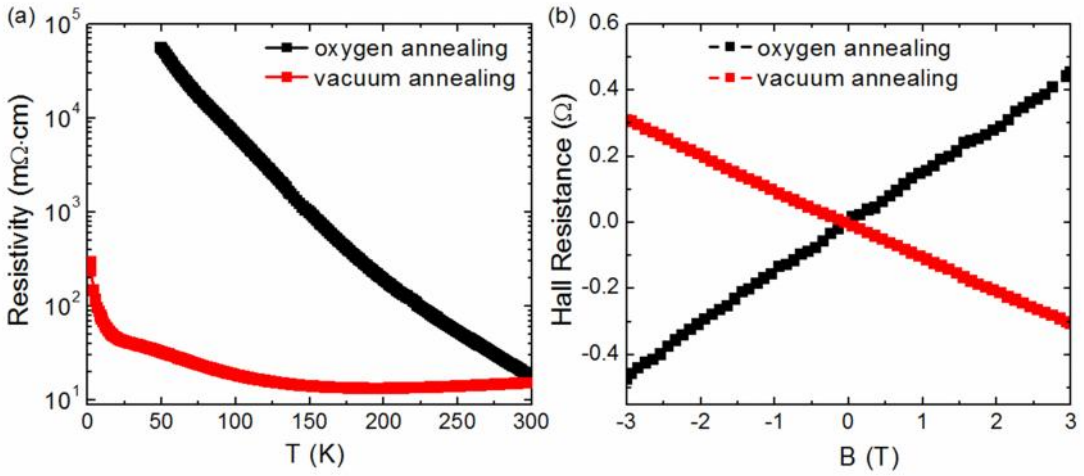

Figure 3.15(a) In-plane resistivity ρ_{ab} as a function of temperature for $PrBa_2Cu_3O_y$ thin films annealed in oxygen and vacuum. (b) Hall resistance at T=300 K as a function of magnetic field.

To further increase the electron doping levels, Pr was substituted for Ba in PBCO thin films. Figure 3.16 shows ρ_{ab} as a function of temperature for electron-doped $Pr(Ba_{2-x}Pr_x)Cu_3O_y$ thin films with different *x*. One can see that ρ_{ab} decreases with increasing *x* from 0 to 0.22. For samples with *x*=0.2 and 0.22, clear metallic behaviour is observed from 300 down to ~38 K. Below 38 K, a slight resistance upturn is observed, probably due to weak localization. For samples with *x*>0.22, even though metallic behaviour still presents at high temperature regime, they show higher ρ_{ab} with increasing *x*. The highest carrier density of ~6×10^{20} cm^{-3} at 300 K is obtained in sample with x=0.22. Pr composition (0.22) which replaces Ba in $Pr(Ba_{2-x}Pr_x)Cu_3O_y$ with highest electron density is lower than La composition (0.36) which replaces Ba in La-doped YBCO sample with highest electron density. This may be due to the proposals that valence state of Pr ion is higher than that in La^{3+}, or charge compensation caused by an increase of oxygen content in $Pr(Ba_{2-x}Pr_x)Cu_3O_y$ as x>0.22, as is discussed in section 3.3. However, highest electron density in $Pr(Ba_{2-x}Pr_x)Cu_3O_y$ is lower than that (~2.87×10^{21} cm^{-3} at 300 K) in La-doped YBCO system shown in section 3.2 and 3.3. This suggests that other mechanisms related to electron doping in $Pr(Ba_{2-x}Pr_x)Cu_3O_y$ need to be further explored.

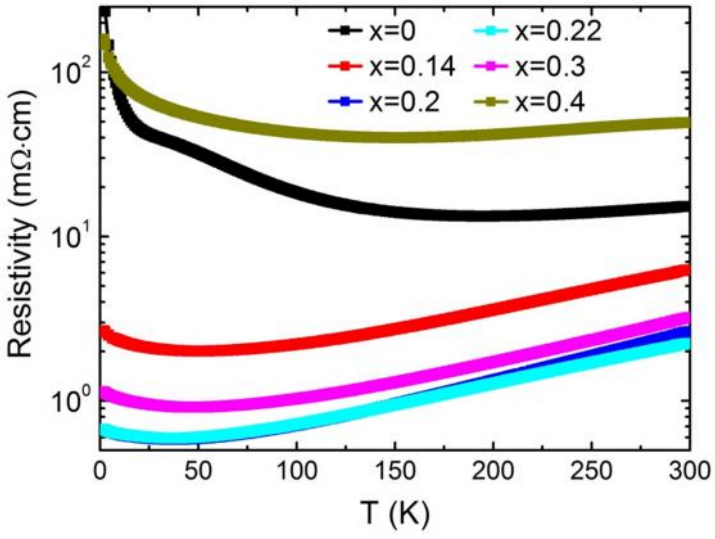

Figure 3.16 In-plane resistivity as a function of temperature for electron-doped $Pr(Ba_{2-x}Pr_x)Cu_3O_y$ thin films with different *x*.

3.4.3 Summary

Electron-doped $Pr(Ba_{2-x}Pr_x)Cu_3O_y$ thin films with different *x* were synthesized by PLD system. At reduced condition, PBCO thin films with electrons as the charge carriers were confirmed by Hall effect measurement, suggesting the hole filling model for the suppression of superconductivity in PBCO system. To further increase the electron doping levels, Pr was substituted for Ba in $Pr(Ba_{2-x}Pr_x)Cu_3O_y$ thin films. The resistivity decreases with increasing Pr doping level for $0 \leq x \leq 0.22$, but increases for $x > 0.22$. The increase in resistivity at high Pr doping levels is probably due to charge compensation caused by an increase of oxygen content. Moreover, it was found that all n-type samples show metallic behaviour at moderate temperature.

Chapter 4 Superconductor-insulator transition in an electron-doped cuprate $Pr_{2-x}Ce_xCuO_4$

In this chapter, we performed electric field effect using electronic double layer transistor (EDLT) configuration, to quasi-continuously tune the carrier density in an electron-doped cuprate $Pr_{2-x}Ce_xCuO_4$ and cause a two-dimensional superconductor-insulator transition (SIT). The resistance-temperature curves and carrier densities at different gate voltages were measured. The magnetic field-induced SITs in superconducting EDLTs at three different doping levels were also performed. The transport data at low temperature were analysed via finite-size scaling. It was suggested that SITs induced both by electric and magnetic fields are quantum phase transitions and the transitions are governed by percolation effects-quantum mechanical in the former and classical in the latter case. The SITs occurred at critical sheet resistances much lower than the pair quantum resistance $R_Q=h/(2e)^2=6.45$ kΩ. The existence of fermionic excitations at the insulating side near SITs, which may cause the lower critical resistances, was discussed.

4.1 Introduction

Quantum phase transition (QPT) is the phase transition between the ground states of a physical system governed by quantum fluctuations. One classical example is superconductor-insulator transition (SIT) in two-dimensional (2D) limit which can be induced by varying external tuning parameters such as disorder (thickness), magnetic field and carrier concentration. Finite-size scaling analysis has been a successful method in describing QPT based on nonzero temperature data [23, 24, 67-69]. Basically, for a 2D system, the sheet resistance, R_s, near a quantum critical point collapses onto a single scaling function, $R_s(x_t,T)=R_cF(|x_t-x_c|T^{-1/\nu z})$, where T is temperature, x_t is tuning parameter, x_c is x_t at critical point, R_c is critical R_s at $x_t=x_c$, ν is the correlation length critical exponent, z is the dynamic critical exponent, and $F(u)$ is a universal function of u with $F(u)\rightarrow 1$ when $u\rightarrow 0$.

There are two scenarios, bosonic and fermionic, to explain the 2D superconductor-insulator QPT. In the bosonic scenario, the SIT is driven by quantum phase fluctuations. At the superconducting side, the Cooper pairs (bosons) are mobile while vortices are localized, resulting in zero resistance. At the insulating side, the vortices are mobile while the Cooper pairs are localized, resulting in a finite resistance. The perfect duality between Cooper pairs and vortices predicts that R_c is equal to pair quantum resistance, $R_Q=h/(2e)^2=6.45$ kΩ. In the fermionic scenario, the SIT is driven by amplitude fluctuations. Cooper pairs condense to support superconductivity at the superconducting sides, while they are broken and the fermionic excitations (unpaired electrons) are localized at the insulating side. In fermionic scenario, the value of R_c may be different from R_Q.

In conventional superconductors, disorder- and magnetic field (B)-induced SITs have been observed at R_Q, suggesting the existence of Bose-condensed vortices and localized electron pairs at the insulating phase [66, 70, 71, 79, 80]. However, the B-induced SITs could also occur at a R_c much lower than R_Q, such as in the case of *a*-MoGe, likely due to the presence of fermionic excitations [67]. These suggest rich physics in 2D-SIT. Investigating SITs in other superconductors and SITs induced by other parameters could help to further our understanding of such phenomena.

In the cuprate family, since the high-T_c superconductivity is caused by charge doping into parent Mott insulators, the carrier-induced SIT is of particular interest. Continuous tuning of carrier density by electric field effect is necessary for investigation of such phase transition [6, 9, 68, 162]. This could be enabled by using ionic liquids and polymer electrolyte as gate dielectrics in electronic double layer transistors (EDLTs), which can induce large amount of carriers at an interface [13]. The capability of EDLTs in accumulating charge carriers has been demonstrated by gate-induced phase transition in various materials [13-18, 21-24, 26, 163]. In hole-doped cuprates $La_{2-x}Sr_xCuO_4$ (LSCO) and $YBa_2Cu_3O_{7-x}$ (YBCO), EDLT-tuned 2D-SIT occurred at R_Q [23, 24], which suggests that mobile vortices dominate the transport at the insulating side near SIT as opposed to fermionic excitations. Further, evidence for a 2D-

QPT has been seen in the hole-doped system via finite size scaling analysis. However, so far there is, to the best of our knowledge, no report on electric field-induced SIT in electron-doped cuprates. As a counterpart of LSCO, the electron-doped $R_{2-x}Ce_xCuO_4$ (RCCO, R=Pr, Nd, Sm or Eu) exhibits different crystalline structures, phase diagrams and electronic properties [49]. These suggest that SIT in n-type cuprates may be expected to be different. Understanding the nature of carrier-induced SIT and the QPT in electron-doped cuprates should shed more light on mechanisms of superconductivity in cuprates. Further, as the SIT strongly depends also on the dynamics of the vortices, it would be revealing if *B*-induced SIT could be studied, as one suppresses the superconductivity via vortices as opposed to charge injection. *B*-induced SITs in cuprates have been investigated in chemically doped superconductors [75, 76]. Unlike chemical doping, superconductivity induced by EDLT has a distinct 2D nature, due to the short screening length in cuprates [23, 164]. *B*-induced SIT in such EDLT superconducting state would be very interesting. However, this has not been done in hole-doped cuprates due to the huge upper critical field H_{c2}. In electron-doped cuprates H_{c2} is much lower and this provides an opportunity to study *B*-induced SIT in superconducting EDLT.

In this chapter, we demonstrate that SIT in an electron-doped cuprate $Pr_{2-x}Ce_xCuO_4$ ultrathin film can be induced by ionic liquid-assisted electric field effect. An R_c with value lower than R_Q is observed and a 2D-QPT is suggested by scaling analysis. Magnetic field-induced SIT was also done at three electric field-induced superconducting states. It is found that the R_c shows much lower value and depend on doping levels. The results suggest that fermionic excitations contribute to the conduction at the insulating side near SIT. Moreover, finite-size scaling analysis indicates that SIT induced both by electric and magnetic field is governed by percolation effects.

4.2 Experimental

4.2.1 Field effect device using an ionic liquid as a dielectric material

The ionic liquid (IL) used in this thesis is N, N-diethyl-N-methyl-N-(2-methoxyethyl)ammonium bis(trifluoromethyl sulphonyl)imide (DEME-TFSI). In an IL-assisted field effect device, the IL is considered as a dielectric material and contacts both the sample surface and the gate electrode. Upon applying a gate voltage, for example with negative bias on the sample as shown in Figure 4.1(a), cations in the IL can move towards the sample surface and anions move towards the gate electrode. Accordingly, the cations accumulate on the sample surface, and thus, negative charge carriers are induced in a thin layer near the sample surface. The cations and the induced charge carriers form an electric double layer (EDL). IL-based electric field effect transistors are usually called electronic double layer transistor (EDLTs). Figure 4.1(b) shows the optical micrograph of an EDLT device in our study and the measurement circuit. It consists of a Hall-bar structure which is used to accurately determine the sheet resistance, and a large-area planar gate electrode which allows for field focusing. During measurements, an IL droplet is put on the sample, and covers and connects the gate electrode with the Hall bar. Figure 4.1(c) shows a schematic diagram of the cross section of the EDLT device corresponding to Figure 4.1(b).

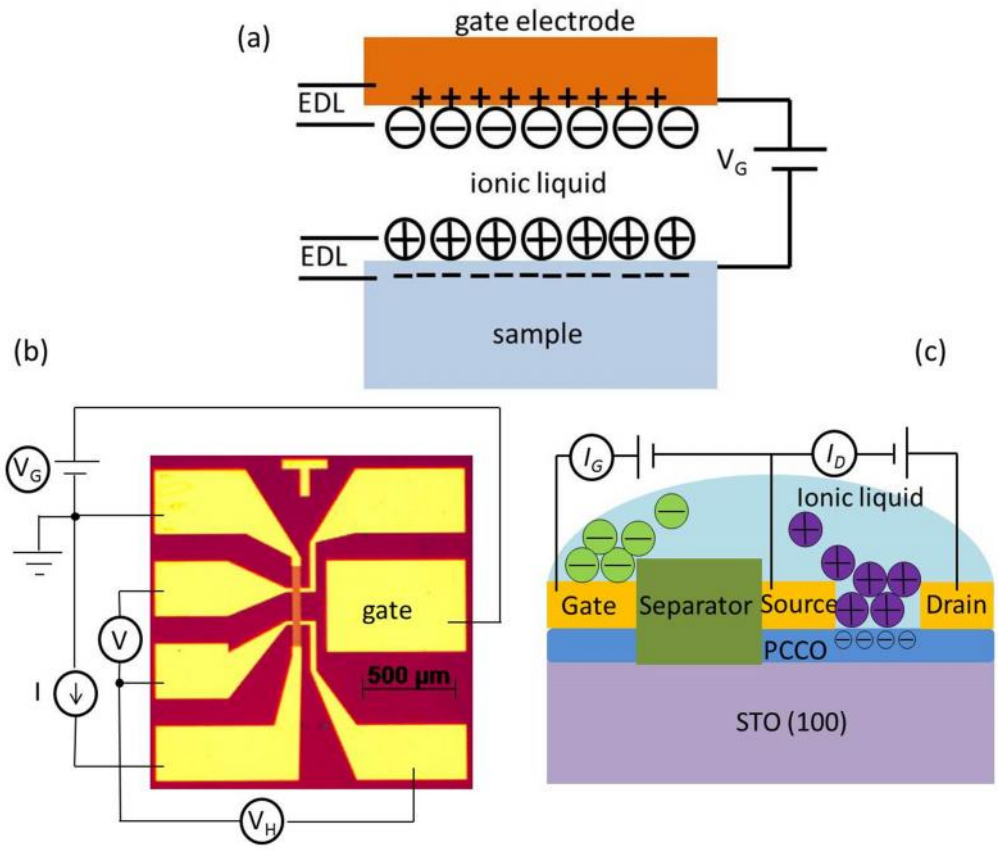

Figure 4.1. (a) Schematic diagram of the operation of ionic liquid-based electronic double layer transistors (EDLT). (b) Optical micrograph of a typical device in our study and the measurement circuit. (c) Schematic diagram of the cross section of EDLT device.

4.2.2 Thin film growth

For the preparation of $Pr_{2-x}Ce_xCuO_4$ (PCCO) ceramic targets, pure cation oxides powders of Pr_6O_{11}, CeO_2 and CuO were weighed and mixed according to the chemical formula. The mixture was then annealed at 850 and 900 ^oC for 15 h, respectively, in air with regrinding before each annealing. Finally, the powder was pressed into disk-shaped pellet and sintered at 950 ^oC for 20 h in air. The thin films were grown on TiO_2-terminated $SrTiO_3$ (001) substrates by pulsed laser deposition (PLD) system. To get TiO_2-terminated surfaces, $SrTiO_3$ (STO) substrates were treated in buffered hydrofluoric acid solution and annealed in air for 1.5 hours at 950 ^oC [125]. After treating, the STO substrates show atomically flat surfaces, as is shown in Figure 2.11 in chapter 2. Furthermore, STO has a lattice constant of 3.905 Å, which is

comparable to that (~3.95 Å) of PCCO [33, 34]. These are crucial for synthesizing PCCO thin films with smooth surfaces and high crystal quality.

For the growth of thick films with thickness of 120 nm, they were deposited at 790 ^{o}C under oxygen pressure (P_{O2}) of 0.25 mbar and then cooled down to room temperature in vacuum (P_{O2}<10^{-4} mbar) at the rate of 20 ^{o}C/min. Figure 4.2(a) shows in-plane resistivity as a function of temperature for $Pr_{2-x}Ce_xCuO_4$ with different Ce doping level x. As is expected, with increasing Ce doping, resistivity decreases and PCCO evolves from insulator to superconductor. Figure 4.2(b) shows the linear-scale resistivity-temperature curve for PCCO at optimal doping level. One can see that the normal-state resistivity exhibits quadratic temperature dependence at moderate temperature range and sharp superconducting transition at low temperature, which is consistent with previous report on electron-doped cuprates [52].

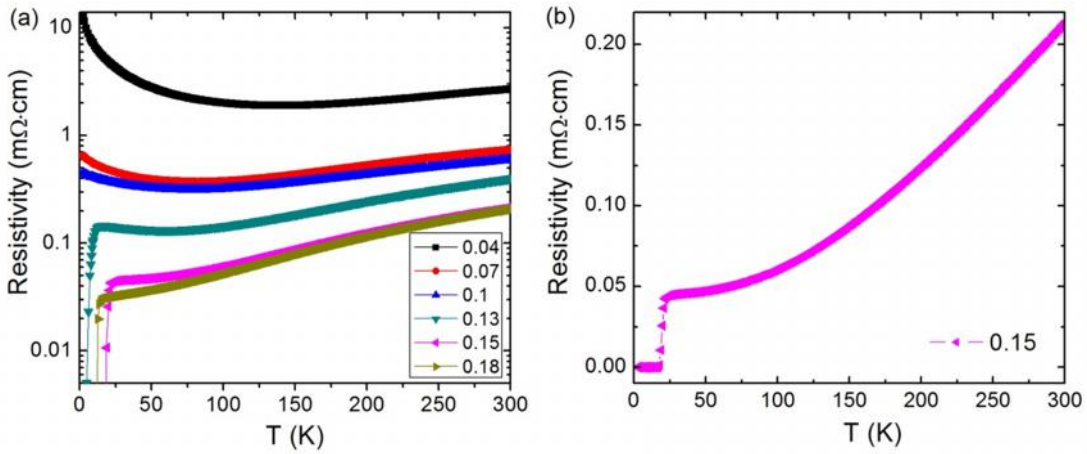

Figure 4.2 (a) Logarithmic-scale resistivity as a function of temperature for $Pr_{2-x}Ce_xCuO_4$ with different Ce doping level x. (b) Linear-scale resistivity-temperature curve for $Pr_{2-x}Ce_xCuO_4$ with optimal Ce doping level x=0.15.

Figure 4.3 shows a comparison of critical temperature T_c for PCCO thin films grown on STO substrates between our results and previous report [165]. The T_c in our results is obtained from the resistivity-temperature curves in Figure 4.2(a) and is defined as the temperature at mid-point of superconducting transition. It can be seen that our data points match the phase diagram of previous results, suggesting the high quality of our thin films.

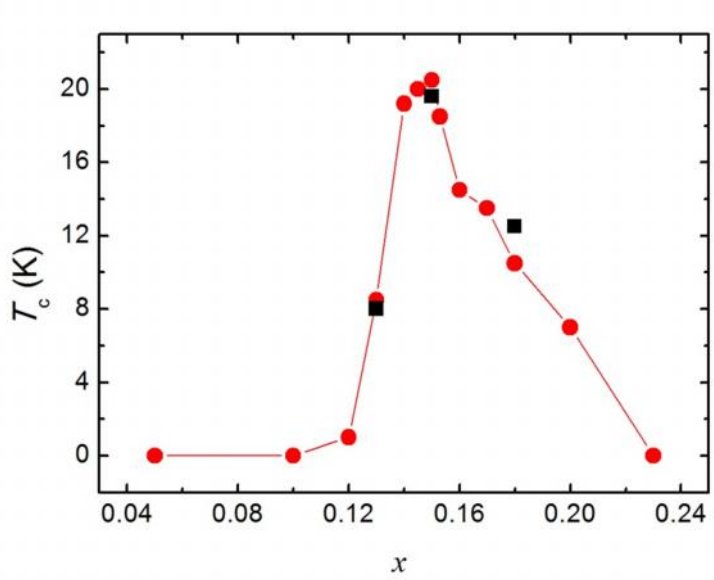

Figure 4.3 Critical temperature T_c for $Pr_{2-x}Ce_xCuO_4$ as a function of Ce doping level x. The red-circle data is extracted from ref.[165] and the black square is our data.

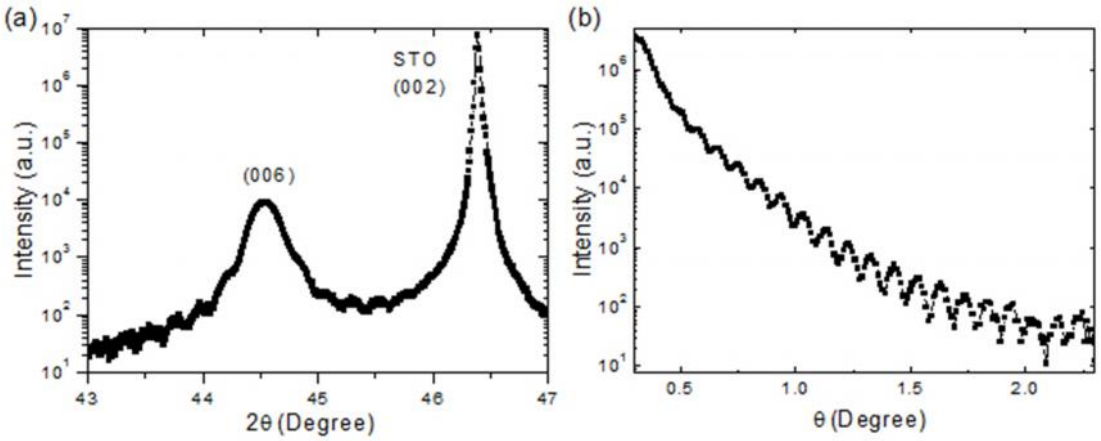

Figure 4.4. X-ray data for the $Pr_{1.9}Ce_{0.1}CuO_4$ film. The wavelength of X-ray is λ=1.538 Å. (a) Finite-thickness oscillations in the vicinity of the (006) diffraction peak (2θ/ω coupled scan). (b) Finite-thickness oscillations in low-angle X-ray reflectivity (XRR).

The high quality of thin films has also been confirmed by high-resolution X-ray diffractometry (HR-XRD) and low-angle X-ray reflectivity (XRR). Figure 4.4 shows the X-ray data of a ~45-nm $Pr_{1.9}Ce_{0.1}CuO_4$ film grown on STO substrate. These measurements were done by HR-XRD and XRR in the X-ray Demonstration and Development (XDD) beamline

at Singapore Synchrotron Light Source (SSLS). The X-ray wavelength is λ=1.538 Å. The finite-thickness oscillations and low-angle reflectance oscillations indicate high quality of the films.

For the preparation of EDLT devices, ultrathin films are required. The ultrathin layering structure with nominally 1 unit cell (uc) underdoped $Pr_{1.9}Ce_{0.1}CuO_4$ on 4-uc Pr_2CuO_4 (PCO) were grown on TiO_2-terminated STO (001) substrates. The PCO layer is a buffer layer, facilitating the growth of the subsequent PCCO layer. We found that without PCO buffer layer, 1-uc PCCO directly grown on STO shows resistance much higher than that grown on PCO layer, suggesting degradation of crystal quality. Since PCO is undoped, resistance of ultrathin PCO layer shows highly insulating behaviour, out of measurement limit at low temperature, as is confirmed by the transport measurement. Therefore, this buffer layer is not expected to play a significant role in the transport properties of the EDLT device.

The substrates were patterned before the deposition of PCCO films, which will be shown in the following section. The thin films were deposited at 790 ^{o}C under P_{O2}= 0.25 mbar and then cooled down to room temperature from 720 ^{o}C in vacuum at the rate of 20 ^{o}C/min. The oxygen composition has a significant influence on the electrical properties of PCCO. Heavy reduction of oxygen causes degradation of PCCO quality and the resultant lower T_c and higher resistivity [166]. For the thick PCCO films, direct cooling from 790 ^{o}C in vacuum after deposition is necessary to obtain low resistivity and superconductivity, as is shown above. However, we found that for the ultrathin films, direct cooling from 790 ^{o}C in vacuum cause high resistivity. This may be due to high oxygen vacancies since it is easier to remove oxygen in ultrathin films, compared to thick films. Therefore, after deposition, the ultrathin films were cooled down from 790 ^{o}C to 720 ^{o}C at P_{O2}= 0.25 mbar, and then from 720 ^{o}C to room temperature in vacuum. The thickness of ultrathin films was calibrated by measuring the thickness of thick films using Profiler, low-angle XRR and transmission electron microscopy, and the number of laser shots during the growth. Figure 4.5 shows atomic force microscopy (AFM) image (5 μm × 5 μm) of ultrathin PCCO/PCO heterostructures grown on STO

substrate. The root-mean-square (RMS) roughness is less than 0.44 nm, indicating smooth surface of thin films. Thin films with smooth surface are important for cuprate EDLT devices, since only a few top layers are active when electric field is applied.

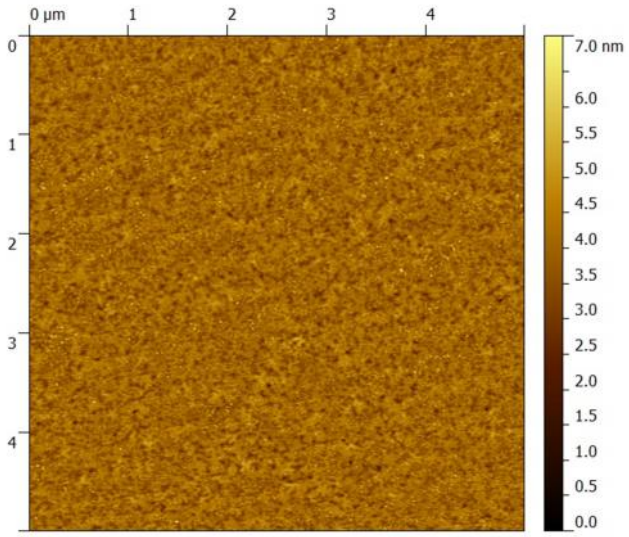

Figure 4.5. Atomic force microscopy (AFM) image of the surface of ultrathin PCCO/PCO heterostructures. Smooth surface and high crystal quality of thin films is observed with root-mean-square (RMS) roughness of less than 0.44 nm and without granularity and secondary-phase precipitates.

4.2.3 Device preparation

The detailed schematic overview of the device development is shown in Figure 4.6. This includes three primary steps. Firstly, STO substrates were patterned before the deposition of PCCO films (Figure 4.6(a)-(e)). TiO_2-terminated STO was patterned into typical Hall bar geometry using conventional photolithography and depositing amorphous AlN (a-AlN) films as hard masks. The thickness of the a-AlN is higher than 100 nm, so that the pattern can be visible in optical microscopy, which is necessary for the mask alignment during second-time lithography process. After patterning, the substrate surfaces are still clean and atomically flat with single termination, as confirmed by AFM. In order to remove the oxygen vacancies introduced in STO during deposition of a-AlN, the patterned STO were annealed in a furnace at 500 ^{o}C in air for 2 hour. Secondly, the patterned substrates were put into PLD chamber for

the deposition of PCCO/PCO thin films (Figure 4.6(f)). It should be noted that the PCCO/PCO films grown on amorphous AlN are highly insulating. This causes the leakage current to be negligibly small, as will be shown in the following text. Finally, after film deposition, Cr/Au (10/70 nm) layers for current/voltage probes and gate electrodes were deposited by thermal evaporation methods (Figure 4.6(g)-(j)). Figure 4.6(k) shows schematic diagram of the operation of a fabricated device. A top view photograph of a device is shown in Figure 4.6(l). The width of the Hall bar is 50 μm and length is 500 μm. The distance between two voltage probes is 160 μm. A six-probe configuration of the Hall-bar device allows for the measurement of both longitudinal and Hall resistance. A large planar gate electrode is used to accumulate ions.

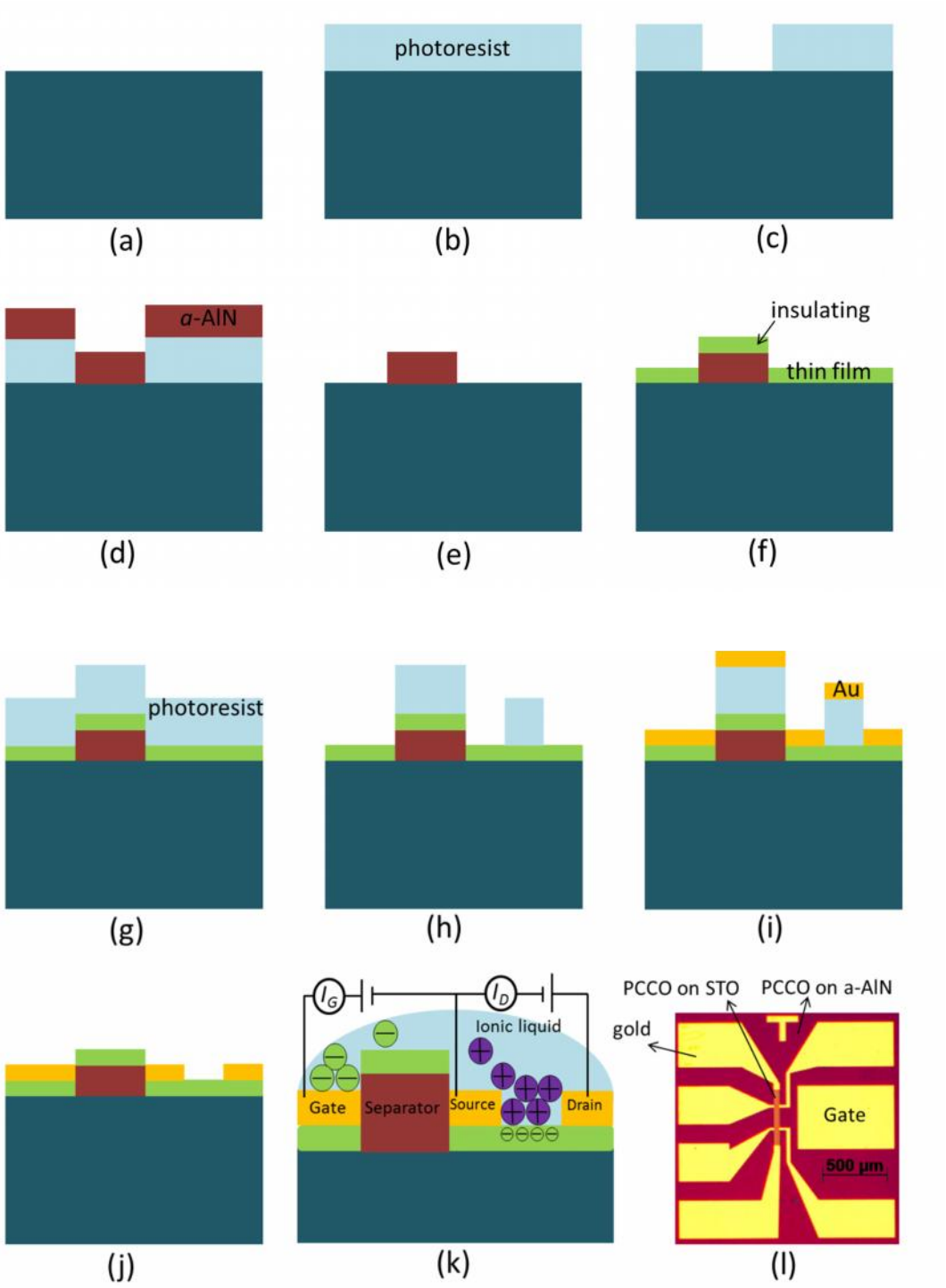

Figure 4.6. Schematic overview of the device preparation of (a) single terminated STO substrate, (b) photoresist applied on bare substrate by spin coating, (c) photoresist exposed to UV light and developed, (d) deposition of *a*-AlN by PLD at room temperature, (e) lift off and removal of photoresist and AlN on top, (f) deposition of PCCO thin film by PLD, the film on *a*-AlN is insulator, (g) second-time photolithography, photoresist applied, (h) photoresist exposed to UV light and developed, (i) deposition of gold by thermal evaporation, (j) lift off and removal of photoresist and gold on top, (k) schematic diagram of the operation of a fabricated EDLT device, and (l) microscopic top view of a fabricated device.

4.2.4 Transport measurements

The transport measurements were made using a Quantum Design Physical Property Measurement System (PPMS) and Keithley Sourcemeters (Model 6430) for applying the gate voltages. A small droplet of an ionic liquid was put onto the sample and covered both the conducting channel and the gate electrode. Then, a thin glass plate was put on top of the liquid droplet, as is shown in Figure 4.7. The samples were quickly cooled down to 210 K after covering IL to prevent possible chemical reaction between thin films and IL at room temperature [23, 24]. When a gate voltage (V_G) was applied, the ions freely move between conducting channel and gate electrode so that they can accumulate on and dissipate away from the film surface, enabling electrostatic charging in a thin layer near surface of film. The V_G was applied at 210 K and kept for several tens of minutes for charging. Resistance measurement was made as the samples were cooled down while keeping the V_G constant. In order to change V_G, the sample was heated to 210 K after each resistance-temperature curve measurement and a new V_G was applied.

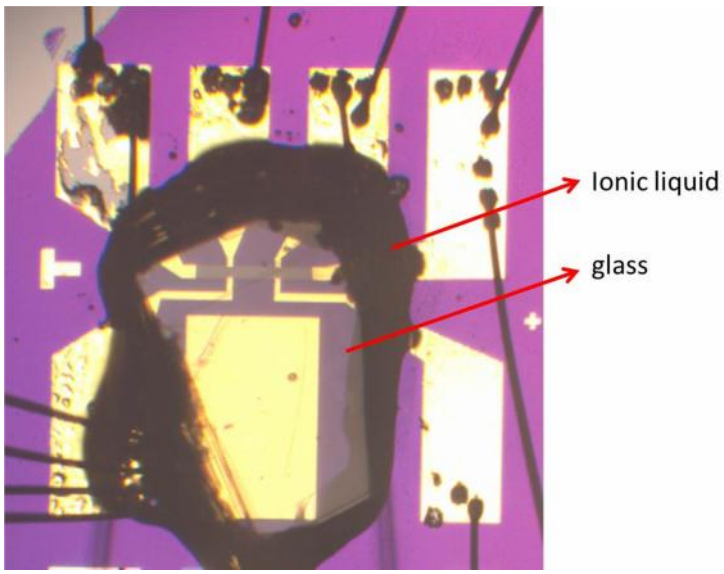

Figure 4.7. A small droplet of an ionic liquid was put onto the sample and covered both the conducting channel and the gate electrode. Then, a thin glass plate was put on top of the liquid droplet.

The typical relationship between resistance and time after applying a V_G is shown in Figure 4.8. For low V_G at which the sample shows high resistance, resistance decreases sharply within 10 min when the V_G is applied, and then decreases slowly and tends to saturate after ~10 min (Figure 4.8(a)). At this V_G, the charging time is kept for around 40 min. Although 40 min is not enough to obtain the complete saturation of resistance, it is sufficient to establish a new charging state. For high V_G at which the sample shows low resistance, resistance decreases smoothly and does not tend to saturate even after 25 min (Figure 4.8(b)). These suggest that the decrease rate of resistance as a function of time depends on the conducting states of the Hall bar channel. In order to obtain quasi-continuous charging states, for high V_G, at each V_G, the sample was kept for 25-40 min for charging and then cooled down for resistance measurement without the saturation of the resistance. The keeping time depends on the change of resistance after applying a V_G. This is highly necessary for the doping range near insulator-to-superconductor transition, since at this doping range a small change of resistance (correspond to carrier density) at 210 K will cause a large change of T_c, as is shown in Figure 4.10. The effective control of V_G and charging time is critical to quasi-continuously tune the carrier density in PCCO film, which is necessary for quantitative analysis of the SIT.

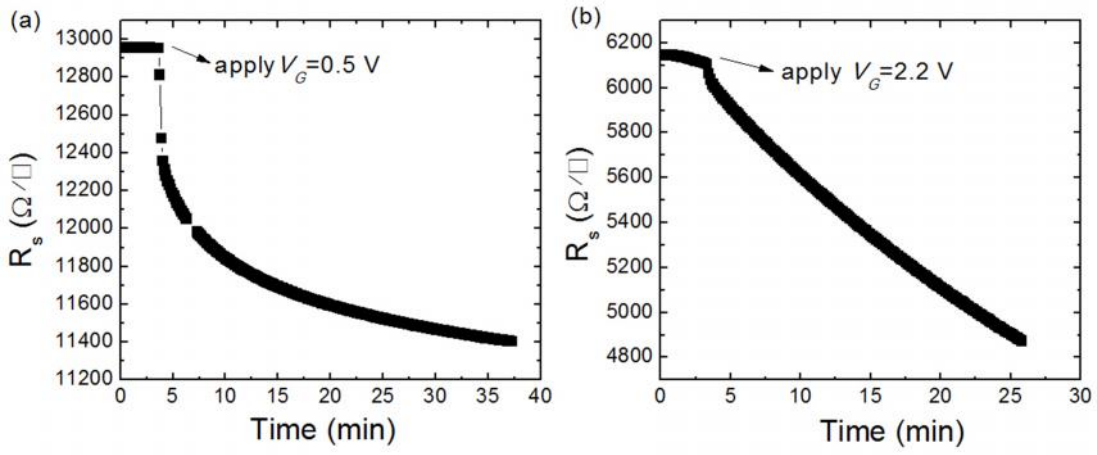

Figure 4.8. Resistance as a function of time after applying a gate voltage. (a)V_G=0.5 V (b) V_G=2.2 V

The leakage current (I_G) is one of the most important parameters in characterizing the performance of electric field-effect devices. Figure 4.9 shows the I_G as a function of V_G for a PCCO-EDLT device. This measurement was done at 210 K. It can be seen that I_G is of the order of 1 nA when the V_G is limited to 3.2 V. This negligibly small I_G indicates good operation of device.

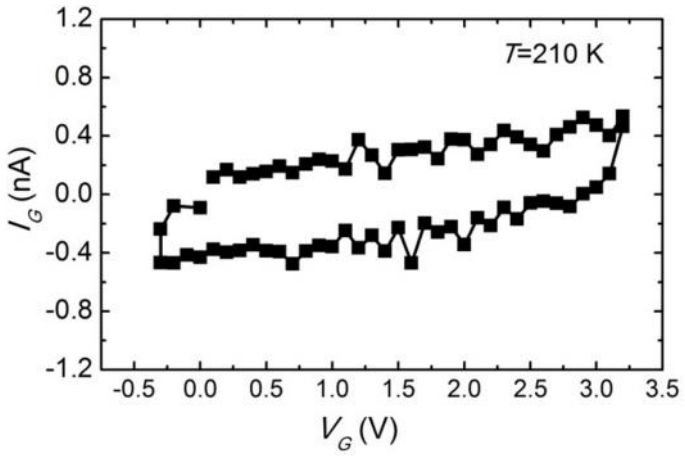

Figure 4.9. Gate voltage (V_G) dependence of the leakage current (I_G).

4.3 Results of electrical transport measurement

4.3.1 Superconductor-insulator transition in an underdoped thin film

Figure 4.10(a) and (b) show the sheet resistance vs temperature (R_s-T) curves at various V_G for a device with 1uc-$Pr_{1.9}Ce_{0.1}CuO$/4uc-PCO. Many curves were recorded and a quasi-continuous insulator-to-superconductor transition was observed. The initially underdoped sample shows insulating behaviour. As V_G is increased, the accumulation of electrons on the surface is enhanced and the normal-state R_s decreases. At V_G above 2.59 V, the resistance drops sharply at low temperature, signaling the onset of superconductivity. As V_G is increased, the T_c increases up to a maximum of 14.8 K at V_G=3 V and decreases beyond this voltage. The T_c is taken to be the temperature at which the R_s falls to 90% of its normal-state value. Figure 4.10(c) shows the magnetic field (B)-dependent R-T curves at V_G=3 V. As B increases,

T_c decreases and finally the zero-resistance state is completely suppressed at B=6 T. This further confirms the occurrence of superconductivity in PCCO as a result of electric field-effect doping. Due to the short Thomas-Fermi screening length in cuprates [23, 164], the active layer in the EDLT device is limited to one or two CuO_2 planes, leaving the deeper layers unaffected. To further demonstrate this screening effect, devices with optimally doped $Pr_{1.85}Ce_{0.15}CuO_4$ showing superconducting T_c of around 15 K were fabricated and tested. It was found that even at a higher V_G of 4 V, only a small change of T_c but no insulating phase was obtained in a film with thickness above 3 uc, indicating the shunting effect from the deeper layers which are not influenced by the field effect. These suggest that the superconductivity obtained in the underdoped EDLT devices occurs within one or two CuO_2 layers on the surface, and thus, is two-dimensional.

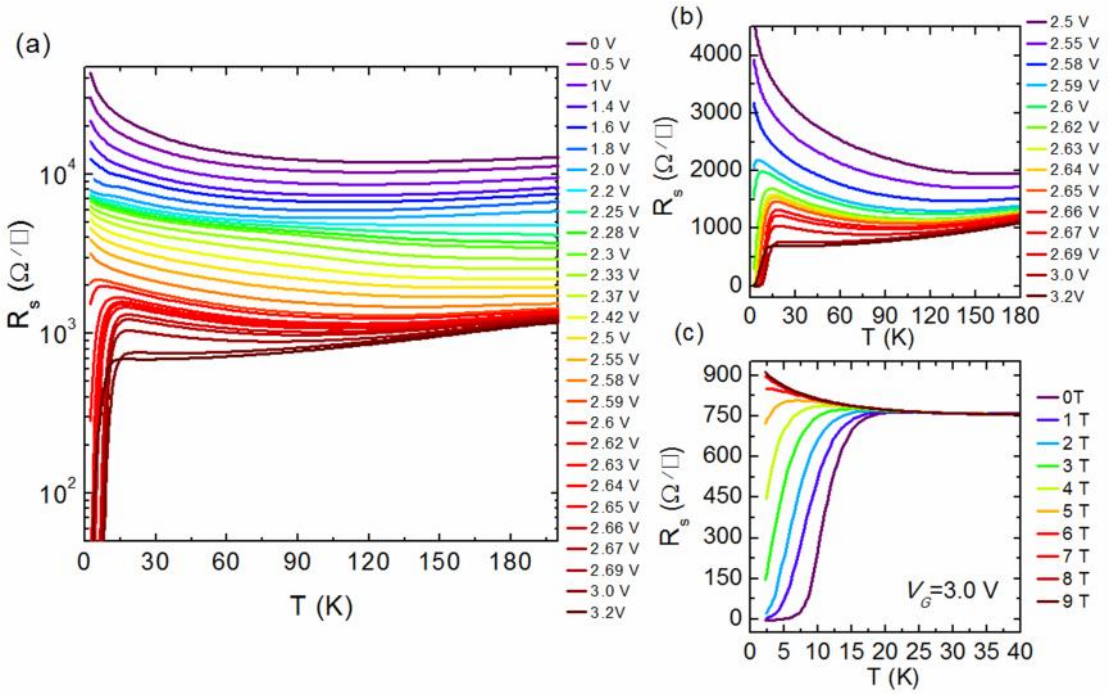

Figure 4.10. (a) The logarithmic-scale sheet resistance vs temperature (*R-T*) curves at various gate voltages for the PCCO sample. (b) The linear-scale *R-T* curves at the superconducting region and insulating region near the SIT. (c) The *R-T* curves at V_G=3.0 V for various magnetic field applied perpendicular to the CuO_2 plane.

It can be seen from the R_s-T curves that T_c increases, and normal-state resistance decreases as the V_G is increased up to 3.0 V (Figure 4.10(b) and Figure 4.11). However, at higher V_G of 3.2

V, normal-state resistance keeps decreasing but T_c decreases. Moreover, in the normal state, the temperature dependence of R_s shows the evolution from a metallic to insulating behaviour with a minimum resistance temperature (T_{min}) and T_{min} keeps decreasing as the V_G increases up to 3.2 V, which is similar to chemically doped materials as the doping is increased [140, 144]. These indicate that the sample is optimally doped at V_G=3.0 V and lightly overdoped at V_G=3.2 V. Therefore, the PCCO thin film can be tuned from underdoped phase to slightly overdoped phase by IL-assisted field effect doping. It is expected that higher V_G will cause higher carrier density, and thus, the highly overdoped states can be obtained if V_G is further increased. However, at V_G higher than 3.2 V, unlike the ones shown in Figure 4.8, the resistance does not decrease but keep increasing when a V_G is applied. As is shown in Figure 4.11, at V_G=3.5 V, the T_c shows lower values but normal-state resistance shows higher value, compared to the slightly overdoped state at V_G=3.2 V. At higher V_G of 3.9 V, superconductivity even disappears and there is a resistance upturn at low T probably caused by localization. These behaviours are different than those in highly overdoped region, in which the metallic behaviour persists down to the lowest T measured. These may suggest that the device deteriorate at V_G higher than 3.2 V. Therefore, in the following text, we use the transport data at V_G≤3.2 V for analysis.

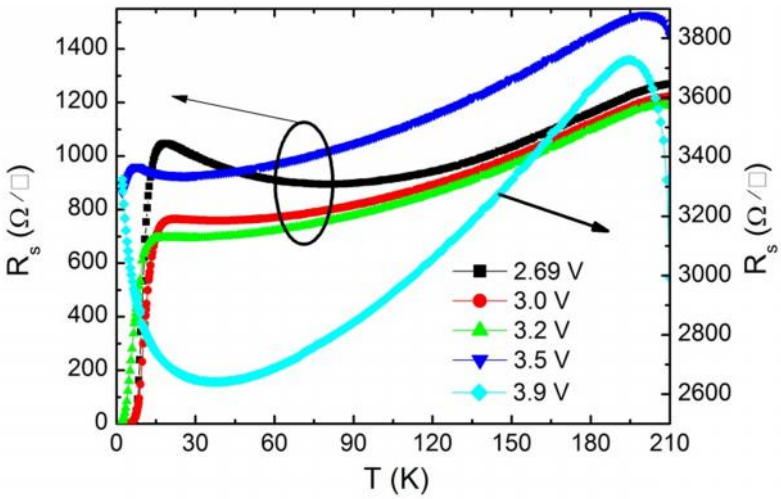

Figure 4.11. *R*-*T* curves at higher V_G of 2.69~3.9 V for the PCCO sample.

It has been reported that liquid gating could induce oxygen vacancies in some of the oxides, and thereby change the electrical transport properties [22]. To demonstrate whether there are oxygen vacancies induced in PCCO, we measured the R_s-T curves of a device before and after gating experiments, as is shown in Figure 4.12(a). The R_s-T curve before gating was obtained on the device in pristine condition before any IL was applied. The one after gating was obtained after the device was gated from insulator to superconductor by applying V_G from 0 up to 3.2 V (Figure 4.12(b)), with subsequent removal of the IL. One can see that these two curves show reasonable agreement, indicating the reversibility of EDLT operation. This suggests that the chemical compositions of PCCO film are unchanged before and after gating experiments. Furthermore, the top layer in our EDLT device is underdoped $Pr_{1.9}Ce_{0.1}CuO_4$, which is not superconducting even if the oxygen is further reduced [165]. However, superconductivity in $Pr_{1.9}Ce_{0.1}CuO_4$ is obtained by liquid gating. These indicate that in this study, the IL predominantly induces charge carriers at the surface of PCCO as opposed to inducing oxygen vacancies.

Figure 4.12(b) shows the R_s-T curves at various V_G. Note that this is another device which is different from the one shown in Figure 4.10. It can be seen that the device could also be induced from insulating to superconducting phase and the SIT occurs at a critical sheet resistance lower than the pair quantum resistance, R_Q (see also in Figure 4.10(b)). This means that liquid-gated SIT on PCCO is reproducible.

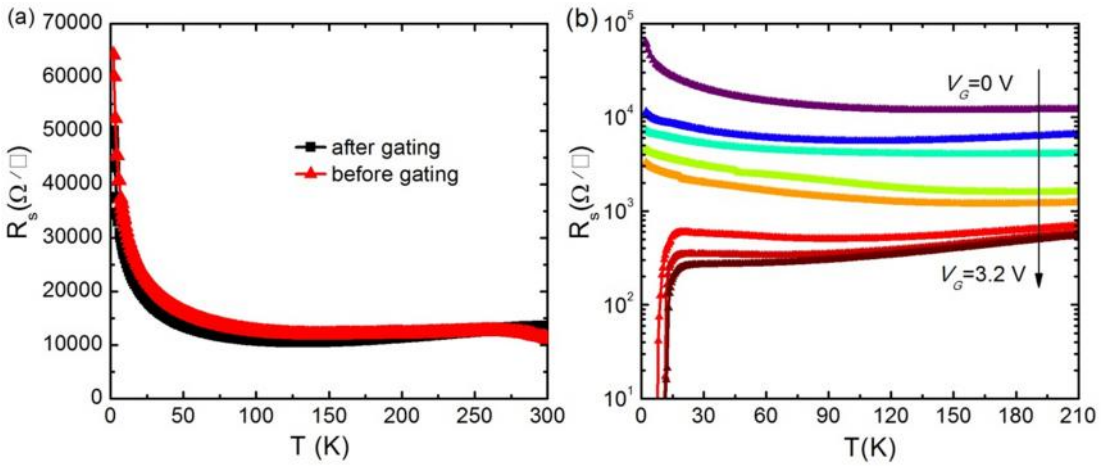

Figure 4.12. (a) R_s-T curves for an EDLT device before and after gating experiments. Inset: (b) R_s-T curves at various V_G.

4.3.2 Phase diagram

The phase diagram, T_c versus field-effect induced carrier concentration, was constructed based on the measured R_s-T curves at different V_G. To characterize the field effect-induced carrier concentration, n, we define the term n as electrons per formula unit and identify n with x, the Ce doping level in $Pr_{2-x}Ce_xCuO_4$. Therefore, the optimally doped sample $Pr_{1.85}Ce_{0.15}CuO_4$ has a carrier concentration x=0.15 (equal to the Ce doping level) electrons per formula unit. In order to estimate x at every V_G, we make assumptions that $1/R_s$(180K) is proportional to the x [23, 24]. From the discussion above, we can assume that the sample at V_G=3.0 V is optimally doped, and thus, the carrier concentration is x=0.15. The x at other V_G can be estimated by x=0.15×R_s(x=0.15, 180K)/R_s(x, 180K). Here, we choose the R_s at 180 K since at this T the IL is frozen and a new charging state has already been established [23, 24, 167]. The dependence of the estimated x on the measured R_s(180 K) is shown in Figure 4.13. One can see that the modulation of x from 0.0135 to 0.153 is obtained by IL-assisted field-effect doping.

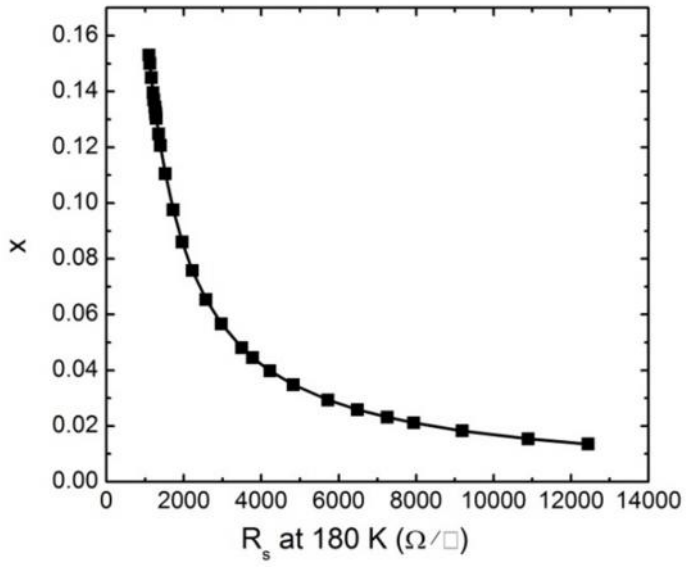

Figure 4.13. The induced carrier concentration, x, as a function of the measured sheet resistance, R_s, at 180 K.

Figure 4.14(a) shows the phase diagram of T_c versus estimated x. It can be seen that insulator-to-superconductor transition occurs at a critical x of around 0.12 and T_c increases sharply with increasing x peaking at x=0.15. The phase diagram from chemical doping [165] is also plotted and the highest T_c at x=0.15 is normalized to the one from field-effect doping. One can see that the phase diagrams derived from field effect and chemical doping are remarkably similar. This suggests that the estimation of x is reliable, a necessity for quantitative analysis near the SIT. Figure 4.14(b) shows color plot of all the R-T curves with the change of x from 0.0135 (underdoped) to 0.1531 (slightly overdoped). It can be seen that R_s changes quasi-continuously with T and x, dropping sharply at the superconducting regime.

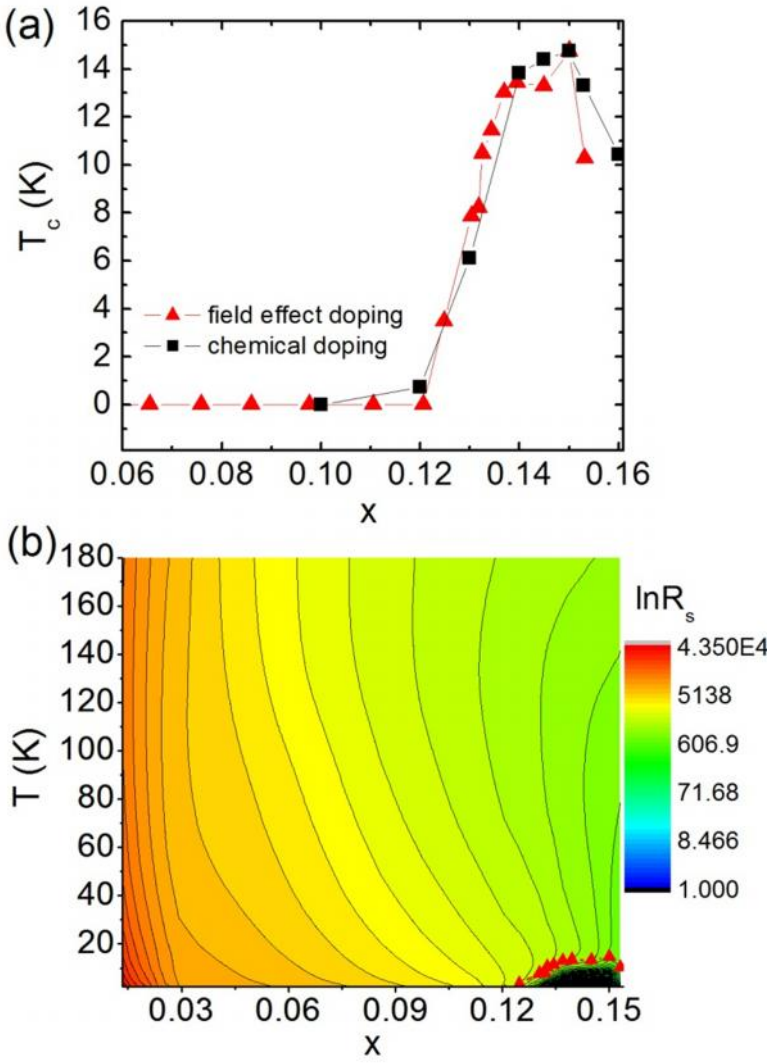

Figure 4.14. (a) Critical temperature T_c as a function of carrier concentration x for electric field effect and chemical doping. T_c~x for chemical doping is extracted from ref.[165] and the highest T_c at x=0.15 is normalized to the one from field effect doping. (b) The color plot of the R-T and x. Different colors represent different sheet resistances. The red triangle is T_c.

4.3.3 Hall effects

Figure 4.15 shows transverse Hall resistances (R_{xy}) as a function of B for different V_G. R_{xy} shows a negative slope, indicating that the field effect-induced charge carriers are electrons as expected. The dependence of R_{xy} on B is reasonably linear, a necessity for the determination of Hall coefficients (R_H). Figure 4.16(a) shows the normalized Hall number (n_H) as a function of V_G. The Hall number is calculated from n_H= -1/($R_H e$), where e is elementary charge and R_H is the Hall coefficient determined from the slope of the linear fit of the R_{xy}-B curve in Figure

4.15. It can be seen that n_H increases with increasing V_G, indicating that more charge carriers were induced at higher V_G. This further indicates that IL-assisted field effect predominantly induces charge carriers at the surface of PCCO. In Figure 4.16(b), n_H as a function of electron concentration x is shown. One can see that there is an anomaly in n_H as x is increased through x~0.13. n_H increases moderately at $0.0135<x<0.13$, and sharply at $0.13<x<0.15$. For such transport anomaly, it has been shown that in liquid-gated YBCO, n_H shows a peak at x~0.15 as x increases from 0.09 (underdoped) to 0.195 (overdoped) [25]. This anomaly in n_H of YBCO coupled with the observation that the normal resistance increase with x on the overdoped side suggests that there is an electronic phase transition in the Fermi surface around the optimal doping level [25]. In the case of PCCO, the overdoped state could not be obtained in the present results. Further optimization on the field-effect technique to obtain overdoped phase is necessary to study such electronic phase transition in PCCO. However, the difference between YBCO and PCCO can be seen if we just compare n_H from underdoped to the optimally doped levels. In liquid-gated YBCO, n_H increases moderately with increasing x from 0.09 to 0.15 without any anomaly. In PCCO, an anomaly of n_H is observed at x=013. This suggests the asymmetry in the normal-state transport properties between YBCO and PCCO below optimal doping levels.

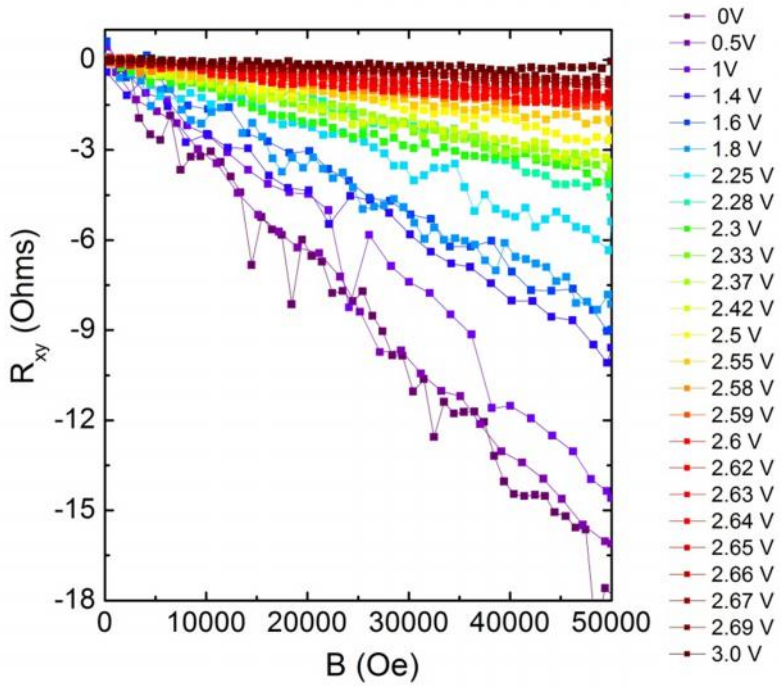

Figure 4.15. Hall resistance (R_{xy}) as a function of magnetic field at T=150 K for different gate voltages.

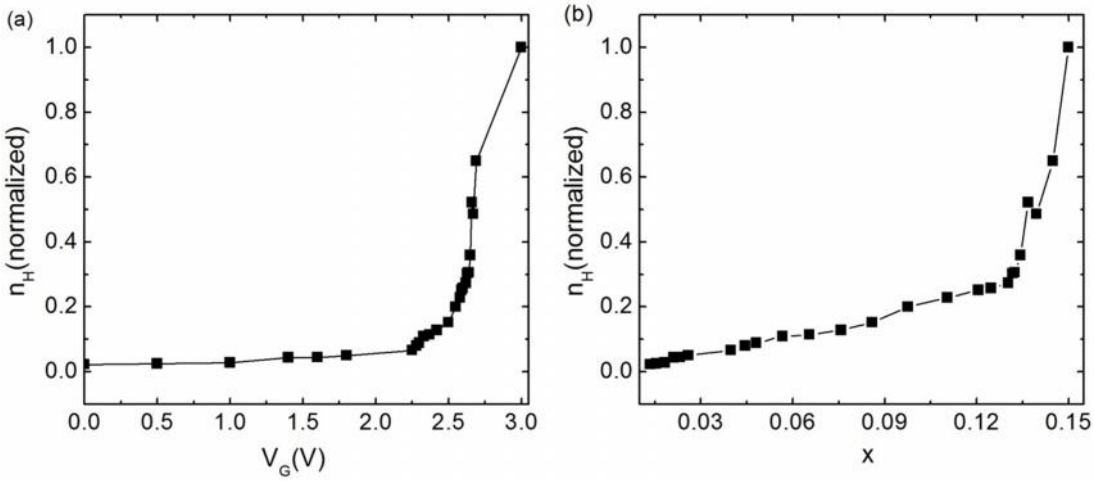

Figure 4.16. (a) Normalized Hal number (n_H) as a function of gate voltage. (b) n_H as a function of carrier concentration.

4.3.4 Quantum phase transition

It is proposed that SIT at the limit of zero temperature and two dimensions is an example of a QPT [64-66]. At nonzero temperature, the signature of a QPT is a success of finite size

scaling in describing the finite-temperature data [23, 24, 67-69]. The R_s of a 2D system near a quantum critical point collapses onto a single scaling function, $R_s(x_t,T)=R_cF(|x_t - x_c|T^{-1/vz})$, where T is temperature, x_t is tuning parameter (in the present result, x_t is carrier concentration and magnetic field), x_c is x_t at critical point, R_c is critical R_s at $x_t = x_c$, v is the correlation length critical exponent, z is the dynamic critical exponent, and $F(u)$ is a universal function of u with $F(u)\rightarrow 1$ when $u\rightarrow 0$. The low-temperature resistances near SIT were extracted for quantitative analysis. In Figure 4.17, the resistance isotherms from 2.2 to 6 K as a function of x are plotted. All curves cross at a single point which separates the insulating and superconducting regimes. The R_c is about 2.35 kΩ, which is much lower than the pair quantum resistance given by $R_Q=h/(2e)^2$=6.45 kΩ. The critical x is x_c=0.118, comparable to that derived from the chemical doping [165]. Inset of Figure 4.17 is the finite size scaling analysis of the data in the vicinity of SIT. Given the exponent product vz=2.5, all of the isotherm curves collapse onto a single function, suggesting the occurrence of a 2D-QPT. The value of vz for PCCO is different from those for the hole-doped 214-structure counterpart, vz=1.5 for LSCO [23] and vz=1.2 for $La_2CuO_{4+\delta}$ [26]. It is consistent with that of the quantum percolation model ($vz\approx 7/3$) [24, 79, 168, 169]. It has been suggested that QPTs occur inside the superconducting dome in both electron-doped PCCO and hole-doped LSCO and $Bi_2Sr_{2-x}La_xCuO_{6+\delta}$ [61-63]. These QPTs are evidenced by the observation that a Hall coefficient anomaly [61, 63] and a thermopower anomaly [62] appear near optimum doping level at temperature below the zero-field T_c. However, the QPT here occurs at the underdoping level where the SIT occurs. This could be an important observation for fully understanding the quantum criticality in cuprates.

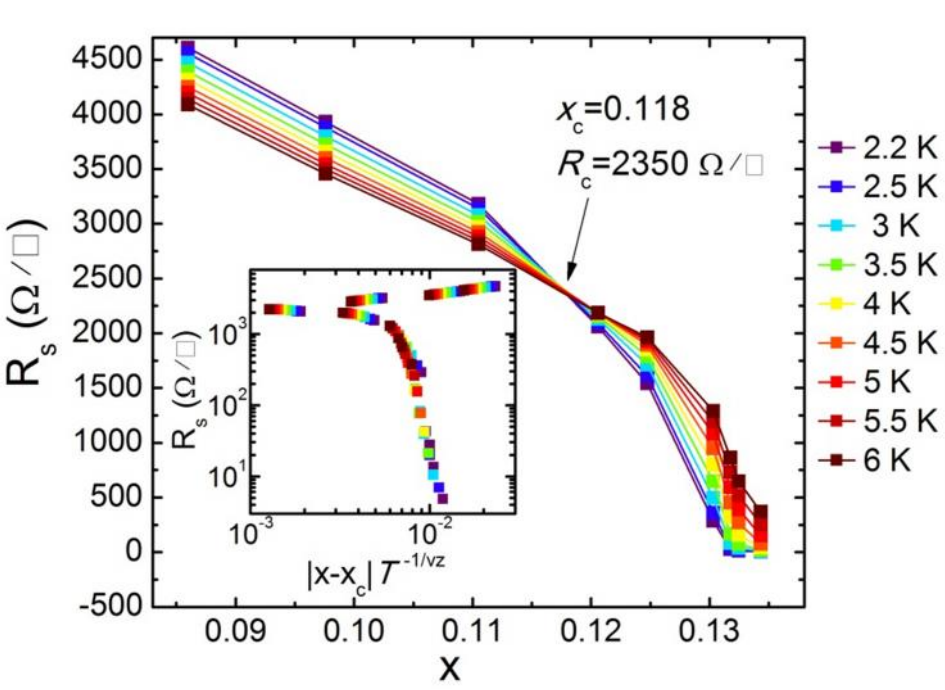

Figure 4.17. Isotherms of sheet resistance as a function of carrier concentration at T ranging from 2.2 to 6 K. Inset: Finite size scaling analysis of the same data.

4.3.5 Magnetic field-induced superconductor-insulator transitions in superconducting EDLTs

It can be seen in Figure 4.10 that at V_G above 2.59 V, the sample was gated into superconductor at low T. We chose three different superconducting states and studied magnetic field (B)-tuned SITs, at V_G of 2.75, 3.0 and 3.2 V, which correspond to underdoped, optimally doped and overdoped states (x=0.132, 0.15 and 0.153), respectively. Figure 4.18(a) shows the R_s-T curves without applying magnetic field. It can be seen that three superconducting states have different normal-state sheet resistance (R_n) and T_c. The R_n obtained at onset of superconductivity and at zero magnetic field, are 1957, 764 and 694 Ω/□ for V_G=2.75, 3.0 and 3.2 V, respectively. Figure 4.18(b)-(d) show the R_s-T curves at various magnetic fields for different V_G. The applied magnetic field is perpendicular to the CuO_2 plane. It can be seen that at each V_G the sample was initially superconducting and could be tuned to insulating states.

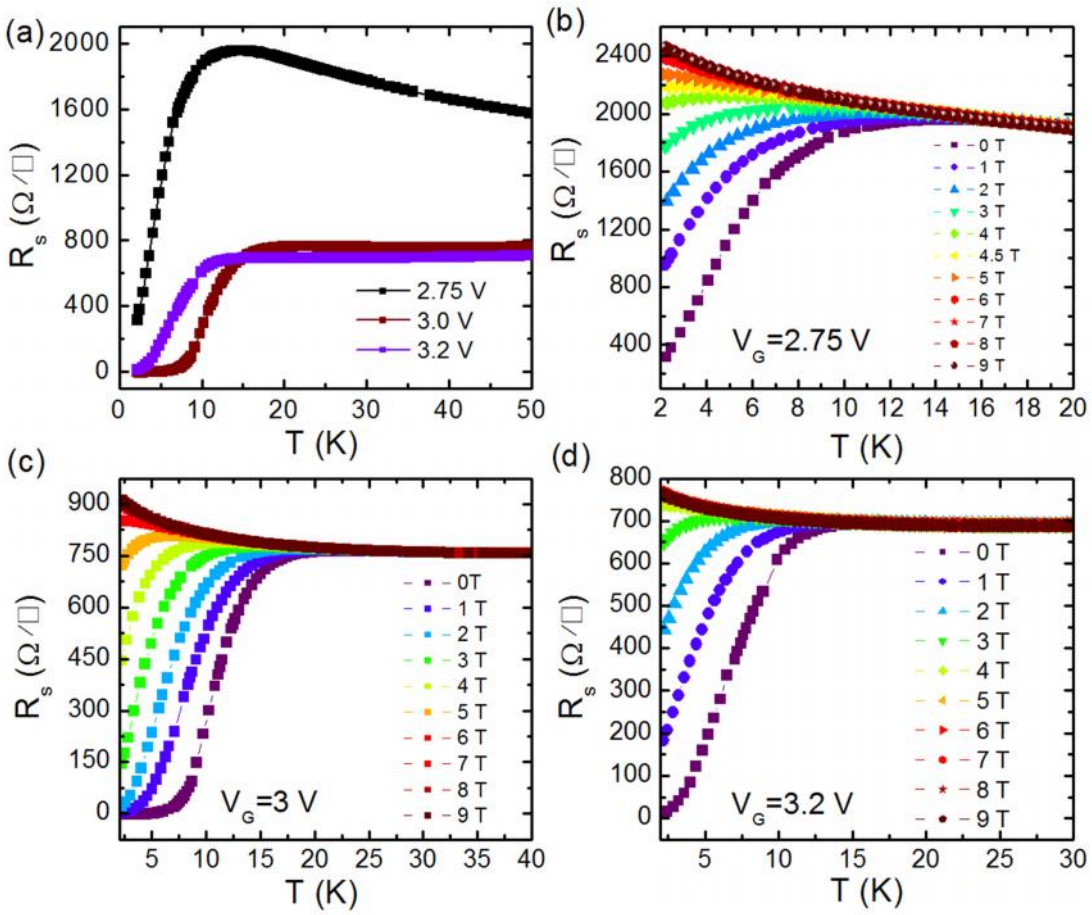

Figure 4.18. (a) *R-T* curves at V_G=2.75, 3.0 and 3.2 V, corresponding to the underdoped, optimally doped and overdoped states, respectively. After the measurement of the overdoped curve at V_G=3.2 V, the V_G was reduced to lower value of 2.75 V to obtain the underdoped state, and then measure *R-T* curve. (b), (c), (d) are the *R-T* curves at various magnetic field for different V_G. The applied magnetic field is perpendicular to the CuO_2 plane.

Figure 4.19(a)-(c) show magnetoresistances (MRs) at four temperature points below the onset of superconductivity. At each doping level, isotherms of R_s cross each other at a single point which separates the insulating from superconducting phase. The critical magnetic fields, B_c and R_c as a function of x are shown in Figure 4.19(d). It can be seen that B_c peaks at optimally doped state and shows lower values at underdoped and overdoped states, consistent with H_{c2} in chemically doped materials [51]. R_c is not universal, decreases with increasing doping levels. The values of R_c are much lower than R_Q, especially for the ones at optimally doped and overdoped states. The insets of Figure 4.19(a)-(c) show finite size scaling analysis of resistance isotherm curves. One can see that all the curves collapse onto a single function

except at high magnetic field, suggesting the occurrence of 2D-QPTs. The deviation of scaling at high magnetic field could probably be due to the presence of weak localization dominating at high field, which causes a weak increase in resistance with increasing magnetic field [170]. This can be seen in the MR curves, which show that above B_c, the resistance tends to saturate at high field. Interestingly, the same exponent product vz=1.4 is obtained at three different V_G, suggesting that the SITs are governed by the same mechanism. The vz observed here is consistent with classical percolation theory (vz≈4/3) [67, 83, 169].

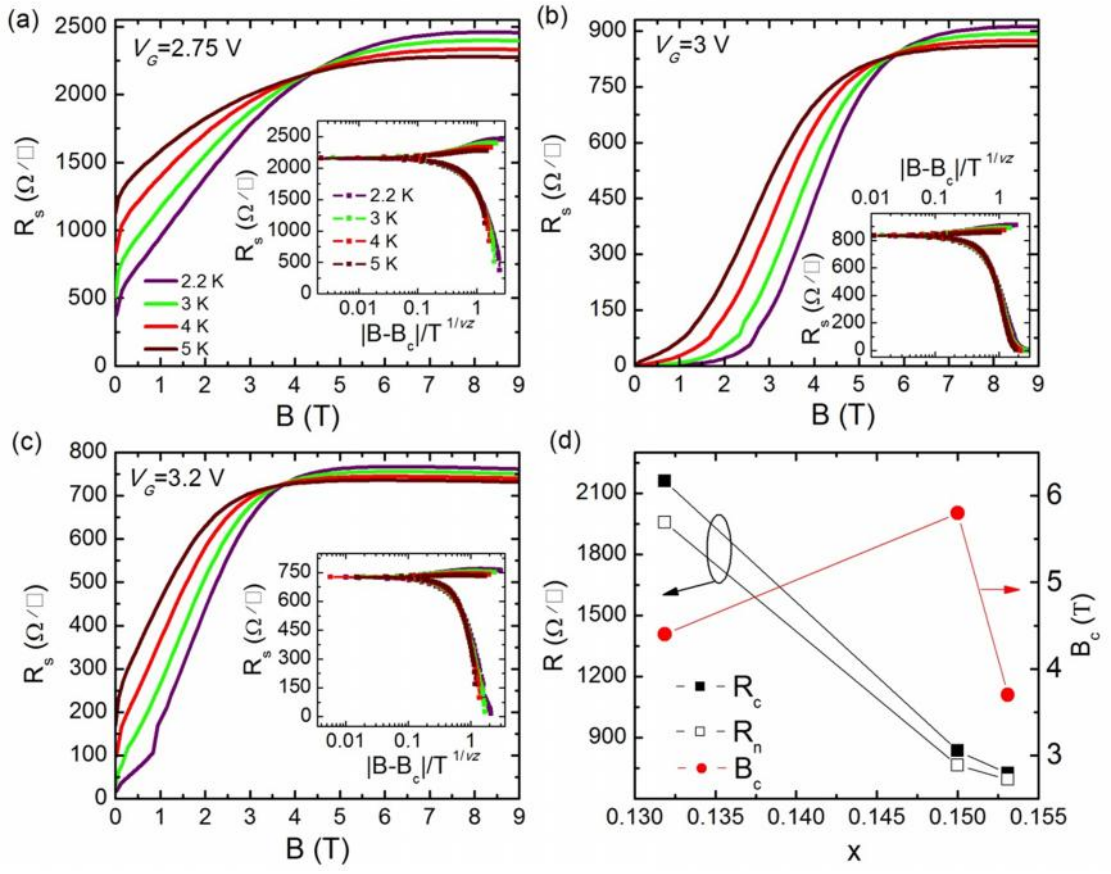

Figure 4.19. Magnetoresistances at (a) V_G=2.75 V, (b) V_G=3.0 V, (c) V_G=3.2 V, corresponding to underdoped, optimally doped and overdoped states (x=0.132, 0.15 and 0.153), respectively. The measurements were done at four different T points which are lower than the T_c. Insets show the R_s as a function of $|B-B_c|/T^{1/vz}$. The data can be fitted by finite size scaling function assuming vz=1.4 for three doping levels. (d) Critical sheet resistance, R_c, normal-state sheet resistance, R_n, and critical magnetic field, B_c, as a function of carrier concentrations which are corresponding to different V_G. R_c and B_c are the resistances and magnetic fields at the points where the resistance isotherms cross each other. R_n is the resistance obtained at onset of superconductivity and zero B.

It has been suggested above that the SITs induced by both carrier density and magnetic are governed by percolation effects, which means that the transport is caused by charge tunnelling between two conducting regions across a non-conducting region. The percolation effects in SITs have also been seen in InO_x [79] MoGe [67, 83] and recently YBCO [24]. Interestingly, under different tuning parameters, carrier concentration and magnetic field, the percolations show different behaviours in the same sample, quantum mechanical in carrier-tuned SIT and classical in *B*-tuned SIT. This may be due to the difference between the percolation correlation length and the system length scale at different parameters [169]. Further investigation of the crossover between these two effects by measuring the carrier-tuned SITs under various magnetic fields may help to reveal the underlying mechanism.

4.3.6 Fermionic excitations

As is discussed in the introduction section, there are two scenarios, bosonic and fermionic, to explain the 2D superconductor-insulator QPT. In the bosonic scenario, Cooper pairs are preserved on both superconducting and insulating sides, and R_c is equal to R_Q=6.45 kΩ. In the fermionic scenario, Cooper pairs present on the superconducting sides, while they are broken and the fermionic excitations dominate on the insulating side. The value of R_c observed in YBCO and LSCO suggests that the SITs is driven by quantum phase fluctuations in the hole-doped cuprates [23, 24]. Indeed, mobile vortices in LSCO and signs of localized pairs in $La_{1.88}Ba_{0.12}CuO_4$ on the insulating phase have been observed [171, 172]. However, electron-doped PCCO shows different behaviour in both carrier- and *B*-tuned SITs, with lower values of R_c, which is not consistent with the bosonic scenario. This probably suggests that there are fermionic excitations contributing to the conduction near SIT in PCCO [67]. At finite temperature, the conduction at the critical point includes the contribution of both the bosons and fermionic excitations: $\sigma_c=\sigma_b+\sigma_f$. Considering that $\sigma_b=1/R_b$, $\sigma_f=1/R_f$ and $R_c=1/\sigma_c=R_f/(1+R_f/R_b)=R_b/(1+R_b/R_f)$, where R_b is determined by bosons and is expected to be close to R_Q at the critical point, and R_f is determined by fermionic excitations and is expected to be close to normal state resistance R_n, if the fermionic excitations contribute significantly to

the conduction at the critical point, i.e., $R_f << R_b$, we expect that R_c is close to $R_f \sim R_n$ and lower than $R_b \sim R_Q$. Indeed, R_c exhibits similar value to R_n at each doping level in the *B*-tuned SITs (Figure 4.19(d)), besides the observation that R_c is significantly lower than R_Q.

The existence of fermionic excitations should be further demonstrated by the relationship between R_c and carrier density. At higher doping level, more electrons contribute to the conduction and the R_n decreases with increasing doping level (Figure 4.19(d)). In the *B*-induced SIT, R_c is not universal at three different doping levels. It shares the same evolution with R_n, which suggests that R_c is much more related to the electron concentration. Moreover, for the carrier-tuned SITs, x_c in PCCO is 0.118, two times higher than those in LSCO (x_c=0.0605) and YBCO (x_c=0.048) [23, 24], which means that the carrier density at which SIT occurs in PCCO is higher than that in hole-doped one. The higher carrier density can also be indicated by the lower R_n near superconducting transition shown in Figure 4.10, compared to hole-doped cuprates [23, 24]. This observation coupled with the lower value of R_c in PCCO suggests that R_c is also related to carrier density in carrier-induced SIT. Such relationship between R_c and carrier density suggests that the conduction is mainly governed by fermionic excitations, i.e., unpaired electrons, which cause R_c to be close to R_n. Moreover, these observations demonstrate that fermionic excitations at the insulating side of SIT in cuprates may occur in superconducting cuprate phases with higher carrier density. Interestingly, the phase fluctuations which are associated with the preservation of bosons in SITs, has been demonstrated to be favored in superconductors with a low superfluid density, rather than those with a high superfluid density [173].

One may expect that the formation of fermionic excitations could be related to the vanishing of superconducting energy gap [69, 174]. Interestingly, tunnelling experiment showed that in $Pr_{2-x}Ce_xCuO_4$, the superconducting gap disappears as the superconductivity was suppressed by lowering the doping level to x=0.11 and increasing the magnetic field to be higher than H_{c2} at $T<T_c$ [45-48]. Even though a normal state gap formed after the suppression of

superconductivity, whether it is related to electron pairing is still under debate [45-48]. Our results seem to suggest the unpaired state of electrons in the insulating phase.

4.4 Summary

Using electric field effect in EDLT configuration, the carrier density in electron-doped cuprate PCCO ultrathin film was quasi-continuously tuned and 2D-SIT was induced. Finite-size scaling analysis suggests that this carrier-tuned SIT is a 2D-QPT and the transition is governed by quantum percolation effect. Critical sheet resistance R_c at SIT was found to be 2.35 kΩ which is much lower than the quantum pair resistance R_Q=6.45 kΩ. This is in contrast to those in hole-doped cuprates in which $R_c \approx R_Q$ was observed. This suggests that there is formation of fermionic excitations at the insulating phase in PCCO, as opposed to the preservation of bosons which is suggested in hole-doped cuprates. *B*-induced SITs in superconducting EDLTs with three different doping levels were also performed. Finite-size scaling analysis suggests that *B*-induced SITs are also 2D-QPTs, but the transitions are governed by classical percolation effect rather than quantum percolation effect. R_c at three doping levels are also lower than R_Q, and decrease with increasing doping level and similar to normal-state resistance R_n at each doping level. Thus, fermionic excitations are also suggested in *B*-induced SITs. These results coupled with the comparison in carrier-tuned SITs between PCCO and hole-doped cuprates demonstrate that fermionic excitations at the insulating side of SITs in cuprates may occur in superconducting cuprate phases with higher carrier density.

Chapter 5 Ionic liquid-assisted electric field effect in oxide heterostructures

In this chapter, we performed electric field effect using EDLT configuration to modify the electrical transport properties in patterned $LaAlO_3/SrTiO_3$ (LAO/STO) interfaces. The patterning of LAO/STO Hall-bar devices and the transport measurements of the patterned devices were demonstrated. The resistances and current-voltage (I-V) curves before and after covering ionic liquid were measured and compared, and the results suggest the interface-surface coupling. By applying gate voltages, reversible metal-insulator transition, field-effect transistor operation in LAO/STO 2DEG were observed. Sheet resistance, carrier density and mobility as a function of temperature at different gate voltages were also measured. The carrier density was reduced, and thus, mobility was enhanced at low gate voltage. Due to the enhancement of mobility, Shubnikov-de Hass oscillations of the conductance were observed.

5.1 Introduction

Since the discovery of conducting LAO/STO quasi-two-dimensional electron gas (q2-DEG), various techniques have been employed to tune the electrical transport properties for both fundamental understanding and potential application. The most common technique is the back gating, an electric field effect using STO substrate as the dielectric material. Thiel *et al* demonstrated insulator-to-metal transition in initially insulating 3 uc LAO/STO interface by applying a back-gate voltage [95]. Caviglia *et al* showed back gate-induced superconductor-to-insulator transition at low temperature [9]. Moreover, mobility, 2D quantum oscillations and spin-orbit interaction were also modulated using such a back gating method [10, 99, 104]. In contrast to back gating, an electric field could also be applied through LAO top layer. In such top-gating configuration, LAO layer, ferroelectric materials and ionic liquid are used for the dielectrics. Using LAO as the top gate insulator and Au or YBCO as gate electrodes, transistor operation, mobility enhancement and complete on/off switching of (super-) conductivity were observed [175-177]. A ferroelectric modulation of the 2DEG conduction was demonstrated using $Pb(Zr_{0.2}Ti_{0.8})O_3$ (PZT), suggesting the possibility of non-volatile

control of interface [178]. More recently, metal-insulator transition (MIT) in 3 uc LAO/STO has been induced by ionic liquid-assisted electric field effect [179]. Compared to back gating induced MIT, in which high gate voltage of hundreds of volts is required, liquid gating only needs several volts.

Besides electric field effects, capping layer and surface adsorbents on top of LAO, and even light illumination could also modify the electrical transport properties of LAO/STO interface. Using $La_{1-x}Sr_xMnO_3$ as the capping layers, an insulating 3uc LAO/STO was induced to a metallic state and the carrier density was tuned to a lower value as the strontium content in $La_{1-x}Sr_xMnO_3$ is increased [180]. Incorporation of a $SrCuO_2$ as a capping layer could reduce the impurity scattering at LAO/STO interface and enhance electron mobility [181]. For the surface adsorbents, it has been shown that the application of polar chemical solvents such as acetone, ethanol and water could cause a large modulation of conductivity and even metallic to semiconducting transition, suggesting potential application in polar molecule sensor [182, 183]. The modulation of electrical properties by the capping layer and surface adsorbents strongly suggests the correlation between the interface and the surface charge states. Under the laser illumination, reversible insulator-metal transition could be tuned at LAO/STO interface, usefull for non-volatile memory application [184].

The modulation of LAO/STO interface could also be done at nano-scale structures. In Jeremy Levy's group, they used conductive probe atomic force microscopy (AFM) to define nano-structures in LAO/STO [185, 186]. In an insulating sample, by using conductive AFM, they were able to locally polarize the LAO surface, and cause reversible switch between insulating and conducting states depending on the polarization of the voltage on the AFM probe. This technique enabled the creation of nano-scale tunnelling junctions and field-effect transistors [186]. One-dimensional conducing channel formed at the boundary between two tiled structures composed of alternating one and three $LaAlO_3$ unit cells. This conductance could be tuned to exhibit qauntized steps by electric field [187].

The discussions above strongly indicate the possibility of modulation of carrier density, conductivity, and thus mobility in LAO/STO. This suggests that we can exploit a flexible and powerful way to construct high-mobility LAO/STO interface which exhibits quantum transport. In this chapter, we demonstrate the modulation of electrical transport properties in LAO/STO interface by electric field effect using electric double layer transistor (EDLT) configuration. Surface-interface coupling, reversible metallic-insulating phase transitions, transistor operation can be induced in initially metallic samples. The electron mobility can be enhanced by reducing the carrier density. Due to enhancement of mobility, we can observe quantum oscillations of the conductance at liquid-gated LAO/STO interface.

5.2 Patterning of $LaAlO_3/SrTiO_3$ 2DEG

Many fundamental studies have demonstrated various interesting properties in LAO/STO 2DEG. Most of the studies on electrical transport properties have been performed with square unpatterned samples and using the van der Pauw method. However, for potential applications and other studies such as quantum-Hall transport, devices with a well-defined pattern are required. The straightforward method is to use Ar-ion etching which has been used extensively to produce controlled structures in various materials. However, the damage created by the ion beam bombardment will cause the STO substrate to be conducting and thereby shunts the 2DEG. Alternatively, previous studies have shown that the patterns could be defined by UV lithography and deposition of amorphous LAO or AlO_x as the hard mask [10, 188, 189]. In some of these studies, two deposition steps of LAO, and thus, two cycles of heating of sample are required [188]. In another case, a hard mask such as amorphous AlO_x was first directly grown on the STO before the preparation of the LAO/STO interface, and then was patterned and developed by certain solution [189]. This may cause the degradation of STO surface and the resultant LAO/STO interface. Scanning probe microscopy has also been implemented to define structures down to nanoscales [185, 186]. However, it is difficult to implement this technique to large-area and large-quantity devices. In this section, we demonstrate the direct patterning of LAO/STO 2DEG using conventional lithography and

deposition of amorphous AlN as the hard mask. The STO substrates are still clean after patterning and the patterned LAO/STO interface shows comparable transport properties to the unpatterned samples. The possibility of interface patterning enables us to perform the ionic liquid-assisted electric field effect on LAO/STO 2DEG.

5.2.1 Thin film growth

The LAO/STO heterostructures were obtained by depositing LAO on STO substrates using pulsed laser deposition (PLD) system. For the patterned LAO/STO interfaces, STO substrates were patterned before the deposition of LAO films which will be shown below. LAO target is single crystal. STO substrates were put into the PLD chamber with a background pressure less than 10^{-7} Torr and heated up to the temperature (T) of 740 ^{o}C at oxygen partial pressure (P_{O2}) of $2x10^{-3}$ Torr. The deposition was done at T=740 ^{o}C and P_{O2}=$2x10^{-3}$ Torr. The frequency of pulsed laser was set to be 1 or 2 Hz and the laser energy density to be 1~2 J/cm^2. After deposition, the samples were cooled down to room T in the deposition pressure at a rate of 15 ^{o}C/min. In order to remove the oxygen vacancies in STO substrates introduced by high-energy plasma bombardment during the deposition, the samples were annealed in a tube furnace at 550 ^{o}C for 1 hour in air.

During the deposition, an *in-situ* high pressure reflection high energy electron diffraction (RHEED) was used to monitor the thickness of LAO. Figure 5.1 shows the RHEED intensity as a function of time during deposition for 20 unit cell LAO grown on a STO (100) substrate. Obvious oscillations are observed from the start until end of deposition, indicating atomic scale layer-by-layer growth. Such growth mode is necessary to obtain the high quality interface.

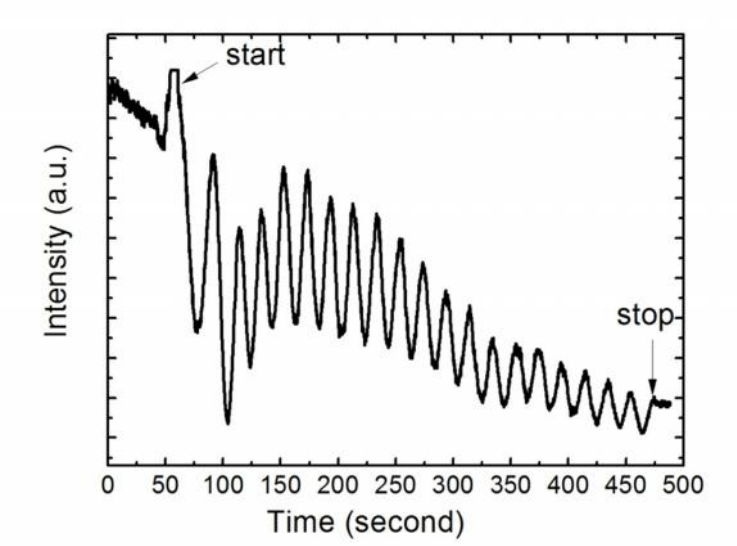

Figure 5.1 RHEED oscillations during the deposition of 20-uc LAO on a STO (100) substrate.

5.2.2 Patterning

For the device preparation, STO substrates were patterned before the deposition of LAO films. TiO_2-terminated STO was patterned into typical Hall bar geometry by using conventional photolithography and depositing amorphous AlN (a-AlN) films by PLD as hard masks. The detailed process for STO patterning is shown in Chapter 4 in Figure 4.6 (a)-(e). An optical micrograph of a Hall-bar pattern and a lateral gate electrode on STO is shown in Figure 5.2(a). In this pattern, the width of the Hall bar is 50 μm and length is 500 μm, the distance between two voltage probes is 160 μm. A six-probe configuration of the Hall bar allows for the measurement of both longitudinal and Hall resistance. After patterning process, the substrate surfaces were still clean and atomically flat with single termination, as was confirmed by atomic force microscopy (AFM). Figure 5.2(b)-(c) show the AFM images for 5, 10 and 20 uc LAO grown patterned STO substrates, respectively. Clear atomic terraces are observed, indicating the smooth surface of patterned substrates and high-quality thin films. It should be noted that the large ratio of the area for the deposition of LAO to the one covered by a-AlN allows direct observation of RHEED oscillation on patterned STO. A bare STO substrate for the calibration of LAO thickness is not necessary. These allow the precise

control of LAO thickness in patterned devices. The RHEED oscillations shown in Figure 5.1 is the one observed in patterned STO.

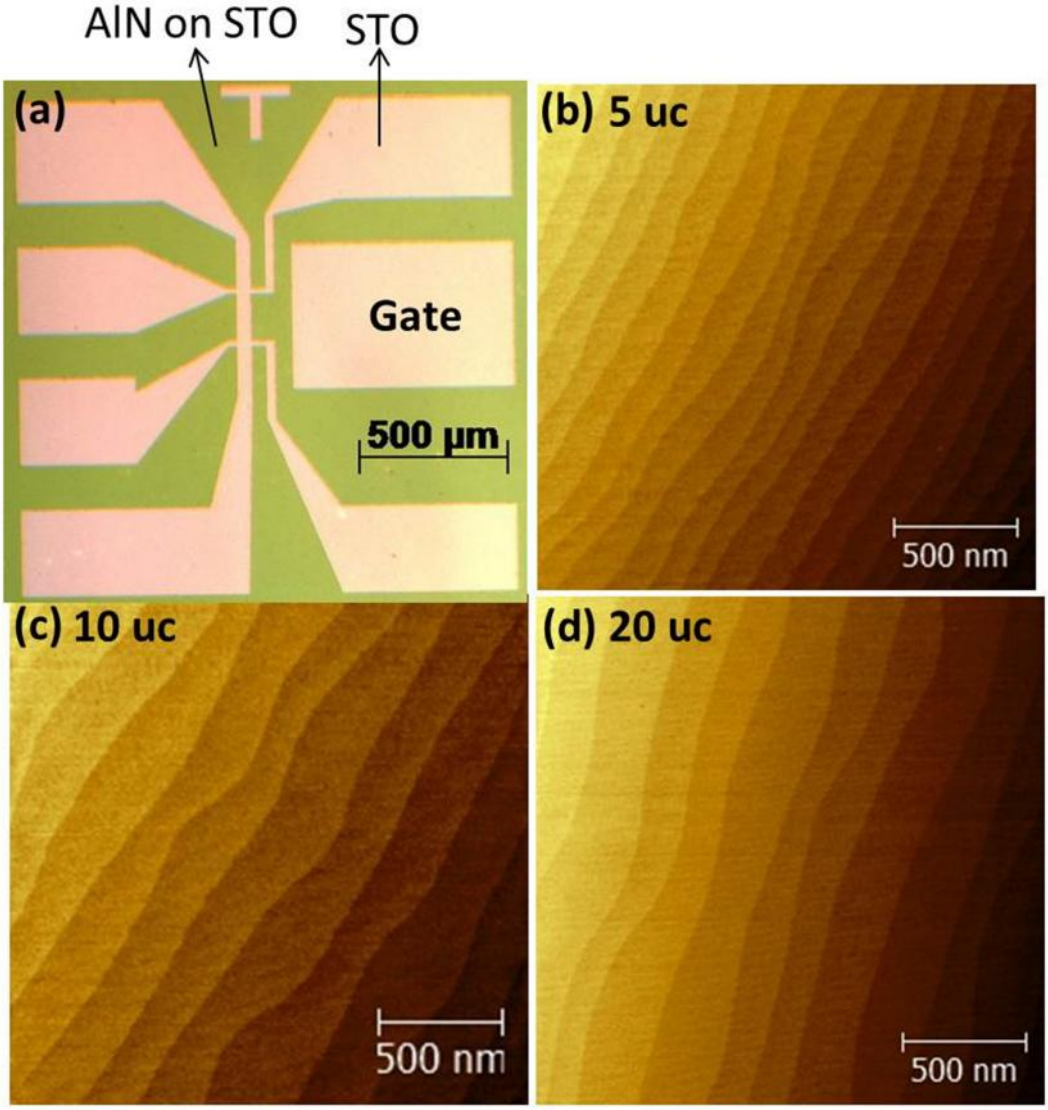

Figure 5.2 (a) Optical micrograph of a Hall-bar pattern on STO using amorphous AlN as the mask. Atomic force microscopy images for (b) 5 uc, (c) 10 uc, (d) 20 uc LAO grown patterned STO substrates, measured in the region of Hall bar channel.

5.2.3 Electrical Transport on the patterned LAO/STO interface

Figure 5.3 shows the temperature dependence of the sheet resistance R_s for 6 uc LAO/STO interfaces. The unpatterned sample was obtained by direct deposition of LAO on bare 5mm×5mm STO substrate and the transport data was measured using the van der Pauw

configuration. Patterned 1 and Patterned 2 are two Hall-bar devices on a STO substrate. Both the unpatterned and patterned samples are synthesized in one deposition. The wire connection for transport measurement of all samples was done by direct Al ultrasonic wire bonding. One can see that LAO/STO interfaces in unpatterned and Hall-bar configurations show very similar transport properties, metallic behaviour with comparable sheet resistances.

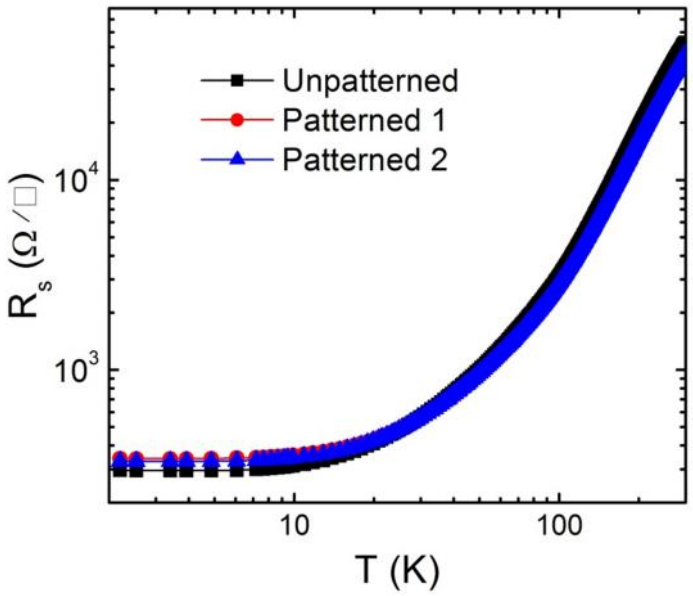

Figure 5.3 Sheet resistance R_s as a function of temperature for 6 uc $LaAlO_3/SrTiO_3$ interfaces. The unpatterned sample was obtained by direct deposition of $LaAlO_3$ on bare $SrTiO_3$ substrate. Patterned 1 and Patterned 2 are two Hall-bar devices on a $SrTiO_3$ substrate.

The temperature dependencies of the corresponding sheet carrier density n_s and carrier mobility μ_H are shown in Figure 5.4, which were determined by $n_s = -1/(e \cdot R_H)$ and $\mu_H = 1/(e \cdot n_s \cdot R_s)$, where R_H is the Hall coefficient, R_s is the sheet resistance and e is the elementary charge. It can be seen that n_s and μ_H show comparable values in both unpatterned and patterned samples, even though slightly lower n_s and higher μ_H in the unpatterned sample. The carrier densities exhibit little T dependence, are ~2.5×10^{13} cm^{-2} from 300 to 2 K for the Hall-bar devices, and from ~2.4×10^{13} cm^{-2} at 300 K to ~1.8×10^{13} cm^{-2} at 2 K for the unpatterned sample. The mobility shows a relatively small value of ~6 cm^2/Vs at 300 K for all samples due to the electron-phonon scattering, and increases to ~1170 cm^2/Vs at 2 K for the

unpatterned sample and ~720 cm^2/Vs at 2 K for the patterned sample. These values of carrier density and mobility at low T are lower than those in patterned devices which were not annealed in oxygen ambience [189] and nano-patterned devices [190]. Nevertheless, they are comparable to the samples which were annealed in oxygen ambience, observed in previous reports [95, 121, 175, 182]. It can be also seen that the Hall-bar devices show remarkable similar values of R_s, n_s and μ_H at all temperature range, which demonstrates that the patterning of Hall-bar devices are reproducible.

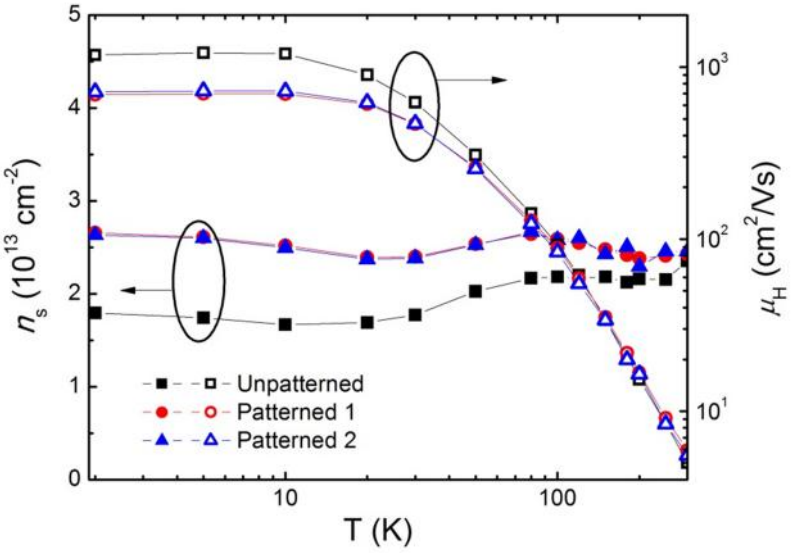

Figure 5.4 Sheet carrier density n_s and carrier mobility μ_H as a function of temperature for 6 uc $LaAlO_3/SrTiO_3$ interfaces, for unpatterned and patterned samples.

5.3 Ionic liquid-assisted electric field effect

5.3.1 Measurement setup

After the thin film growth, we did not carry out any processing step such as lithography because exposing LAO to other chemicals may change the surface and interface. The wire connection for transport measurement was done by direct Al ultrasonic wire bonding. For the connection of gate electrodes, Al wires were first bonded to the lateral gate pads, and then a small amount of silver paint is dropped to cover the gate pad, as is shown in Figure 5.5(a). The silver paint is used to enlarge the area of the gate electrode, enabling the accumulation of

ions. A small droplet of an ionic liquid (IL), N,N-diethyl-N-methyl-N-(2-methoxyethyl)ammonium bis(trifluoromethyl sulphonyl)imide (DEME-TFSI), was put onto the sample and covered both the conducting channel and the gate electrode, as is shown in Figure 5.5(b). The sample was then placed in the chamber of a Quantum Design Physical Property Measurement System (PPMS). The transport measurements were made in PPMS using the built-in Source Measure Units (SMU) and Keithley SMU. For the resistance-gate voltage curves (R-V_G) curves, source drain current-V_G (I_{SD}-V_G) curves and the corresponding gate current-V_G (I_G-V_G) curves, we use Keithley 2400 Sourcemeters and Keithley 2002 Multimeters for the measurements and Keithley 2400 Sourcemeters for applying V_G. For the resistance-temperature (R-T) curves at different V_G, we use PPMS built-in SMU for the measurements and Keithley 2400 Sourcemeters for applying V_G. For the R-T curve measurements, the V_G was applied at 230 K and kept for 10-20 minutes for charging. Resistance measurement was made as the samples were cooled down while keeping the V_G constant. In order to change V_G, the sample was heated to 230 K after each R-T curve and a new V_G was applied.

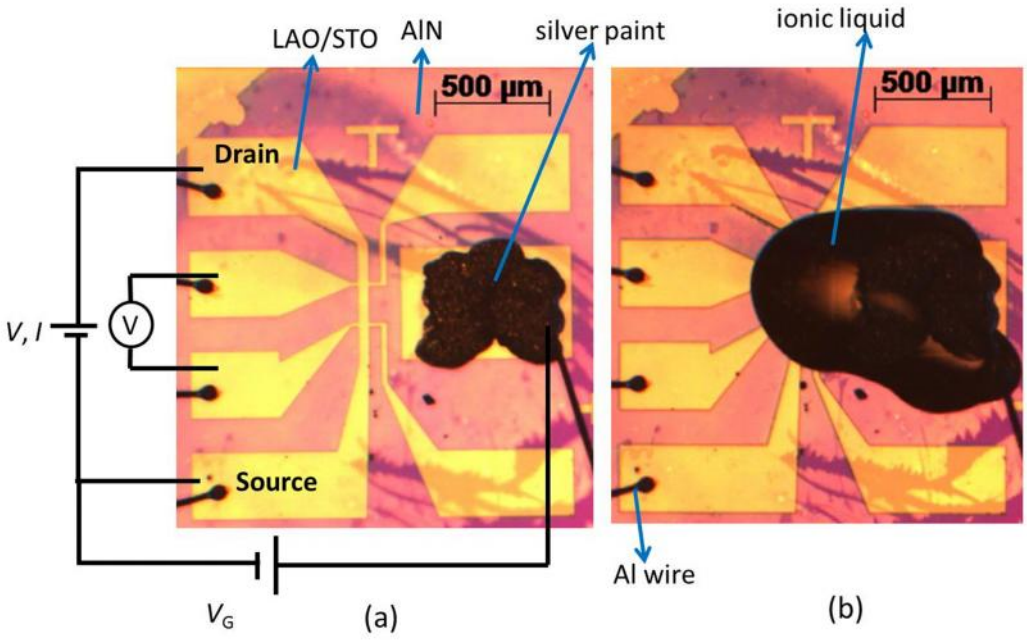

Figure 5.5 (a) Device with a small droplet of silver paint covering the lateral gate electrode. (b) Device with an ionic liquid droplet covering the Hall-bar channel and gate electrode. The measurement circuit is also shown in (a).

5.3.2 Interface-surface coupling

Figure 5.6 shows current-voltage (*I*-*V*) curves of a 10 uc LAO/STO interface with and without ionic liquid on the LAO surface, measured in a two-probe configuration. It can be seen that the *I*-*V* curve without ionic liquid shows perfect linear behaviour for voltage up to 8 V, indicating the metallic conducting channel and Ohmic contacts of the drain and source probes. When an ionic liquid droplet is put on top of the conducting channel (inset of Figure 5.6), transistor-like *I*-*V* curve is observed, with strong saturation of current at high voltage. At *V*=8 V, current is suppressed by almost one order of magnitude. This suggests that the conducting state of LAO/STO interface is changed after the application of ionic liquid.

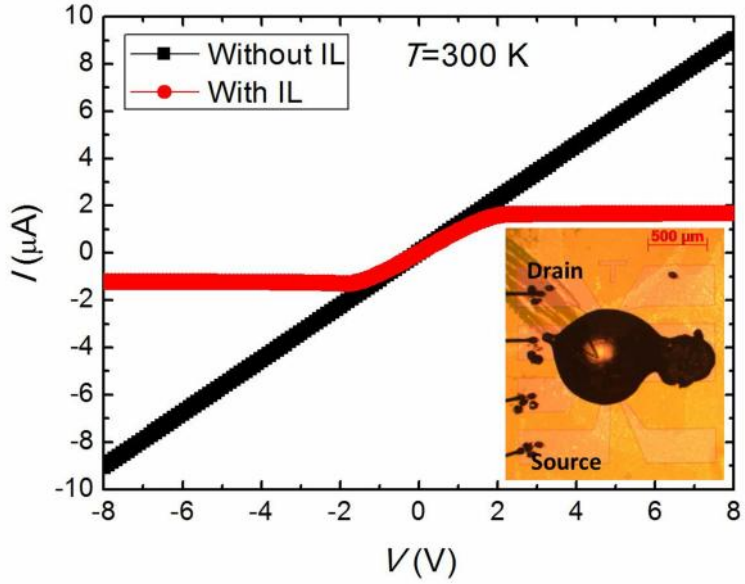

Figure 5.6 Current-voltage (*I*-*V*) characteristics of a 10 uc LAO/STO Hall-bar device with/without ionic liquid (IL) droplet on top of the LAO surface. The measurements were performed in a two-probe method and at *T*=300 K. The inset is the microscopic image of the device with ionic liquid on top of the surface. During the measurement, the voltage is applied between the drain and source probes. There is no Al wire connection between the Hall-bar channels and the gate electrodes, in contrast to gating measurement shown in Figure 5.5.

To further confirm the change of the conducting state, the resistance as a function of time before and after application of ionic liquid was collected and shown in Figure 5.7. It can be seen that the resistance remains unchanged before application of ionic liquid, while it jumps

sharply up to a certain value after application of ionic liquid, and then keeps increasing with time.

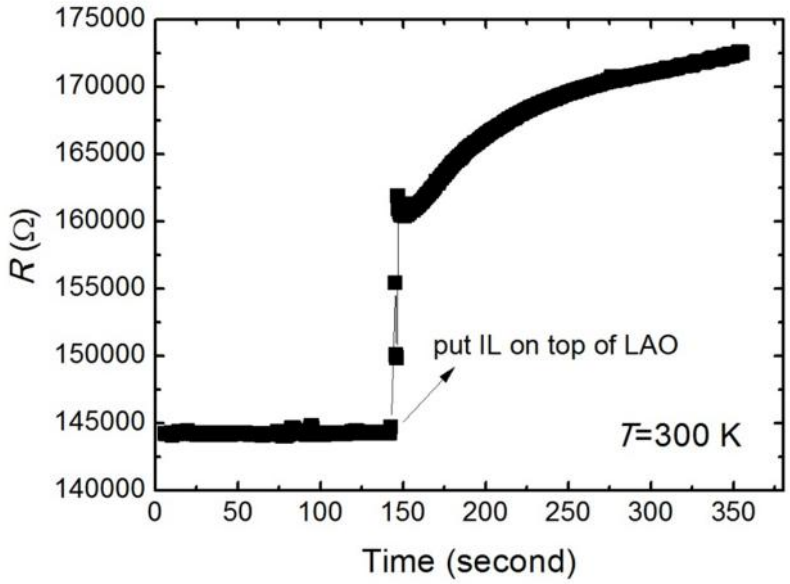

Figure 5.7 Resistance as a function of time for a 10 uc LAO/STO Hall-bar device with ionic liquid droplet on top of LAO surface. The resistance was measured in four-probe method.

To explain the change of conducting state caused by ionic liquid, in Figure 5.8 we show a schematic diagram illustrating the effect of ionic liquid on the polarization field in LAO layer. Since LAO is a polar oxide with a stack of positively charged $(LaO)^{1+}$ and negatively charged $(AlO_2)^{1-}$ sublayers, the polarization field points from the substrate to the surface when LAO is grown on STO substrate. When an ionic liquid droplet is put on the LAO surface, the anions tend to accumulate on LAO surface, and therefore, the polarization field is reduced and reaches a relatively more stable state. The reduced polarization field causes the change of band structure in LAO/STO interface and the resultant reduced carrier density. This is the reason why the resistance is enhanced with ionic liquid on the surface, as can be observed in Figure 5.7. The conductivity change in LAO/STO interfaces has also been observed in samples with LAO surface polar molecular adsorbates [182, 183].

The non-linear *I-V* curve can be explained if the area of LAO/STO without ionic liquid is considered as a metal and the area underlying ionic liquid is considered as an n-type

semiconductor [183]. In this case, throughout the ionic liquid area from drain to source, there are two metal-semiconductor Schottky junctions. At V=0 V, the Fermi levels of the metallic and semiconducting LAO/STO are on the same level and there is no net carriers across two Sckottky barriers. For non-zero V, the Fermi level in one metallic LAO/STO side with V>0 V is higher than that in semiconducting LAO/STO, the Sckottky barrier at this side disappears and carriers can pass through the semiconducting LAO/STO and tunnel through another barrier. Thus, the current increases with increasing voltage. However, at higher voltages, the carriers reach the limit of tunneling of another barrier, and therefore, the current saturates. This result suggests that the conducting state at LAO/STO interface could be affected by covering the charged adsorbent on the surface.

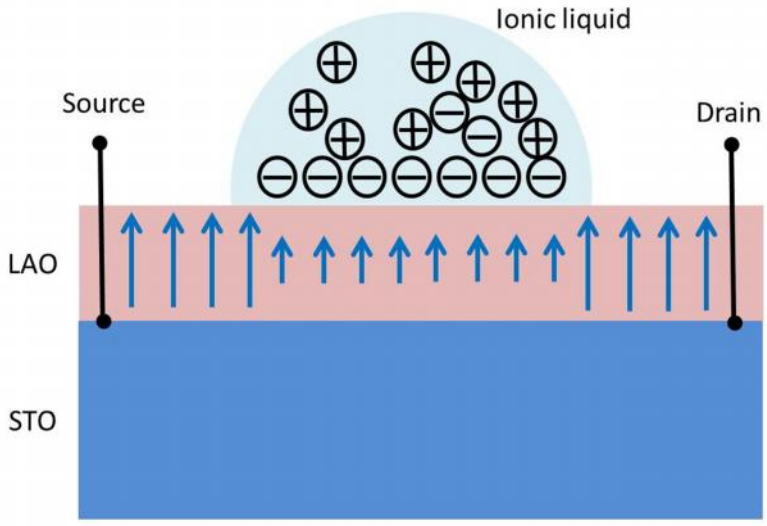

Figure 5.8 Schematic diagram illustrating the effect of ionic liquid on the polarization field in LAO layer. Due to the accumulation of anions on the LAO surface, the polarization field in the LAO layer covered by ionic liquid is reduced (indicated by small arrow), compared to that without ionic liquid (indicated by larger arrow).

5.3.3 Gate-induced metal-insulator transition

We have shown in previous section that ionic liquid on top of LAO surface affected the conducting state of underlying LAO/STO interface. However, only small increase in resistance is observed (Figure 5.7), which is far away from the insulating state. Heavy

accumulation of anions on surface will further increase the resistance and reach the metal-insulator transition. This can be realized by electric field effect by applying external gate voltage. The measurement circuit of field effect is shown in Figure 5.5(a). Figure 5.9(a) shows the resistance as a function of gate voltage for a 10 uc LAO/STO device measured at T=300 K. It can be seen that resistance increases with decreasing gate voltage, and up to the measurement limit at $V_G \approx$ -0.6V. The V_G to obtain the insulating state is significantly lower than that (V_G ~100 V) in back-gating device [95]. The scan measurements were performed for three cycles, reversible metal-insulator transition is preserved and no obvious hysteresis is observed. This is because the movement of ions in ionic liquid is quite fast, the sample can immediately move to a new charging state if the gate voltage is changed, suggesting a potential application for switching devices. Figure 5.9(b) shows resistance as a function V_G for different temperature, taken with decreasing V_G. One can see that at each temperature point, metal to insulator transition is observed and the V_G at which the resistance reaches the measurement limit is the same.

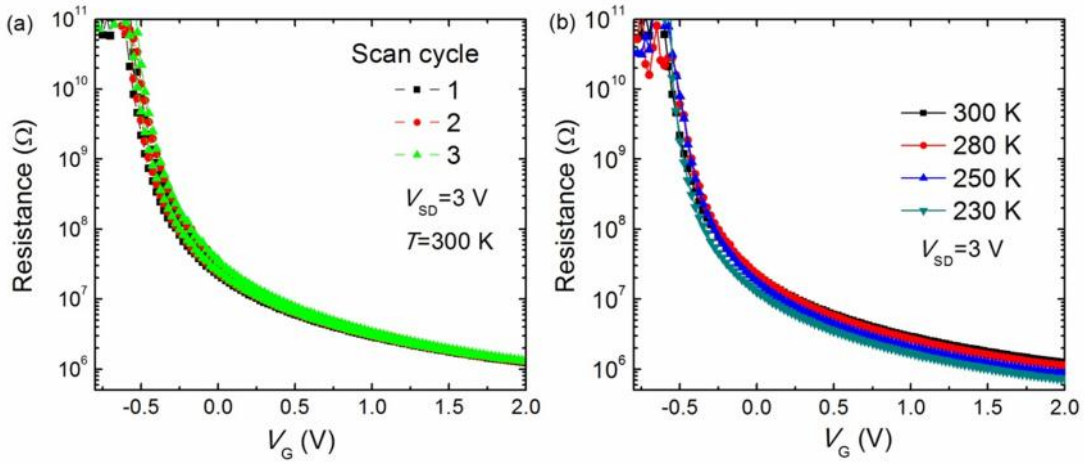

Figure 5.9 (a) Resistance as a function of gate voltage (V_G) for a 10 uc LAO/STO interface for three scan cycles. (b) Resistance as a function V_G for different temperatures, taken with decreasing V_G. The measurement was performed in a two-probe method and with a scan speed of 25 mV/s.

We draw schematic diagram of the band structures to explain the electric field-induced metal-insulator transition, as is shown in Figure 5.10. For an idealized LAO/STO interface free from

surface states, electrons at the interface come from the electrons at the valence band of LAO [110, 191]. The electrons sit in the well caused by band bending of STO at the interface and with energy lower than the Fermi level (Figure 5.10(a)). For V_G>0 V, the cations accumulate on LAO surface, which causes the band bending to be more pronounce. More states with energy lower than the Fermi level are created in the well and can accept more electrons transferred from valence band of LAO (Figure 5.10(b)). Therefore, the carrier density at the interface is enhanced and resistance is reduced. For V_G<0 V, anions accumulate on LAO surface causing the band bending to be relaxed. Electrons transfer back to LAO valence band and the resistance increases. At certain negative V_G, there is no state with energy lower than Fermi level, and the sample is insulator (Figure 5.10(c)).

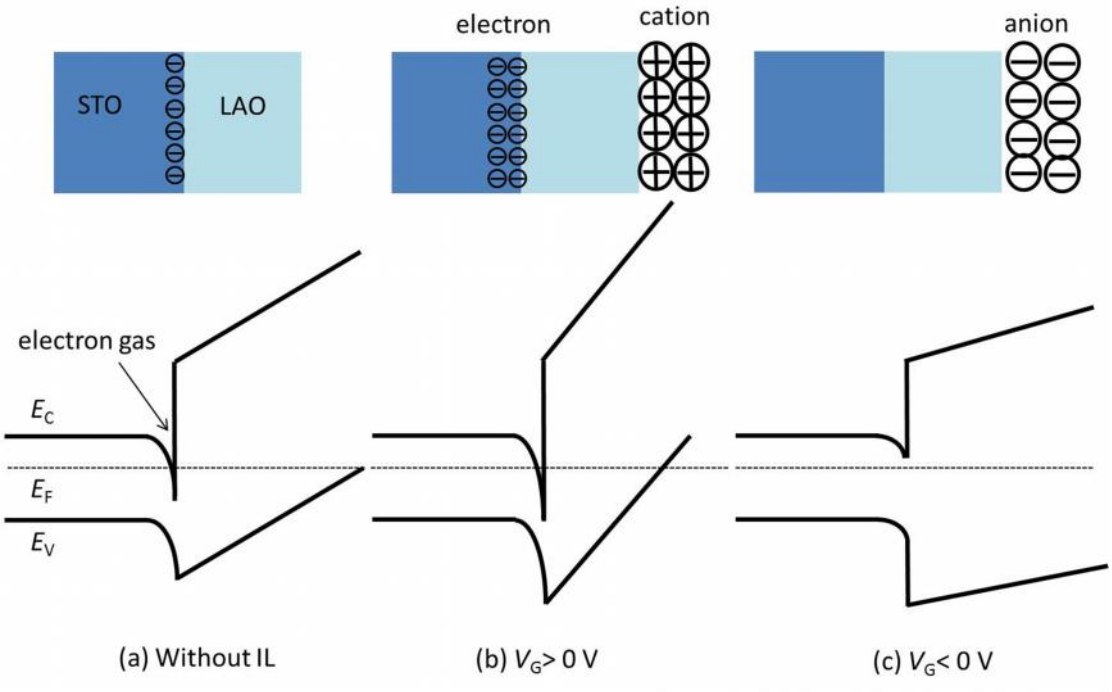

Figure 5.10 Schematic diagram of the band structures of LAO/STO heterostructures. (a) Without IL on top of LAO, (b) V_G>0 V, (c) V_G<0 V.

We also recorded the leakage current (I_G) between the Hall-bar channel and the gate electrode, and plotted it as a function of gate voltage in Figure 5.11. It can be seen that I_G is less than 0.4 nA for -0.8 V≤V_G≤2 V. It does not change with the change of gate voltage and shows random

value within ±0.4 nA, indicating good operation of electric field-effect device. This is in contrast to the observation in the top-gated device using LAO as gate insulator, in which the leakage current increases with increasing magnitude of gate voltage [175, 176]. Note that even the gate voltage is applied to higher value, for example, up to -4 or +3 V, the leakage current is still negligibly small. These indicate that the metal to insulator transition shown above is not due to leakage in the device, and that it is safe to apply higher gate voltage to obtain more reliable metal-insulator transition for on-off switching applications (Figure 5.12).

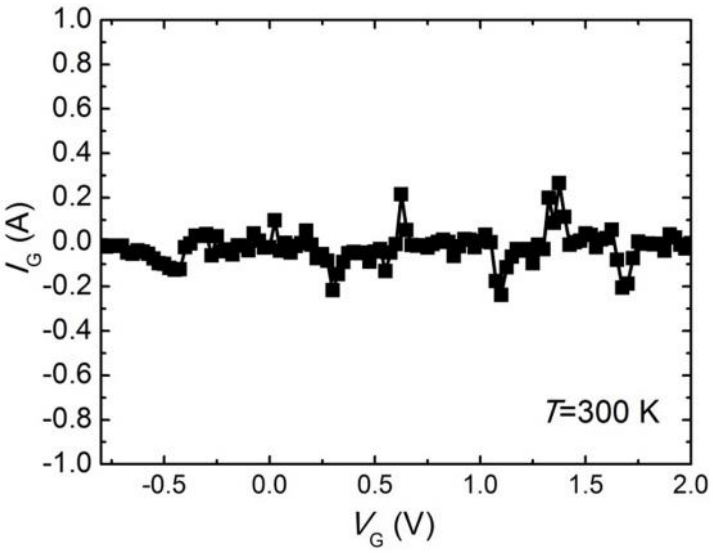

Figure 5.11 Leakage current (I_G) as a function of gate voltage (V_G).

Figure 5.12 shows the resistance and the applied gate voltage as a function of time. By switching the gate voltage between -2 V and 2 V, the resistance could be reversibly switched between a low value of ~1×10^7 Ω (V_G=2V) and an unmeasurable value of ~4×10^{10} Ω (V_G= -2V), indicating the reversible on-off states with a ratio of ~10^4. This on-off switching is obtained at a V_G of ±2 V, significantly lower than that (V_G ~100 V) in back-gating device [95] and comparable to those in top-gating devices using LAO as dielectric materials [175-177].

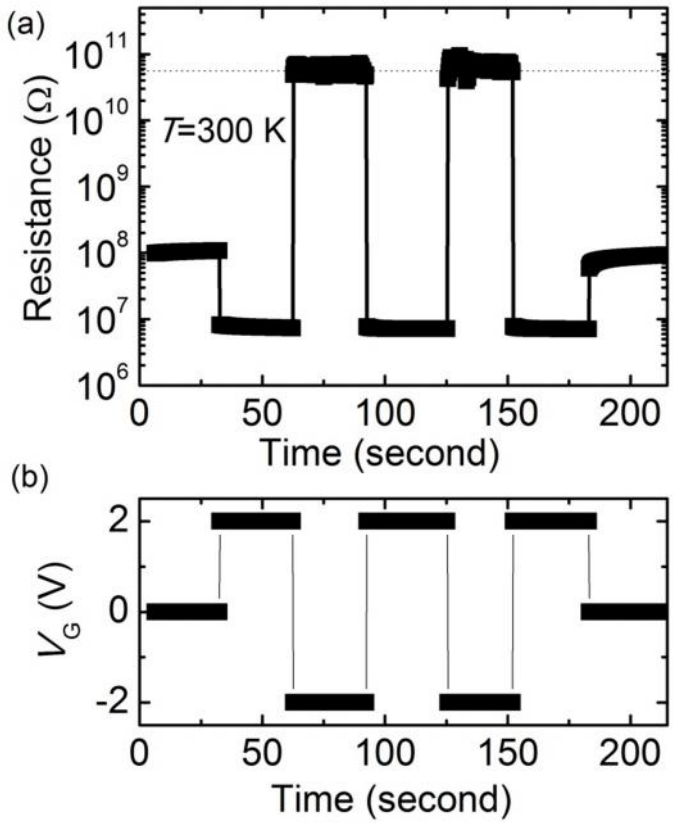

Figure 5.12 (a) Resistance and (b) gate voltage (V_G) as a function of time.

5.3.4 Transistor operation in $LaAlO_3/SrTiO_3$ 2DEG

Field-effect transistors (FETs) are the backbone of modern electronics, especially the silicon-based devices. Recently, FET operations in complex oxides, especially in the strongly correlated electron systems, have been explored in order to enhance the performance of devices and to search for possible roads to overcome the scaling limitations of silicon-based devices [5, 6]. Among these, FET devices based on oxide interfaces such as LAO/STO would be very interesting since they exhibit various novel properties. For LAO/STO 2DEG, even though electric field effect has been extensively explored to induce the change of carrier density and the resultant electrical transport properties such as metal-insulator transition and superconductor-insulator transition, transistor operation was observed in only few reports [175, 177]. In those experiments, LAO is directly used as a gate dielectric and Au or YBCO

are grown on top of LAO as gate electrodes. Here, we show transistor operation of LAO/STO interface using ionic liquid as gate materials.

The measurement circuit of transistor operation is shown in Figure 5.5(a). Figure 5.13 shows gate voltage-dependent I_{DS}-V_{DS} (current-voltage between drain and source) characteristics of a 10uc LAO/STO device at T=300, 280, 250 and 230 K. The measurements were performed in two-probe configuration and with increasing V_{DS}. Clear transistor characteristics are observed at all temperature range. For V_G between -0.2 V and 2 V, pinch-off is seen at each I_{DS}-V_{DS} scan. For example, for T=300 K and V_G=2 V, at low V_{DS}<1 V, I_{DS} increases linearly with increasing V_{DS}. At V_{DS}>1 V, I_{DS} still increases but with a slower rate, and shows saturation as V_{DS}>3.3 V. Differentiating the data of each I_{DS}-V_{DS} curve, we can obtain the pinch-off voltage V_P which is defined as the V_{DS} at dI_{DS}/dV_{DS}=0 or at the point where dI_{DS}/dV_{DS} shows a minimum value. The V_P at each I_{DS}-V_{DS} curve is shown in Figure 5.13, indicated by the black circle. The behaviour of V_P with increasing V_G is similar to that in conventional transistor [1], in top-gated STO single crystal using $CaHfO_3$ as dielectric material [192] and in top-gated LAO/STO interface using LAO as dielectric materials [175, 177]. At the same V_G, V_P shows a higher value at lower temperatures due to the lower resistance of LAO/STO 2DEG at low temperature.

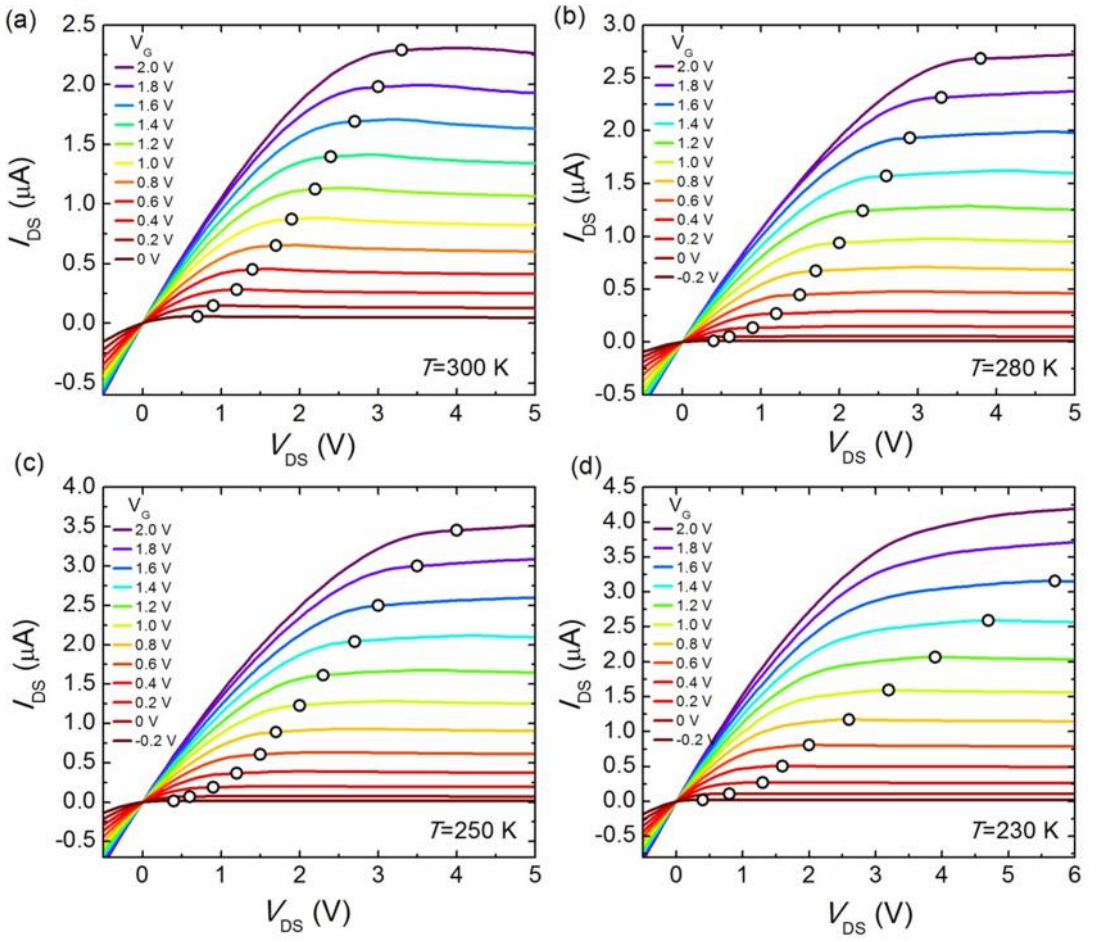

Figure 5.13 Gate voltage-dependent I_{DS}-V_{DS} characteristics of a 10uc LAO/STO device at different temperature measured in two-probe method. All data are taken with increasing V_{DS}. The black circles are the co-ordinates (V_p, $I_{DS,sat}$) on the respective curve, which indicate the saturation of I_{DS} with increasing V_{DS}. $I_{DS,sat}$ is the current at V_{DS}=V_P.

To investigate the relationship between saturation I_{DS} and V_G, we extract I_{DS} at V_{DS}=5 V and plot $(I_{DS})^{0.5}$ as a function of V_G in Figure 5.14. It can be seen that at four temperature points, $(I_{DS})^{0.5}$ is linear with V_G for -0.2 V≤V_G≤1.4 V, indicating essentially ideal quadratic form of I_{DS}-V_G. This is consistent with the gradual-channel model of transistor in the saturation regime [1]. The fitting gives the threshold voltage (V_G at I_{DS}=0) V_{th} of -0.34, -0.32, -0.32 and -0.36 V for temperature of 300, 280, 250 and 230 K, respectively. The V_{th} at four temperature points are similar, which means that the gate voltages required to deplete the conducting channel are the same for different temperatures. This is consistent with the measurement in Figure 5.9, even though the V_{th} observed here is relatively smaller. The V_{th} observed here is smaller than that (V_{th}= -1.1 V) in top-gated LAO/STO using LAO as the gate insulator [175], which means

that the gate voltage depleting the channel in that device is higher than that in our liquid-gated device. This may be because there is surface-interface coupling when the ionic liquid is applied, the carrier density is reduced even without applying gate voltage. The results suggest that ionic liquid-assisted field effect is a more effective tool to tune electrical transport properties of LAO/STO interface.

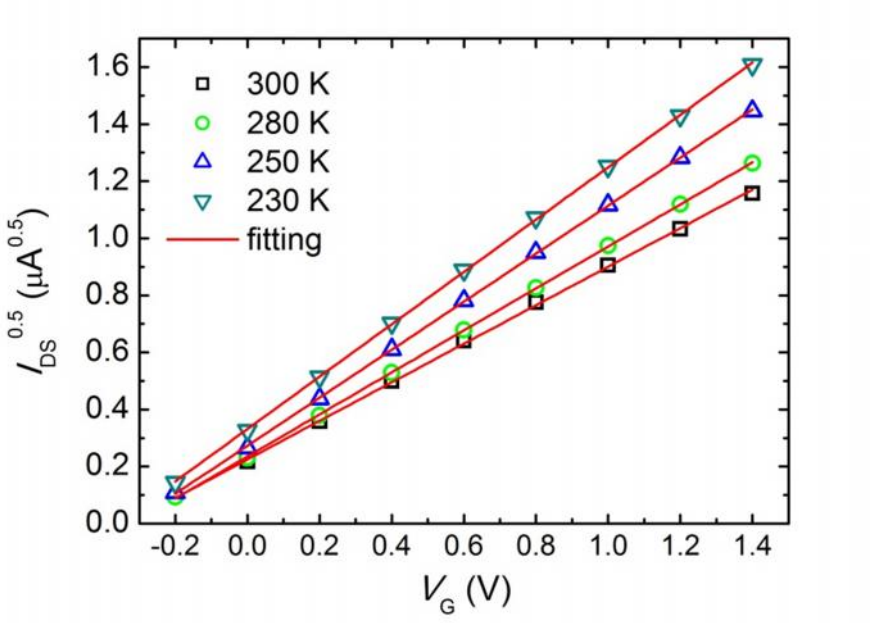

Figure 5.14 $(I_{DS})^{1/2}$ as a function of V_G for different temperature, showing quadratic dependence of I_{DS} on V_G in the saturation region. The I_{DS} is taken at V_{DS}=5 V from Figure 5.13.

Note that the ionic liquid covers only LAO/STO near the Hall bar channel, leaving the area where the Al wires present free from the liquid (Figure 5.5(b)). The carrier depletion and accumulation of LAO/STO interface induced by electric field effect are active only in the area under the ionic liquid. Therefore, the Al wire contacts to drain and source probes are not affected by field effect and still show Ohmic-contact behaviour when gate voltages are applied. This indicates that the transistor operation observed above takes place in the Hall-bar channel, rather than the junctions of the drain and source contacts. To further confirm this, *I-V* curves at different gate voltages using a four-probe method were also measured and shown in Figure 5.15. One can see that the device also shows clear transistor operation. The saturation

current I_{sat} (at V=5 V) also shows quadratic dependence on V_G and the V_{th} is -0.33 V, similar to the one observed in Figure 5.14.

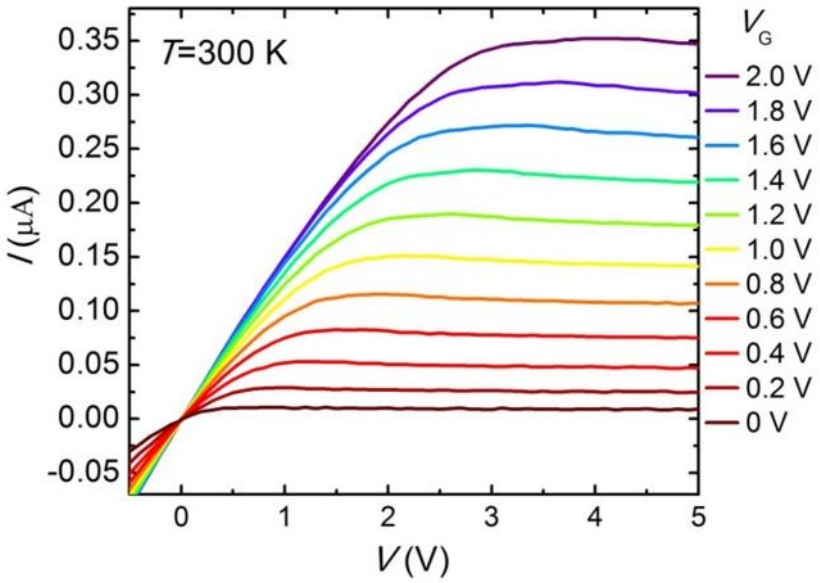

Figure 5.15 Gate voltage-dependent *I*-*V* characteristics of a 10uc LAO/STO device at *T*=300 K, measured in four-probe method.

5.3.5 Enhancement of mobility

As was discussed above, the conducting channel could be tuned to an insulating state by depleting the carriers using applied negative gate voltage. It is expected that carrier mobility could be enhanced if the carrier density is reduced. Here we perform liquid-gated effect on resistance-temperature curves, carrier density, mobility and magnetoresistance in 10 uc LAO/STO interfaces. The measurements were performed by the four-probe method. Figure 5.16 shows the sheet resistance (R_s), sheet carrier density (n_s) and Hall mobility (μ_H) as a function of temperature before the gating experiment. The resistance shows metallic behaviour, decreasing with decreasing T all the way below 300 K. The carrier density exhibits little T dependence, and is ~ 2.5×10^{13} cm^{-2} from 300 to 2 K. The mobility shows a relatively small value of ~6 cm^2/Vs at 300 K due to the electron-phonon scattering, and increases to ~1110 cm^2/Vs at 2 K with decreasing temperature.

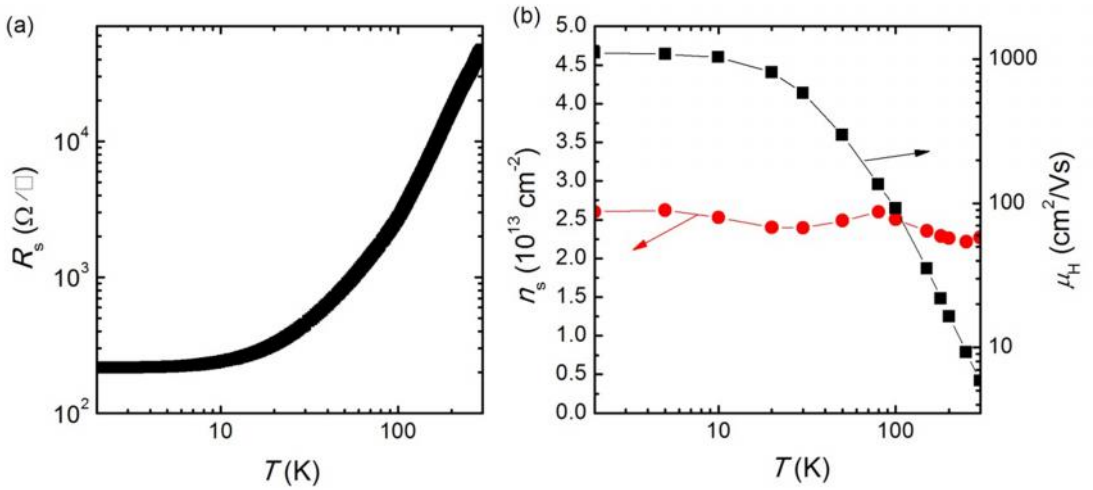

Figure 5.16 (a) Sheet resistance R_s as a function of temperature T for 10 uc LAO/STO interface. (b) Sheet carrier density n_s and mobility μ_H as a function of temperature.

Figure 5.17 shows the sheet resistance vs temperature (R_s-T) curves at various gate voltages. At high T, as the V_G is increased, R_s decreases for the positive V_G and increases for negative V_G. These indicate that positive V_G causes enhancement of carrier density while negative V_G causes reduction of carrier density at the interface, as is shown in Figure 5.18(a). At low T, R_s does not show monotonous change with increasing V_G (Figure 5.17(b)). R_s decreases as V_G is increased from -0.4 to 0 V while increases as V_G is increased from 0 to 3 V. At $V_G \geq 1.5$ V, R_s shows a slight upturn at T below ~5 K, suggesting localization at high V_G. The resistance upturn has also been observed for 3uc LAO/STO metallic samples induced by liquid gating [179]. In that report, the resistance upturn presents at all V_G from 0 to 3 V, and the T_{min} at which resistance shows minimum value is higher (~10 K) at high V_G of 3 V [179]. However, our sample shows lower T_{min} and completely metallic behaviour down to 2 K for $V_G \leq 1$ V. This suggests that charge carriers in conducting interface of our sample are less heavily scattered by defects.

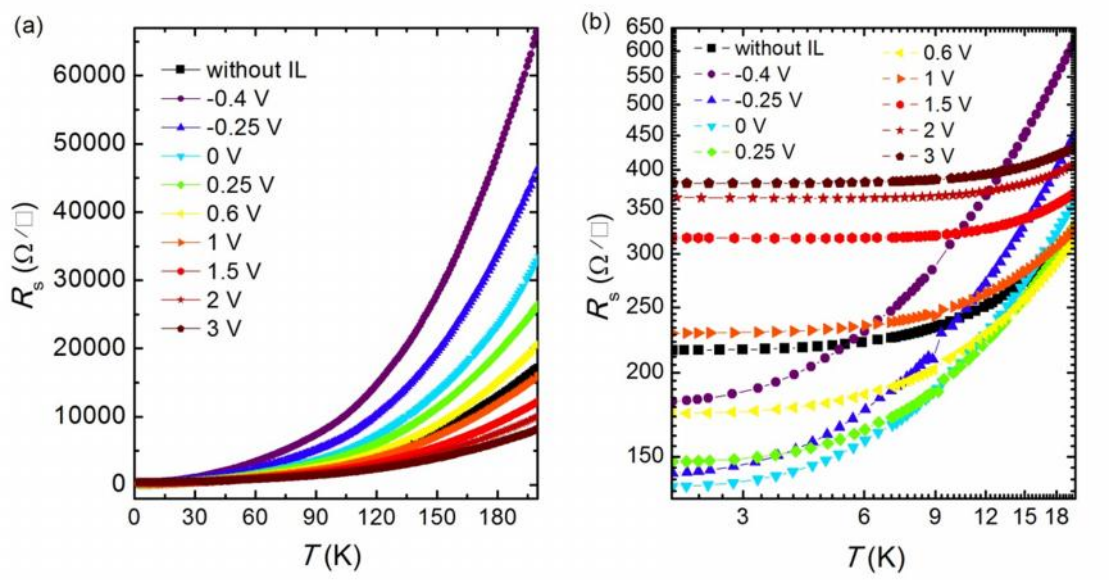

Figure 5.17 (a) The linear-scale sheet resistance vs temperature (R_s-T) curves at various gate voltages. (b) The logarithmic-scale R_s-T curves at low temperature. The black square is the data without ionic liquid (IL) on top of the sample.

To shed light on the accumulation and depletion of charge carriers at the interface, we measured the carrier density through Hall-effects. The carrier density n_s as a function of temperature at various gate voltages is shown in Figure 5.18(a). At high T regime, n_s increases with increasing V_G. Inset of Figure 5.18(a) shows the n_s at 180 K as a function of V_G. One can see that n_s changes quasi-linearly over the whole range of V_G. Such linear change of n_s is consistent with the previous report on carrier density modulation by EDLT in insulating 3 uc LAO/STO interface [179]. However, at low T regime from 20 to 2 K, n_s increases with increasing V_G from -0.4 to 1 V and saturates at ~3×10^{13} cm^{-2} for $V_G \geq 1.5$ V. The saturation of n_s at 2 K can be clearly seen in Figure 5.19.

The T dependent behaviour of n_s is different between the two V_G regimes. For $V_G \leq 1$ V, n_s is nearly T independent at each V_G. For $V_G \geq 1.5$ V, n_s generally decreases with decreasing T, suggesting the carrier freeze-out effect. It has been reported that n_s of the oxygen-annealed LAO/STO heterostructures showed T independent behaviour [121]. Considering that our sample is oxygen-annealed, observation of T independent n_s at moderate V_G is expected. Such observation is also seen in liquid-gated metallic 3uc LAO/STO even if V_G is as high as 3.0 V [179]. However, in our results, the carrier freeze-out effect is observed at $V_G \geq 1.5$ V. The

freeze-out effect could be attributed to the oxygen vacancies, and has been observed in oxygen-deficient STO films [193], amorphous LAO/STO [121] and unannealed crystalline LAO/STO heterostructures which were directly cooled down to room T in the deposition P_{O2} after growth [98, 121, 194]. This probably suggests that oxygen vacancies at the interface are induced by electric field effect at high V_G. Oxygen vacancies induced by liquid gating have also been demonstrated in VO_2 [22]. Moreover, at high gate voltages, the Hall effect shows nonlinear behaviour at high magnetic field, as is shown in Figure 5.22. This nonlinear Hall effect has also been observed in as-grown LAO/STO interface (unannealed in oxygen) in which oxygen vacancies present [10, 100]. Interestingly, the V_G at which carrier shows freeze-out effect is the same as that at which resistance shows an upturn at low T, suggesting that localization is caused by electric field-induced oxygen vacancies.

In contrast to n_s, as is shown in Figure 5.18(b), μ_H increases with decreasing T at all V_G. For example, at V_G= -0.4 V, μ_H increases from ~24 cm^2/Vs at 180 K to ~6600 cm^2/Vs at 2 K. At high T of 180 K, μ_H exhibits little V_G dependence, changing from 20 cm^2/Vs at V_G=2 V to 24 cm^2/Vs at V_G= -0.4 V. However, at low T, a significant enhancement of μ_H is obtained. For example, at T =2 K, μ_H increases from ~650 cm^2/Vs at V_G=2 V to ~6600 cm^2/Vs at V_G = -0.4 V (see also Figure 5.19(a)).

The R_s-T, n_s -T and μ_H -T curves for the sample without ionic liquid are also plotted in Figure 5.17 and Figure 5.18. One can see that the curves for the sample without ionic liquid and for the sample with ionic liquid but without application of V_G (V_G=0 V) do not coincide with each other. The sample with V_G=0 V show higher R_s at high T but lower R_s at low T, compared with that for sample without ionic liquid. Moreover, the n_s at V_G=0 V is lower and μ_H is higher than those without ionic liquid. These suggest that there is a coupling between the interface and surface which was covered by ionic liquid even without the application of V_G, causing depletion of n_s at the interface, as was shown in section 5.3.2. The interface-surface coupling and the resultant change of electrical transport properties in LAO/STO heterostructures have also been observed by capping polar chemical solvents such as acetone,

ethanol and water on top of LAO surface [182]. In that report, enhancements of n_s and reduction of μ_H were obtained by covering the polar solvents. However, our results show the opposite behaviour with reduction of n_s and enhancement of μ_H. This may be due to the different properties between polar solvents and ionic liquid. Moreover, μ_H can be further enhanced by applying electric field, indicating a new method to search for high-mobility oxide interfaces.

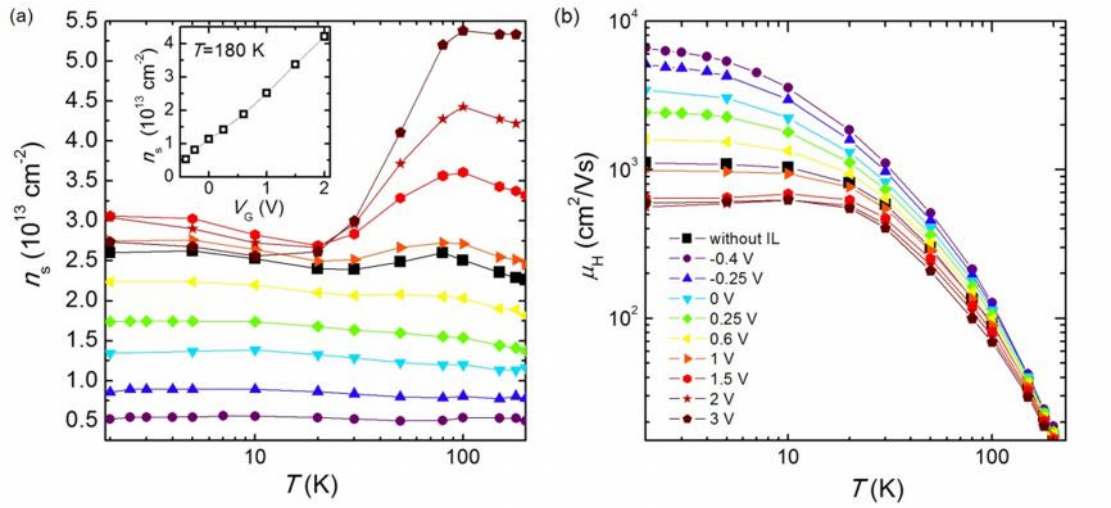

Figure 5.18 The n_s (a) and μ_H (b) as a function of temperature at various V_G. Inset of (a) is the n_s at 180 K as a function of V_G. The black square is the data without IL on top of the sample.

We extract n_s and μ_H at 2 K, and plot them as a function of V_G in Figure 5.19(a). Significant depletion of n_s (from ~3×10^{13} cm^{-2} to ~5×10^{12} cm^{-2}) and enhancement of μ_H (from ~650 cm^2/Vs to ~6600 cm^2/Vs) are obtained by changing V_G from 2 to -0.4 V. Considering that $\mu_H = 1/(e \cdot n_s \cdot R_s)$, where e is the elementary charge, and that R_s does not monotonously decrease with decreasing V_G at low T (Figure 5.17(b)), we are able to attribute enhancement of μ_H to the depletion of n_s. This can be clearly seen in Figure 5.19(b) showing that μ_H increases with decreasing n_s. The data without ionic liquid is also plotted. Compared with the one without ionic liquid, μ_H increases from ~1110 to ~3400 cm^2/Vs after covering ionic liquid, even without applying gate voltage (V_G=0 V). This could be due to the interface-surface coupling, which could deplete n_s, and thus, enhance μ_H, as was discussed above. The highest μ_H is ~6600 cm^2/Vs at negative V_G of -0.4 V, corresponding to the lowest n_s of ~5×10^{12} cm^{-2}. Such

enhancement of mobility by liquid gating is much higher than that in conventional back gating using STO as dielectric (up to ~3600 cm^2/Vs), and top gating using LAO as dielectric (up to ~2000 cm^2/Vs) [10, 99, 175]. Further increasing the negative gate voltage above -0.4 V causes the sample to be unmeasurable, probably due to much lower carrier density.

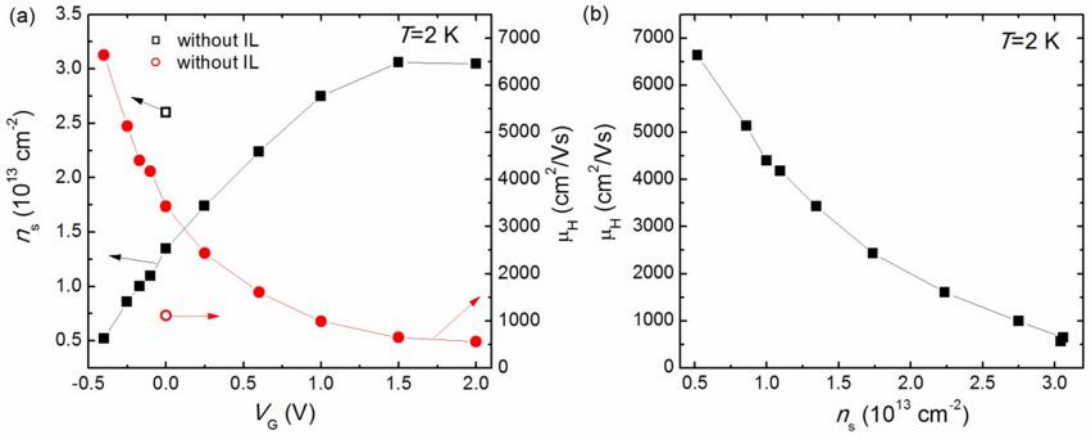

Figure 5.19 (a) The n_s and μ_H as a function of V_G at 2 K. The data for sample without IL is also shown. (b) μ_H as a function of n_s.

5.3.6 Quantum oscillation

Shubnikov-de Hass (SdH) oscillations of conductance in a material arise from the magnetic field dependence of the conduction electron energies. Measurement of SdH oscillations is a powerful method to probe the electronic bandstructure close to the Fermi energy. High mobility, low temperature and high magnetic field are critical to observe SdH oscillations. In LAO/STO system, three-dimensional SdH oscillations have been seen in sample grown at low P_{O2} [117], two-dimensional oscillations have been seen in samples grown and annealed in high P_{O2}, and sample in which $SrCuO_2$ is covered on top of LAO [99-101]. Here, owing to the enhancement of mobility by ionic liquid-assisted field effect, we show SdH oscillations in the LAO/STO interface in which oscillations cannot be seen before liquid gating. Figure 5.20(a) shows the variation of resistance $\Delta R=R(B)-R(0)$ for different gate voltages as a function of magnetic field B oriented perpendicular to the LAO/STO interface, measured at T=2 K. For the sample without ionic liquid, positive magnetoresistance (MR) and no oscillation is observed for magnetic field up to 9 T. After application of ionic liquid, ΔR oscillation is

observed for magnetic field higher than ~4 T even without gate voltage (V_G=0 V), due to the enhancement of mobility (Figure 5.19). ΔR oscillation is also observed at low gate voltage for -0.4 V≤V_G≤ 0 V. Figure 5.20(b) shows numerical derivative of resistance dR/dB as a function of the inverse of magnetic field B^{-1}. One can see that the oscillations are more visible in dR/dB versus B^{-1} plots and the oscillations are periodic in B^{-1}. With decreasing gate voltage and thereby decreasing carrier density, the shift of the main peak of the oscillations is observed, which is similar to the back gating effect [99]. However, the shift here is much clearer since the carrier density is significantly reduced. These results strongly indicate that quantum phenomenon could be obtained by increasing the electron mobility using ionic liquid-assisted field effect.

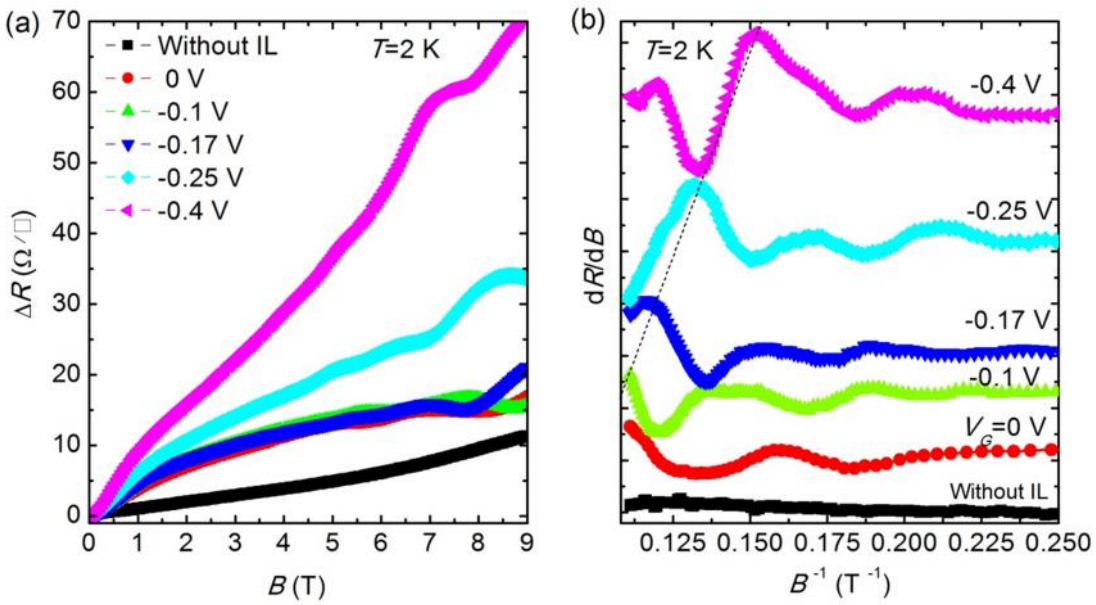

Figure 5.20 Liquid-gated modulation of the Shubnikov-de Hass oscillations. (a) Variation of resistance ΔR=R(B)-R(0) as a function of magnetic field B. (b) Numerical derivative dR/dB as a function of the inverse of magnetic field. The dash line indicates the shift of the main oscillation peak.

Figure 5.21(a) shows the sheet resistance as function of magnetic field at different temperatures. By subtracting a polynomial background for each curve, the amplitude of quantum oscillation is obtained and shown in Figure 5.21(b). One can see that the amplitude

decreases with increasing temperature. The oscillation amplitude ΔR as a function of temperature can be described by the relation

$$\Delta R(T) = 4R_0 e^{-\sim T_D} \sim T / \sinh(\sim T) \qquad \text{Equation (5-1)}$$

where $\sim = 2\pi^2 k_B / \hbar\mu_c$, $\mu_c = eB/m^*$, k_B is the Boltzmann constant, $\hbar$ is the Planck constant, μ_c is the cyclotron frequency, e is the elementary charge, B is the magnetic field, m^* is the carrier effective mass, R_0 is the non-oscillatory component of the sheet resistance, and T_D is the Dingle temperature. We extracted ΔR at B=8.25 T (the peak at B^{-1}=0.121 T^{-1}) and plotted it as a function of temperature in Figure 5.21(c). The fitting of these data by using equation (5-1) gives the value of α. From the definition of α, we can obtain the effective mass m^*=0.99 m_e, where m_e is free electron mass. The value of m^* observed here is slightly smaller than those in previous report [99, 100].

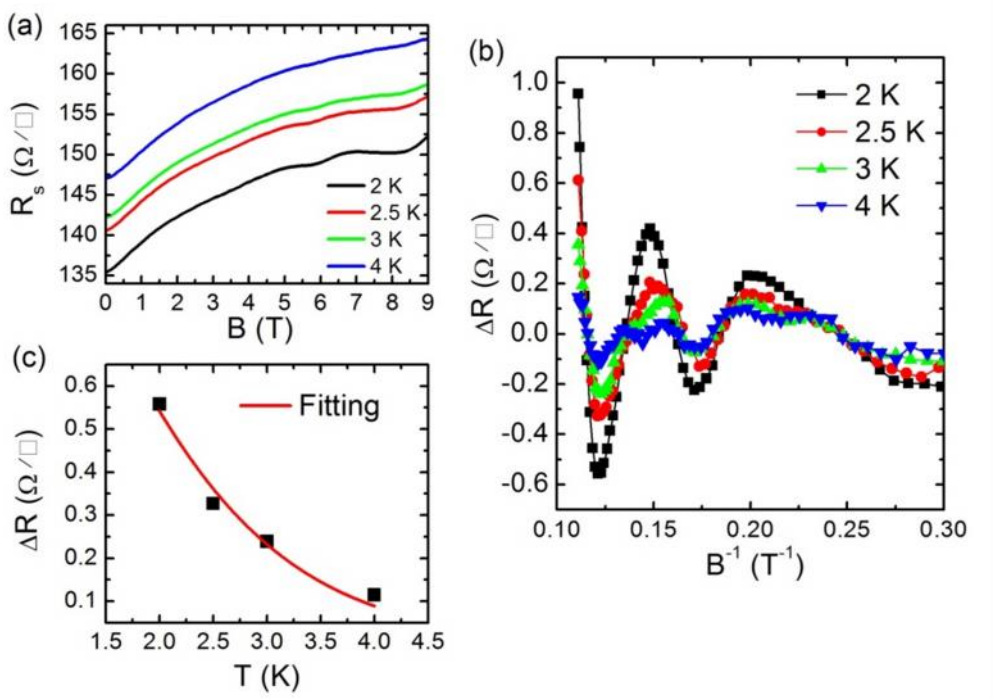

Figure 5.21 Temperature dependence of the SdH oscillations at V_G=0 V. (a) Sheet resistance as a function of magnetic field for different temperatures. (b) Oscillatory component of the sheet resistance as a function of the inverse of magnetic field. (c) The amplitude of the oscillation at B=8.25 T as a function of temperature. The black squares are the experimental data and the red curve is the fitting line.

Figure 5.22 shows the Hall resistance R_H as a function of magnetic field for various gate voltages, measured at T=2 K. Perfect linear Hall effect is observed except at high gate voltage above 1.5 V. Nonlinear Hall effect is observed at V_G=2 and 3 V, probably suggesting multiple conducting carriers induced by field effect at high gate voltages [10, 100, 195, 196]. At V_G= -0.4 V which corresponds to the lowest carrier density and highest mobility, the Hall resistance shows a slight anomaly at B≈7.5 T. This anomaly is at the point where the MR shows a dip (Figure 5.20(a)). Further experiment with higher magnetic fields and lower temperature would be helpful to reveal possible quantum transport properties.

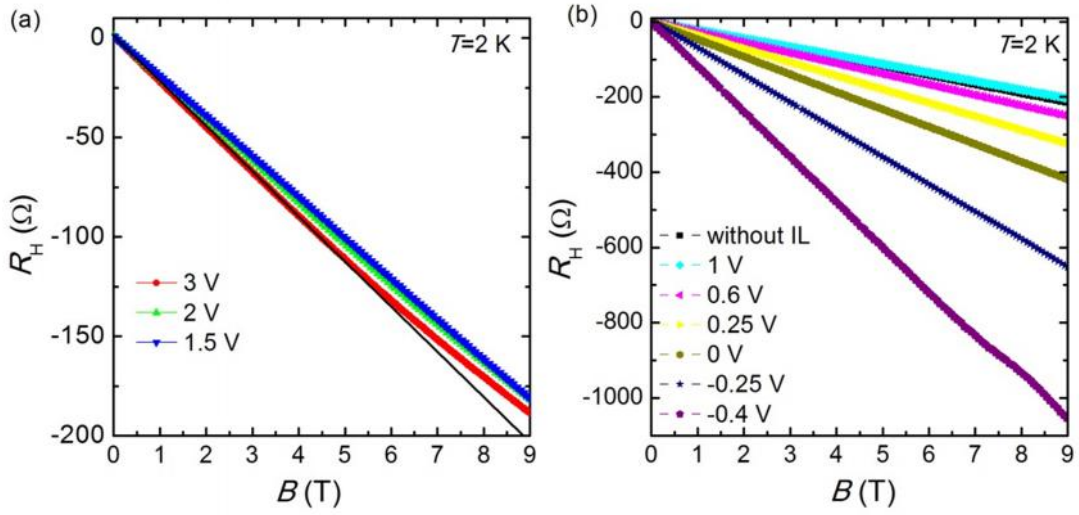

Figure 5.22 Hall resistance R_H as a function of magnetic field B for V_G from 3 to -1.5 V (a) and from 1 to -0.4 V (b). The black line in (a) is guide for eye, to indicate nonlinear Hall effect. The black square is the data without ionic liquid on top of the sample.

5.4 Summary

We demonstrated the modulation of electrical transport properties in patterned LAO/STO interface by electric field effect. Using conventional lithography and depositing amorphous AlN as the hard mask, LAO/STO Hall-bar devices were patterned. The patterned and unpatterned samples showed comparable transport properties, suggesting that clean interface

was preserved after patterning process. Two patterned devices showed remarkable similar values of R_s, n_s and μ_H, evidencing that the patterning of devices are reproducible.

Using the patterned device, we performed the ionic liquid-assisted field effect on LAO/STO 2DEG. The conducting state of the interface was changed after covering ionic liquid even without application of gate voltage, due to the interface-surface coupling caused by the polar nature of LAO layer. By scanning gate voltages between 2 V and -0.8 V, it was found that the resistance increased with decreasing gate voltage, and the initially metallic sample was tuned into as insulating phase at $V_G \approx$ -0.6V. Reversible on-off resistance states with a ratio of ~10^4 could be switched between gate voltages of -2 and 2 V. I_{DS}-V_{DS} curves at different gate voltages were collected. It was found that pinch-off behaviour with saturation of I_{DS} at high V_{DS} was observed in I_{DS}-V_{DS} curve for -0.2 V$\leq V_G \leq$2 V, indicating field-effect transistor operation in LAO/STO 2DEG. This gating-induced metal-insulator transition could be a step to further understand the origin of conducting LAO/STO and explore potential application.

Sheet resistance, carrier density and mobility as a function of temperature were measured. Resistance monotonically increased with decreasing gate voltage at high temperature regime, but did not show monotonic behaviour at low temperature. The carrier density was reduced, and therefore, mobility was enhanced at low gate voltage. The highest mobility is ~6600 cm^2/Vs obtained at negative V_G of -0.4 V. Due to the higher mobility, we observed Shubnikov-de Hass oscillations of the conductance which was not seen in the sample before liquid gating. These results indicate that quantum phenomena could be induced by increasing the electron mobility using ionic liquid-assisted field effect.

Chapter 6 Summary and future directions

6.1 Summary

6.1.1 Ambipolar conductivity in YBCO system

By doping La and modifying the oxygen composition in $YBa_2Cu_3O_y$ system, we obtained ambipolar cuprate $Y_{0.38}La_{0.62}(Ba_{2-x}La_x)Cu_3O_y$ thin films in which both electrons and holes can be doped into a single parent Mott insulator. The samples could be tuned from hole-doped superconductors to electron-doped metals. The electron-doped $Y_{0.38}La_{0.62}(Ba_{1.64}La_{0.36})Cu_3O_y$ thin films showed transport properties similar to underdoped n-type NCCO, such as the quadratic *T* dependence on resistivity at moderate *T* and resistivity anomaly at higher *T*. These phenomena were not observed in hole-doped samples, suggesting *n-p* asymmetry in YBCO system. At the optimally reduced condition, the $Y_{0.38}La_{0.62}(Ba_{1.64}La_{0.36})Cu_3O_y$ thin film showed an electron density of ~2.8×10^{21} cm^{-3} which is, to the best of our knowledge, the highest carrier density in electron-doped YBCO system [135-137]. Comparing the electron density to the underdoped n-type PCCO, it is suggested that our samples are at the very edge of the superconducting dome [49, 61]. $Y_{0.38}La_{0.62}(Ba_{2-x}La_x)Cu_3O_y$ thin films with higher La substitution for Ba were also synthesized. Unexpectedly, the n-type samples with higher La doping levels showed lower electron density, which could probably be attributed to the charge compensation caused by an increase in the oxygen content [132]. This suggests that a balance between the La composition and the achievable lowest oxygen composition is critical to obtain high electron density in YBCO system. Moreover, owing to the high valence state ($>3^+$) of Pr ion, electron doping and metallic behaviour were also seen in $Pr(Ba_{2-x}Pr_x)Cu_3O_y$ thin films. The present work could be a significant step toward ambipolar superconductivity in YBCO system.

6.1.2 Superconductor-insulator transition in electron-doped PCCO

Using ionic liquid-assisted electric field effect and magnetic field, 2D-SITs in electron-doped PCCO ultrathin film were induced. Finite-size scaling analysis indicates that SITs induced both by electric and magnetic field are 2D-QPTs, and the transitions are governed by percolation effects - quantum mechanical in the former and classical in the latter case. Compared to the hole-doped cuprates the SITs in electron-doped system occur at an R_c much lower than R_Q=6.45 kΩ. These suggest that there are amplitude fluctuations associated with the 2D-SITs in electron-doped cuprates, which cause the formation of fermionic excitations at the insulating phase, as opposed to the preservation of bosons which is suggested in hole-doped cuprates [23, 24]. Moreover, in electron-doped cuprates, whether there is still electron pairing as the superconductivity is suppressed by lowering the doping level and increasing the magnetic field to be higher than H_{c2} is still under debate [45-48]. The observations here seem to suggest the unpaired state of electrons in the insulating phase. The present results could help to further our understanding of electron-hole asymmetry in SITs and the pairing states at the edge of criticality in cuprates.

6.1.3 Field effect in LAO/STO interface

Using ionic liquid-assisted electric field effect, the electrical transport properties in patterned LAO/STO interface were modulated. The conducting state of the interface was changed after covering ionic liquid even without application of a gate voltage, suggesting the interface-surface coupling caused by the polar nature of LAO layer. By applying gate voltages, reversible transitions between metallic and insulating phases were observed, indicating that the carrier in the interface could be reversibly accumulated and depleted. We also obtained field-effect transistor operation in LAO/STO 2DEG with different pinch-off voltage V_P at different gate voltages. Moreover, enhancement of mobility was obtained through depleting the carrier density at low gate voltage. Due to the higher mobility, we observed Shubnikov-de Hass oscillations of the conductance which was not seen in the sample before liquid gating.

These results suggest that ionic liquid-assisted field effect could be an important avenue to further understand the origin of conducting LAO/STO, and to explore quantum phenomena and potential applications.

6.2 Future directions

We have shown that our n-type La-doped YBCO thin films exhibit high carrier density and are at the very edge of the superconducting dome. In order to obtain superconductivity higher electron doping is required. However, through further chemical doping, i.e. higher La substitution for Ba, higher electron density has not been obtained, which could probably be due to the charge compensation caused by an increase of oxygen content. From the liquid gating experiment on electron-doped PCCO, the sample could be tuned from initially insulating (underdoped) to superconducting states (slightly overdoped). One can expect that higher electron doping into superconducting dome can be realized by liquid gating. However, for YBCO system, ultrathin films are very sensitive and react with most chemicals [24]. We found that the initially conducting samples were insulating after device process, suggesting degradation of thin films. Therefore, more stable ultrathin films and a robust device fabrication process are critical for ionic liquid-assisted field effect on n-type YBCO system.

We have shown that carrier-tuned and *B*-tuned SITs in PCCO are 2D-QPTs and the transitions are governed by percolation effects. However, under different tuning parameters, the percolations show different behaviours in the same sample, quantum mechanical in carrier-tuned SIT and classical in *B*-tuned SIT. Further investigation of the crossover between these two effects by measuring the carrier-tuned SITs under various magnetic fields may help to reveal the underlying mechanism. The gating effect observed here was performed on 1-uc PCCO grown on undoped PCO. To further demonstrate the efficiency of ionic liquid gating effect, it is interesting to induce superconductivity from the undoped PCO. Furthermore, oxygen reduction is necessary to obtain superconductivity in electron-doped cuprates. The SIT in PCCO here was performed in samples annealed in vacuum. We also demonstrated that

ionic liquid gating predominantly induced charge carriers at the surface of PCCO as opposed to inducing oxygen vacancies. Therefore, it is interesting to perform liquid gating and induce superconductivity in PCCO samples which are free from oxygen vacancies (annealed in oxygen). This would help to further our understanding of the role of oxygen vacancies in electron-doped cuprate superconductors.

We have shown that the mobility of LAO/STO 2DEG could be enhanced through ionic liquid gating. For a device with $\mu_H \approx 1110$ cm^2/Vs before applying ionic liquid, higher $\mu_H \approx 6600$ cm^2/Vs was obtained and Shubnikov-de Hass oscillations were observed. Further increasing the mobility is critical to reveal other quantum phenomena such as quantum Hall effect. It has been shown that high mobility of ~5000 cm^2/Vs in LAO/STO interface could be obtained by improving the crystalline quality [99]. Therefore, it is interesting to improve the interface quality and perform ionic liquid gating on this initially high-mobility interface.

Bibliography

[1] S.M. Sze, K.K. Ng, Physics of Semiconductor Devices, Wiley, (2007).

[2] N. Plakida, High-Temperature Cuprate Superconductors, Springer, (2010).

[3] Y. Tokura, Critical features of colossal magnetoresistive manganites, Reports on Progress in Physics, 69 (2006) 797-851.

[4] M.B. Salamon, M. Jaime, The physics of manganites: Structure and transport, Rev. Mod. Phys., 73 (2001) 583-628.

[5] C.H. Ahn, J.M. Triscone, J. Mannhart, Electric field effect in correlated oxide systems, Nature, 424 (2003) 1015-1018.

[6] C.H. Ahn, A. Bhattacharya, M. Di Ventra, J.N. Eckstein, C.D. Frisbie, M.E. Gershenson, A.M. Goldman, I.H. Inoue, J. Mannhart, A.J. Millis, A.F. Morpurgo, D. Natelson, J.M. Triscone, Electrostatic modification of novel materials, Rev. Mod. Phys., 78 (2006) 1185-1212.

[7] J. Mannhart, High-T-c transistors, Supercond. Sci. Technol., 9 (1996) 49-67.

[8] S. Mathews, R. Ramesh, T. Venkatesan, J. Benedetto, Ferroelectric field effect transistor based on epitaxial perovskite heterostructures, Science, 276 (1997) 238-240.

[9] A.D. Caviglia, S. Gariglio, N. Reyren, D. Jaccard, T. Schneider, M. Gabay, S. Thiel, G. Hammerl, J. Mannhart, J.M. Triscone, Electric field control of the LaAlO3/SrTiO3 interface ground state, Nature, 456 (2008) 624-627.

[10] C. Bell, S. Harashima, Y. Kozuka, M. Kim, B.G. Kim, Y. Hikita, H.Y. Hwang, Dominant Mobility Modulation by the Electric Field Effect at the LaAlO3/SrTiO3 Interface, Phys. Rev. Lett., 103 (2009) 226802.

[11] A. Tsukazaki, S. Akasaka, K. Nakahara, Y. Ohno, H. Ohno, D. Maryenko, A. Ohtomo, M. Kawasaki, Observation of the fractional quantum Hall effect in an oxide, Nature Materials, 9 (2010) 889-893.

[12] H. Shimotani, H. Asanuma, A. Tsukazaki, A. Ohtomo, M. Kawasaki, Y. Iwasa, Insulator-to-metal transition in ZnO by electric double layer gating, Applied Physics Letters, 91 (2007) 082106.

[13] H.T. Yuan, H. Shimotani, A. Tsukazaki, A. Ohtomo, M. Kawasaki, Y. Iwasa, High-Density Carrier Accumulation in ZnO Field-Effect Transistors Gated by Electric Double Layers of Ionic Liquids, Advanced Functional Materials, 19 (2009) 1046-1053.

[14] K. Ueno, S. Nakamura, H. Shimotani, A. Ohtomo, N. Kimura, T. Nojima, H. Aoki, Y. Iwasa, M. Kawasaki, Electric-field-induced superconductivity in an insulator, Nature Materials, 7 (2008) 855-858.

[15] J.T. Ye, S. Inoue, K. Kobayashi, Y. Kasahara, H.T. Yuan, H. Shimotani, Y. Iwasa, Liquid-gated interface superconductivity on an atomically flat film, Nature Materials, 9 (2010) 125-128.

[16] K. Ueno, S. Nakamura, H. Shimotani, H.T. Yuan, N. Kimura, T. Nojima, H. Aoki, Y. Iwasa, M. Kawasaki, Discovery of superconductivity in KTaO3 by electrostatic carrier doping, Nat. Nanotechnol., 6 (2011) 408-412.

[17] J.T. Ye, Y.J. Zhang, R. Akashi, M.S. Bahramy, R. Arita, Y. Iwasa, Superconducting Dome in a Gate-Tuned Band Insulator, Science, 338 (2012) 1193-1196.

[18] Y. Yamada, K. Ueno, T. Fukumura, H.T. Yuan, H. Shimotani, Y. Iwasa, L. Gu, S. Tsukimoto, Y. Ikuhara, M. Kawasaki, Electrically Induced Ferromagnetism at Room Temperature in Cobalt-Doped Titanium Dioxide, Science, 332 (2011) 1065-1067.

[19] A.S. Dhoot, C. Israel, X. Moya, N.D. Mathur, R.H. Friend, Large Electric Field Effect in Electrolyte-Gated Manganites, Phys. Rev. Lett., 102 (2009) 136402.

[20] T. Hatano, Y. Ogimoto, N. Ogawa, M. Nakano, S. Ono, Y. Tomioka, K. Miyano, Y. Iwasa, Y. Tokura, Gate Control of Electronic Phases in a Quarter-Filled Manganite, Scientific Reports, 3 (2013) 1-5.

[21] M. Nakano, K. Shibuya, D. Okuyama, T. Hatano, S. Ono, M. Kawasaki, Y. Iwasa, Y. Tokura, Collective bulk carrier delocalization driven by electrostatic surface charge accumulation, Nature, 487 (2012) 459-462.

[22] J. Jeong, N. Aetukuri, T. Graf, T.D. Schladt, M.G. Samant, S.S.P. Parkin, Suppression of Metal-Insulator Transition in VO2 by Electric Field-Induced Oxygen Vacancy Formation, Science, 339 (2013) 1402-1405.

[23] A.T. Bollinger, G. Dubuis, J. Yoon, D. Pavuna, J. Misewich, I. Bozovic, Superconductor-insulator transition in La2-xSrxCuO4 at the pair quantum resistance, Nature, 472 (2011) 458-460.

[24] X. Leng, J. Garcia-Barriocanal, S. Bose, Y. Lee, A.M. Goldman, Electrostatic Control of the Evolution from a Superconducting Phase to an Insulating Phase in Ultrathin YBa2CaCu3O7-x Films, Phys. Rev. Lett., 107 (2011) 027001.

[25] X. Leng, J. Garcia-Barriocanal, B.Y. Yang, Y. Lee, J. Kinney, A.M. Goldman, Indications of an Electronic Phase Transition in Two-Dimensional Superconducting YBa2Cu3O7-x Thin Films Induced by Electrostatic Doping, Phys. Rev. Lett., 108 (2012) 067004.

[26] J. Garcia-Barriocanal, A. Kobrinskii, X. Leng, J. Kinney, B. Yang, S. Snyder, A.M. Goldman, Electronically driven superconductor-insulator transition in electrostatically doped La2CuO4+delta thin films, Phys. Rev. B, 87 (2013) 024509.

[27] J.G. Bednorz, K.A. Muller, POSSIBLE HIGH-TC SUPERCONDUCTIVITY IN THE BA-LA-CU-O SYSTEM, Z. Phys. B-Condens. Mat., 64 (1986) 189-193.

[28] M.K. Wu, J.R. Ashburn, C.J. Torng, P.H. Hor, R.L. Meng, L. Gao, Z.J. Huang, Y.Q. Wang, C.W. Chu, SUPERCONDUCTIVITY AT 93-K IN A NEW MIXED-PHASE Y-BA-CU-O COMPOUND SYSTEM AT AMBIENT PRESSURE, Phys. Rev. Lett., 58 (1987) 908-910.

[29] L. Gao, Y.Y. Xue, F. Chen, Q. Xiong, R.L. Meng, D. Ramirez, C.W. Chu, J.H. Eggert, H.K. Mao, SUPERCONDUCTIVITY UP TO 164-K IN HGBA2CAM-1CUMO2M+2+DELTA (M=1,2, AND 3) UNDER QUASI-HYDROSTATIC PRESSURES, Phys. Rev. B, 50 (1994) 4260-4263.

[30] J.D. Jorgensen, B.W. Veal, A.P. Paulikas, L.J. Nowicki, G.W. Crabtree, H. Claus, W.K. Kwok, STRUCTURAL-PROPERTIES OF OXYGEN-DEFICIENT YBA2CU3O7-DELTA, Phys. Rev. B, 41 (1990) 1863-1877.

[31] R.J. Cava, A.W. Hewat, E.A. Hewat, B. Batlogg, M. Marezio, K.M. Rabe, J.J. Krajewski, W.F. Peck, L.W. Rupp, STRUCTURAL ANOMALIES, OXYGEN ORDERING AND SUPERCONDUCTIVITY IN OXYGEN DEFICIENT BA2YCU3OX, Physica C, 165 (1990) 419-433.

[32] J.M. Tranquada, A.H. Moudden, A.I. Goldman, P. Zolliker, D.E. Cox, G. Shirane, S.K. Sinha, D. Vaknin, D.C. Johnston, M.S. Alvarez, A.J. Jacobson, J.T. Lewandowski, J.M. Newsam, ANTIFERROMAGNETISM IN YBA2CU3O6+X, Phys. Rev. B, 38 (1988) 2477-2485.

[33] Y. Tokura, H. Takagi, S. Uchida, A SUPERCONDUCTING COPPER-OXIDE COMPOUND WITH ELECTRONS AS THE CHARGE-CARRIERS, Nature, 337 (1989) 345-347.

[34] H. Takagi, S. Uchida, Y. Tokura, SUPERCONDUCTIVITY PRODUCED BY ELECTRON DOPING IN CUO2-LAYERED COMPOUNDS, Phys. Rev. Lett., 62 (1989) 1197-1200.

[35] J.B. Torrance, Y. Tokura, A.I. Nazzal, A. Bezinge, T.C. Huang, S.S.P. Parkin, ANOMALOUS DISAPPEARANCE OF HIGH-TC SUPERCONDUCTIVITY AT HIGH HOLE CONCENTRATION IN METALLIC LA2-XSRXCUO4, Phys. Rev. Lett., 61 (1988) 1127-1130.

[36] H. Takagi, T. Ido, S. Ishibashi, M. Uota, S. Uchida, Y. Tokura, SUPERCONDUCTOR-TO-NONSUPERCONDUCTOR TRANSITION IN (LA1-XSRX)2CUO4 AS INVESTIGATED BY TRANSPORT AND MAGNETIC MEASUREMENTS, Phys. Rev. B, 40 (1989) 2254-2261.

[37] Y. Krockenberger, J. Kurian, A. Winkler, A. Tsukada, M. Naito, L. Alff, Superconductivity phase diagrams for the electron-doped cuprates R(2-x)Ce(x)CuO(4) (R=La, Pr, Nd, Sm, and Eu), Phys. Rev. B, 77 (2008) 060505.

[38] M.G. Smith, A. Manthiram, J. Zhou, J.B. Goodenough, J.T. Markert, ELECTRON-DOPED SUPERCONDUCTIVITY AT 40-K IN THE INFINITE-LAYER COMPOUND SR1-YNDYCUO2, Nature, 351 (1991) 549-551.

[39] S. Karimoto, K. Ueda, M. Naito, T. Imai, Single-crystalline superconducting thin films of electron-doped infinite-layer compounds grown by molecular-beam epitaxy, Applied Physics Letters, 79 (2001) 2767-2769.

[40] A. Damascelli, Z. Hussain, Z.X. Shen, Angle-resolved photoemission studies of the cuprate superconductors, Rev. Mod. Phys., 75 (2003) 473-541.

[41] T. Timusk, B. Statt, The pseudogap in high-temperature superconductors: an experimental survey, Reports on Progress in Physics, 62 (1999) 61-122.

[42] S. Hufner, M.A. Hossain, A. Damascelli, G.A. Sawatzky, Two gaps make a high-temperature superconductor?, Reports on Progress in Physics, 71 (2008) 062501.

[43] O. Fischer, M. Kugler, I. Maggio-Aprile, C. Berthod, C. Renner, Scanning tunneling spectroscopy of high-temperature superconductors, Rev. Mod. Phys., 79 (2007) 353-419.

[44] M.R. Norman, C. Pepin, The electronic nature of high temperature cuprate superconductors, Reports on Progress in Physics, 66 (2003) 1547-1610.

[45] S. Kleefisch, B. Welter, A. Marx, L. Alff, R. Gross, M. Naito, Possible pseudogap behavior of electron-doped high-temperature superconductors, Phys. Rev. B, 63 (2001) 100507.

[46] A. Biswas, P. Fournier, V.N. Smolyaninova, R.C. Budhani, J.S. Higgins, R.L. Greene, Gapped tunneling spectra in the normal state of Pr2-xCexCuO4, Phys. Rev. B, 64 (2001) 104519.

[47] L. Alff, Y. Krockenberger, B. Welter, M. Schonecke, R. Gross, D. Manske, M. Naito, A hidden pseudogap under the 'dome' of superconductivity in electron-doped high-temperature superconductors, Nature, 422 (2003) 698-701.

[48] Y. Dagan, M.M. Qazilbash, R.L. Greene, Tunneling into the normal state of Pr2-xCexCuO4, Phys. Rev. Lett., 94 (2005) 187003.

[49] N.P. Armitage, P. Fournier, R.L. Greene, Progress and perspectives on electron-doped cuprates, Rev. Mod. Phys., 82 (2010) 2421-2487.

[50] Y. Ando, G.S. Boebinger, A. Passner, L.F. Schneemeyer, T. Kimura, M. Okuya, S. Watauchi, J. Shimoyama, K. Kishio, K. Tamasaku, N. Ichikawa, S. Uchida, Resistive upper critical fields and irreversibility lines of optimally doped high-T-c cuprates, Phys. Rev. B, 60 (1999) 12475-12479.

[51] P. Fournier, R.L. Greene, Doping dependence of the upper critical field of electron-doped Pr(2-x)Ce(x)CuO(4) thin films, Phys. Rev. B, 68 (2003) 094507.

[52] C.C. Tsuei, A. Gupta, G. Koren, QUADRATIC TEMPERATURE-DEPENDENCE OF THE INPLANE RESISTIVITY IN SUPERCONDUCTING ND1.85CUO4 - EVIDENCE FOR FERMI-LIQUID NORMAL STATE, Physica C, 161 (1989) 415-422.

[53] M. Gurvitch, A.T. Fiory, RESISTIVITY OF LA1.825SR0.175CUO4 AND YBA2CU3O7 TO 1100-K - ABSENCE OF SATURATION AND ITS IMPLICATIONS, Phys. Rev. Lett., 59 (1987) 1337-1340.

[54] H. Takagi, B. Batlogg, H.L. Kao, J. Kwo, R.J. Cava, J.J. Krajewski, W.F. Peck, SYSTEMATIC EVOLUTION OF TEMPERATURE-DEPENDENT RESISTIVITY IN LA2-XSRXCUO4, Phys. Rev. Lett., 69 (1992) 2975-2978.

[55] N.P. Armitage, F. Ronning, D.H. Lu, C. Kim, A. Damascelli, K.M. Shen, D.L. Feng, H. Eisaki, Z.X. Shen, P.K. Mang, N. Kaneko, M. Greven, Y. Onose, Y. Taguchi, Y. Tokura, Doping dependence of an n-type cuprate superconductor investigated by angle-resolved photoemission spectroscopy, Phys. Rev. Lett., 88 (2002) 257001.

[56] T. Yoshida, X.J. Zhou, T. Sasagawa, W.L. Yang, P.V. Bogdanov, A. Lanzara, Z. Hussain, T. Mizokawa, A. Fujimori, H. Eisaki, Z.X. Shen, T. Kakeshita, S. Uchida, Metallic behavior of lightly doped La2-xSrxCuO4 with a Fermi surface forming an arc, Phys. Rev. Lett., 91 (2003) 027001.

[57] N. Harima, J. Matsuno, A. Fujimori, Y. Onose, Y. Taguchi, Y. Tokura, Chemical potential shift in Nd2-xCexCuO4: Contrasting behavior between the electron- and hole-doped cuprates, Phys. Rev. B, 64 (2001) 220507.

[58] E. Dagotto, CORRELATED ELECTRONS IN HIGH-TEMPERATURE SUPERCONDUCTORS, Rev. Mod. Phys., 66 (1994) 763-840.

[59] P.A. Lee, N. Nagaosa, X.G. Wen, Doping a Mott insulator: Physics of high-temperature superconductivity, Rev. Mod. Phys., 78 (2006) 17-85.

[60] S.C. Zhang, A unified theory based on SO(5) symmetry of superconductivity and antiferromagnetism, Science, 275 (1997) 1089-1096.

[61] Y. Dagan, M.M. Qazilbash, C.P. Hill, V.N. Kulkarni, R.L. Greene, Evidence for a quantum phase transition in Pr2-xCexCuO4-delta from transport measurements, Phys. Rev. Lett., 92 (2004) 167001.

[62] P.C. Li, K. Behnia, R.L. Greene, Evidence for a quantum phase transition in electron-doped Pr2-xCexCuO4-delta from thermopower measurements, Phys. Rev. B, 75 (2007) 020506.

[63] F.F. Balakirev, J.B. Betts, A. Migliori, I. Tsukada, Y. Ando, G.S. Boebinger, Quantum Phase Transition in the Magnetic-Field-Induced Normal State of Optimum-Doped High-T-c Cuprate Superconductors at Low Temperatures, Phys. Rev. Lett., 102 (2009) 017004.

[64] S.L. Sondhi, S.M. Girvin, J.P. Carini, D. Shahar, Continuous quantum phase transitions, Rev. Mod. Phys., 69 (1997) 315-333.

[65] V.F. Gantmakher, V.T. Dolgopolov, Superconductor-insulator quantum phase transition, Physics-Uspekhi, 53 (2010) 1-49.

[66] M.P.A. Fisher, QUANTUM PHASE-TRANSITIONS IN DISORDERED 2-DIMENSIONAL SUPERCONDUCTORS, Phys. Rev. Lett., 65 (1990) 923-926.

[67] A. Yazdani, A. Kapitulnik, SUPERCONDUCTING-INSULATING TRANSITION IN 2-DIMENSIONAL ALPHA-MOGE THIN-FILMS, Phys. Rev. Lett., 74 (1995) 3037-3040.

[68] K.A. Parendo, K.H. Sarwa, B. Tan, A. Bhattacharya, M. Eblen-Zayas, N.E. Staley, A.M. Goldman, Electrostatic tuning of the superconductor-insulator transition in two dimensions, Phys. Rev. Lett., 94 (2005) 197004.

[69] A.M. Goldman, N. Markovic, Superconductor-insulator transitions in the two-dimensional limit, Physics Today, 51 (1998) 39-44.

[70] D.B. Haviland, Y. Liu, A.M. Goldman, ONSET OF SUPERCONDUCTIVITY IN THE TWO-DIMENSIONAL LIMIT, Phys. Rev. Lett., 62 (1989) 2180-2183.

[71] Y. Liu, K.A. McGreer, B. Nease, D.B. Haviland, G. Martinez, J.W. Halley, A.M. Goldman, SCALING OF THE INSULATOR-TO-SUPERCONDUCTOR TRANSITION IN ULTRATHIN AMORPHOUS BI FILMS, Phys. Rev. Lett., 67 (1991) 2068-2071.

[72] Y. Liu, D.B. Haviland, B. Nease, A.M. Goldman, INSULATOR-TO-SUPERCONDUCTOR TRANSITION IN ULTRATHIN FILMS, Phys. Rev. B, 47 (1993) 5931-5946.

[73] S.J. Lee, J.B. Ketterson, CRITICAL SHEET RESISTANCE FOR THE SUPPRESSION OF SUPERCONDUCTIVITY IN THIN MO-C FILMS, Phys. Rev. Lett., 64 (1990) 3078-3081.

[74] R. Schneider, A.G. Zaitsev, D. Fuchs, H. von Lohneysen, Superconductor-Insulator Quantum Phase Transition in Disordered FeSe Thin Films, Phys. Rev. Lett., 108 (2012) 257003.

[75] S. Tanda, S. Ohzeki, T. Nakayama, BOSE-GLASS VORTEX-GLASS PHASE-TRANSITION AND DYNAMIC SCALING FOR HIGH-T(C) ND2-XCEXCUO4 THIN-FILMS, Phys. Rev. Lett., 69 (1992) 530-533.

[76] G.T. Seidler, T.F. Rosenbaum, B.W. Veal, 2-DIMENSIONAL SUPERCONDUCTOR-INSULATOR TRANSITION IN BULK SINGLE-CRYSTAL YBA2CU3O6.38, Phys. Rev. B, 45 (1992) 10162-10164.

[77] K. Karpinska, A. Malinowski, M.Z. Cieplak, S. Guha, S. Gershman, G. Kotliar, T. Skoskiewicz, W. Plesiewicz, M. Berkowski, P. Lindenfeld, Magnetic-field induced superconductor-insulator transition in the La2-xSrxCuO4 system, Phys. Rev. Lett., 77 (1996) 3033-3036.

[78] M. Steiner, A. Kapitulnik, Superconductivity in the insulating phase above the field-tuned superconductor-insulator transition in disordered indium oxide films, Physica C-Superconductivity and Its Applications, 422 (2005) 16-26.

[79] M.A. Steiner, N.P. Breznay, A. Kapitulnik, Approach to a superconductor-to-Bose-insulator transition in disordered films, Phys. Rev. B, 77 (2008) 212501.

[80] A.F. Hebard, M.A. Paalanen, MAGNETIC-FIELD-TUNED SUPERCONDUCTOR-INSULATOR TRANSITION IN 2-DIMENSIONAL FILMS, Phys. Rev. Lett., 65 (1990) 927-930.

[81] M. Ovadia, D. Kalok, B. Sacepe, D. Shahar, Duality symmetry and its breakdown in the vicinity of the superconductor-insulator transition, Nature Physics, 9 (2013) 415-418.

[82] S.Y. Hsu, J.M. Valles, MAGNETIC-FIELD-INDUCED PAIR-BREAKING EFFECTS IN GRANULAR PB FILMS NEAR THE SUPERCONDUCTOR-TO-INSULATOR TRANSITION, Phys. Rev. B, 48 (1993) 4164-4167.

[83] N. Mason, A. Kapitulnik, Dissipation effects on the superconductor-insulator transition in 2D superconductors, Phys. Rev. Lett., 82 (1999) 5341-5344.

[84] F.W. Lytle, X-RAY DIFFRACTOMETRY OF LOW-TEMPERATURE PHASE TRANSFORMATIONS IN STRONTIUM TITANATE, J. Appl. Phys., 35 (1964) 2212.

[85] E. Tosatti, R. Martonak, ROTATIONAL MELTING IN DISPLACIVE QUANTUM PARAELECTRICS, Solid State Communications, 92 (1994) 167-180.

[86] S.K. Mishra, D. Pandey, Low temperature x-ray diffraction study of the phase transitions in Sr1-xCaxTiO3 (x=0.02, 0.04): Evidence for ferrielectric ordering, Applied Physics Letters, 95 (2009) 232910.

[87] K.A. Muller, H. Burkard, SRTIO3 - INTRINSIC QUANTUM PARA-ELECTRIC BELOW 4-K, Phys. Rev. B, 19 (1979) 3593-3602.

[88] R.L. Wild, E.M. Rockar, J.C. Smith, THERMOCHROMISM AND ELECTRICAL CONDUCTIVITY IN DOPED SRTIO3, Phys. Rev. B, 8 (1973) 3828-3835.

[89] C. Lee, J. Destry, J.L. Brebner, OPTICAL-ABSORPTION AND TRANSPORT IN SEMICONDUCTING SRTIO3, Phys. Rev. B, 11 (1975) 2299-2310.

[90] H. Yamada, G.R. Miller, POINT-DEFECTS IN REDUCED STRONTIUM-TITANATE, J. Solid State Chem., 6 (1973) 169-177.

[91] J.F. Schooley, W.R. Hosler, M.L. Cohen, SUPERCONDUCTIVITY IN SEMICONDUCTING SRTIO3, Phys. Rev. Lett., 12 (1964) 474.

[92] J. Chrosch, E.K.H. Salje, Temperature dependence of the domain wall width in LaAlO3, J. Appl. Phys., 85 (1999) 722-727.

[93] S.A. Hayward, S.A.T. Redfern, E.K.H. Salje, Order parameter saturation in LaAlO(3), J. Phys.-Condes. Matter, 14 (2002) 10131-10144.

[94] A. Ohtomo, H.Y. Hwang, A high-mobility electron gas at the LaAlO3/SrTiO3 heterointerface, Nature, 427 (2004) 423-426.

[95] S. Thiel, G. Hammerl, A. Schmehl, C.W. Schneider, J. Mannhart, Tunable quasi-two-dimensional electron gases in oxide heterostructures, Science, 313 (2006) 1942-1945.

[96] N. Reyren, S. Thiel, A.D. Caviglia, L.F. Kourkoutis, G. Hammerl, C. Richter, C.W. Schneider, T. Kopp, A.S. Ruetschi, D. Jaccard, M. Gabay, D.A. Muller, J.M. Triscone, J. Mannhart, Superconducting interfaces between insulating oxides, Science, 317 (2007) 1196-1199.

[97] A. Brinkman, M. Huijben, M. Van Zalk, J. Huijben, U. Zeitler, J.C. Maan, W.G. Van der Wiel, G. Rijnders, D.H.A. Blank, H. Hilgenkamp, Magnetic effects at the interface between non-magnetic oxides, Nature Materials, 6 (2007) 493-496.

[98] Ariando, X. Wang, G. Baskaran, Z.Q. Liu, J. Huijben, J.B. Yi, A. Annadi, A.R. Barman, A. Rusydi, S. Dhar, Y.P. Feng, J. Ding, H. Hilgenkamp, T. Venkatesan, Electronic phase separation at the LaAlO3/SrTiO3 interface, Nature Communications, 2 (2011) 1038.

[99] A.D. Caviglia, S. Gariglio, C. Cancellieri, B. Sacepe, A. Fete, N. Reyren, M. Gabay, A.F. Morpurgo, J.M. Triscone, Two-Dimensional Quantum Oscillations of the Conductance at LaAlO3/SrTiO3 Interfaces, Phys. Rev. Lett., 105 (2010) 236802.

[100] M. Ben Shalom, A. Ron, A. Palevski, Y. Dagan, Shubnikov-De Haas Oscillations in SrTiO3/LaAlO3 Interface, Phys. Rev. Lett., 105 (2010) 206401.

[101] A. McCollam, S. Wenderich, M.K. Kruize, V.K. Guduru, H.J.A. Molegraaf, M. Huijben, G. Koster, D.H.A. Blank, G. Rijnders, A. Brinkman, H. Hilgenkamp, U. Zeitler, J.C. Maan, Quantum oscillations and subband properties of the two-dimensional electron gas at the LaAlO3/SrTiO3 interface, Apl Materials, 2 (2014) 022102.

[102] A.D. Caviglia, M. Gabay, S. Gariglio, N. Reyren, C. Cancellieri, J.M. Triscone, Tunable Rashba Spin-Orbit Interaction at Oxide Interfaces, Phys. Rev. Lett., 104 (2010) 126803.

[103] A. Fete, S. Gariglio, A.D. Caviglia, J.M. Triscone, M. Gabay, Rashba induced magnetoconductance oscillations in the LaAlO3-SrTiO3 heterostructure, Phys. Rev. B, 86 (2012) 201105.

[104] M. Ben Shalom, M. Sachs, D. Rakhmilevitch, A. Palevski, Y. Dagan, Tuning Spin-Orbit Coupling and Superconductivity at the SrTiO3/LaAlO3 Interface: A Magnetotransport Study, Phys. Rev. Lett., 104 (2010) 126802.

[105] D.A. Dikin, M. Mehta, C.W. Bark, C.M. Folkman, C.B. Eom, V. Chandrasekhar, Coexistence of Superconductivity and Ferromagnetism in Two Dimensions, Phys. Rev. Lett., 107 (2011) 056802.

[106] J.A. Bert, B. Kalisky, C. Bell, M. Kim, Y. Hikita, H.Y. Hwang, K.A. Moler, Direct imaging of the coexistence of ferromagnetism and superconductivity at the LaAlO3/SrTiO3 interface, Nature Physics, 7 (2011) 767-771.

[107] L. Li, C. Richter, J. Mannhart, R.C. Ashoori, Coexistence of magnetic order and two-dimensional superconductivity at LaAlO3/SrTiO3 interfaces, Nature Physics, 7 (2011) 762-766.

[108] C. Richter, H. Boschker, W. Dietsche, E. Fillis-Tsirakis, R. Jany, F. Loder, L.F. Kourkoutis, D.A. Muller, J.R. Kirtley, C.W. Schneider, J. Mannhart, Interface superconductor with gap behaviour like a high-temperature superconductor, Nature, 502 (2013) 528-531.

[109] N. Nakagawa, H.Y. Hwang, D.A. Muller, Why some interfaces cannot be sharp, Nature Materials, 5 (2006) 204-209.

[110] Z.S. Popovic, S. Satpathy, R.M. Martin, Origin of the Two-Dimensional Electron Gas Carrier Density at the LaAlO3 on SrTiO3 Interface, Phys. Rev. Lett., 101 (2008) 256801.

[111] A. Annadi, Q. Zhang, X.R. Wang, N. Tuzla, K. Gopinadhan, W.M. Lu, A.R. Barman, Z.Q. Liu, A. Srivastava, S. Saha, Y.L. Zhao, S.W. Zeng, S. Dhar, E. Olsson, B. Gu, S. Yunoki, S. Maekawa, H. Hilgenkamp, T. Venkatesan, Ariando, Anisotropic two-dimensional electron gas at the LaAlO3/SrTiO3 (110) interface, Nature Communications, 4 (2013) 1838.

[112] P.R. Willmott, S.A. Pauli, R. Herger, C.M. Schleputz, D. Martoccia, B.D. Patterson, B. Delley, R. Clarke, D. Kumah, C. Cionca, Y. Yacoby, Structural basis for the conducting interface between LaAlO3 and SrTiO3, Phys. Rev. Lett., 99 (2007) 155502.

[113] V. Vonk, M. Huijben, K.J.I. Driessen, P. Tinnemans, A. Brinkman, S. Harkema, H. Graafsma, Interface structure of SrTiO3/LaAlO3 at elevated temperatures studied in situ by synchrotron x rays, Phys. Rev. B, 75 (2007) 235417.

[114] Z.Q. Liu, Z. Huang, W.M. Lu, K. Gopinadhan, X. Wang, A. Annadi, T. Venkatesan, Ariando, Atomically flat interface between a single-terminated LaAlO3 substrate and SrTiO3 thin film is insulating, Aip Advances, 2 (2012) 012147.

[115] A. Kalabukhov, R. Gunnarsson, J. Borjesson, E. Olsson, T. Claeson, D. Winkler, Effect of oxygen vacancies in the SrTiO3 substrate on the electrical properties of the LaAlO3/SrTiO3 interface, Phys. Rev. B, 75 (2007) 121404.

[116] W. Siemons, G. Koster, H. Yamamoto, W.A. Harrison, G. Lucovsky, T.H. Geballe, D.H.A. Blank, M.R. Beasley, Origin of charge density at LaAlO3 on SrTiO3 heterointerfaces: Possibility of intrinsic doping, Phys. Rev. Lett., 98 (2007) 196802.

[117] G. Herranz, M. Basletic, M. Bibes, C. Carretero, E. Tafra, E. Jacquet, K. Bouzehouane, C. Deranlot, A. Hamzic, J.M. Broto, A. Barthelemy, A. Fert, High mobility in LaAlO3/SrTiO3

heterostructures: Origin, dimensionality, and perspectives, Phys. Rev. Lett., 98 (2007) 216803.

[118] J.N. Eckstein, Oxide interfaces - Watch out for the lack of oxygen, Nature Materials, 6 (2007) 473-474.

[119] Y.Z. Chen, N. Pryds, J.E. Kleibeuker, G. Koster, J.R. Sun, E. Stamate, B.G. Shen, G. Rijnders, S. Linderoth, Metallic and Insulating Interfaces of Amorphous SrTiO3-Based Oxide Heterostructures, Nano Lett., 11 (2011) 3774-3778.

[120] S.W. Lee, Y.Q. Liu, J. Heo, R.G. Gordon, Creation and Control of Two-Dimensional Electron Gas Using Al-Based Amorphous Oxides/SrTiO3 Heterostructures Grown by Atomic Layer Deposition, Nano Lett., 12 (2012) 4775-4783.

[121] Z.Q. Liu, C.J. Li, W.M. Lu, X.H. Huang, Z. Huang, S.W. Zeng, X.P. Qiu, L.S. Huang, A. Annadi, J.S. Chen, J.M.D. Coey, T. Venkatesan, Ariando, Origin of the Two-Dimensional Electron Gas at LaAlO3/SrTiO3 Interfaces: The Role of Oxygen Vacancies and Electronic Reconstruction, Physical Review X, 3 (2013) 021010.

[122] Z.Q. Liu, L. Sun, Z. Huang, C.J. Li, S.W. Zeng, K. Han, W.M. Lu, T. Venkatesan, Ariando, Dominant role of oxygen vacancies in electrical properties of unannealed LaAlO3/SrTiO3 interfaces, J. Appl. Phys., 115 (2014) 054303.

[123] M.A. Kastner, R.J. Birgeneau, G. Shirane, Y. Endoh, Magnetic, transport, and optical properties of monolayer copper oxides, Rev. Mod. Phys., 70 (1998) 897-928.

[124] Z. Huang, X.R.S. Wang, Z.Q. Liu, W.M. Lu, S.W. Zeng, A. Annadi, W.L. Tan, X.P. Qiu, Y.L. Zhao, M. Salluzzo, J.M.D. Coey, T. Venkatesan, Ariando, Conducting channel at the LaAlO3/SrTiO3 interface, Phys. Rev. B, 88 (2013) 161107.

[125] M. Kawasaki, K. Takahashi, T. Maeda, R. Tsuchiya, M. Shinohara, O. Ishiyama, T. Yonezawa, M. Yoshimoto, H. Koinuma, ATOMIC CONTROL OF THE SRTIO3 CRYSTAL-SURFACE, Science, 266 (1994) 1540-1542.

[126] R. Dirsyte, J. Schwarzkopf, G. Wagner, R. Fornari, J. Lienemann, M. Busch, H. Winter, Thermal-induced change in surface termination of DyScO3(110), Surface Science, 604 (2010) L55-L58.

[127] J.E. Kleibeuker, B. Kuiper, S. Harkema, D.H.A. Blank, G. Koster, G. Rijnders, P. Tinnemans, E. Vlieg, P.B. Rossen, W. Siemons, G. Portale, J. Ravichandran, J.M. Szepieniec, R. Ramesh, Structure of singly terminated polar DyScO3 (110) surfaces, Phys. Rev. B, 85 (2012) 165413.

[128] T. Ohnishi, K. Takahashi, M. Nakamura, M. Kawasaki, M. Yoshimoto, H. Koinuma, A-site layer terminated perovskite substrate: NdGaO3, Applied Physics Letters, 74 (1999) 2531-2533.

[129] R. Dirsyte, J. Schwarzkopf, G. Wagner, J. Lienemann, M. Busch, H. Winter, R. Fornari, Surface termination of the NdGaO3(110), Applied Surface Science, 255 (2009) 8685-8687.

[130] J.H. Ngai, T.C. Schwendemann, A.E. Walker, Y. Segal, F.J. Walker, E.I. Altman, C.H. Ahn, Achieving A-Site Termination on La0.18Sr0.82Al0.59Ta0.41O3 Substrates, Adv. Mater., 22 (2010) 2945.

[131] X.S. Wu, J. Gao, The influence of La substitution for Ba in YBa2Cu3Oy cuprates, Physica C, 315 (1999) 215-222.

[132] R.J. Cava, B. Batlogg, R.M. Fleming, S.A. Sunshine, A. Ramirez, E.A. Rietman, S.M. Zahurak, R.B. Vandover, BA2-XLAXYCU3O7+/-DELTA PEROVSKITE COMPOUNDS - CRYSTAL-CHEMISTRY, Phys. Rev. B, 37 (1988) 5912-5915.

[133] A. Knizhnik, G.M. Reisner, Y. Eckstein, 1 : 2 : 3 superconductors (MxLa1-x)(LauBa1-u)(2)Cu3Oy with M = Ca or Y: lattice constants and T-c, Supercond. Sci. Technol., 17 (2004) 1077-1081.

[134] P. Karen, H. Fjellvag, A. Kjekshus, A.F. Andresen, LANTHANUM SUBSTITUTION FOR BARIUM IN YBA2CU3O9-DELTA, J. Solid State Chem., 93 (1991) 163-172.

[135] K. Segawa, Y. Ando, Doping n-type carriers by La substitution for Ba in the YBa2Cu3Oy system, Phys. Rev. B, 74 (2006) 100508.

[136] K. Segawa, M. Kofu, S.H. Lee, I. Tsukada, H. Hiraka, M. Fujita, S. Chang, K. Yamada, Y. Ando, Zero-doping state and electron-hole asymmetry in an ambipolar cuprate, Nature Physics, 6 (2010) 579-583.

[137] T. Nojima, H. Tada, S. Nakamura, N. Kobayashi, H. Shimotani, Y. Iwasa, Hole reduction and electron accumulation in YBa(2)Cu(3)O(y) thin films using an electrochemical technique: Evidence for an n-type metallic state, Phys. Rev. B, 84 (2011) 020502.

[138] Y. Ando, Mott Limit in High-Tc Cuprates, Springer, Berlin, (2007).

[139] V.J. Emery, S.A. Kivelson, SUPERCONDUCTIVITY IN BAD METALS, Phys. Rev. Lett., 74 (1995) 3253-3256.

[140] Y. Ando, A.N. Lavrov, S. Komiya, K. Segawa, X.F. Sun, Mobility of the doped holes and the antiferromagnetic correlations in underdoped high-T-c cuprates, Phys. Rev. Lett., 87 (2001) 017001.

[141] N.E. Hussey, K. Takenaka, H. Takagi, Universality of the Mott-Ioffe-Regel limit in metals, Philosophical Magazine, 84 (2004) 2847-2864.

[142] N.A. Babushkina, L.M. Belova, A.P. Zhernov, Role of the magnetic scattering in the quadratic temperature dependence of Nd2-xCexCuO4-delta films in normal state, Physica C, 282 (1997) 1163-1164.

[143] K. Jin, N.P. Butch, K. Kirshenbaum, J. Paglione, R.L. Greene, Link between spin fluctuations and electron pairing in copper oxide superconductors, Nature, 476 (2011) 73-75.

[144] Y. Onose, Y. Taguchi, K. Ishizaka, Y. Tokura, Charge dynamics in underdoped Nd(2-x)Ce(x)CuO(4): Pseudogap and related phenomena, Phys. Rev. B, 69 (2004) 024504.

[145] Y. Onose, Y. Taguchi, K. Ishizaka, Y. Tokura, Doping dependence of pseudogap and related charge dynamics in Nd(2-x)Ce(x)CuO4, Phys. Rev. Lett., 87 (2001) 217001.

[146] M. Ikeda, M. Takizawa, T. Yoshida, A. Fujimori, K. Segawa, Y. Ando, Chemical potential jump between the hole-doped and electron-doped sides of ambipolar high-T(c) cuprate superconductors, Phys. Rev. B, 82 (2010) 020503.

[147] P. Fournier, J. Higgins, H. Balci, E. Maiser, C.J. Lobb, R.L. Greene, Anomalous saturation of the phase coherence length in underdoped Pr2-xCexCuO4 thin films, Phys. Rev. B, 62 (2000) 11993-11996.

[148] S.J. Hagen, X.Q. Xu, W. Jiang, J.L. Peng, Z.Y. Li, R.L. Greene, TRANSPORT AND LOCALIZATION IN ND2-XCEXCUO4-Y CRYSTALS AT LOW DOPING, Phys. Rev. B, 45 (1992) 515-518.

[149] Y. Dagan, M.C. Barr, W.M. Fisher, R. Beck, T. Dhakal, A. Biswas, R.L. Greene, Origin of the anomalous low temperature upturn in the resistivity of the electron-doped cuprate superconductors, Phys. Rev. Lett., 94 (2005) 057005.

[150] W.H. Tang, J. Gao, Influence of Nd at Ba-sites on superconductivity of YBa2-xNdxCu3Oy, Physica C, 298 (1998) 66-72.

[151] H. Eisaki, N. Kaneko, D.L. Feng, A. Damascelli, P.K. Mang, K.M. Shen, Z.X. Shen, M. Greven, Effect of chemical inhomogeneity in bismuth-based copper oxide superconductors, Phys. Rev. B, 69 (2004) 064512.

[152] H.J. Kang, P. Dai, B.J. Campbell, P.J. Chupas, S. Rosenkranz, P.L. Lee, Q. Huang, S. Li, S. Komiya, Y. Ando, Microscopic annealing process and its impact on superconductivity in T '-structure electron-doped copper oxides, Nature Materials, 6 (2007) 224-229.

[153] P.H. Hor, R.L. Meng, Y.Q. Wang, L. Gao, Z.J. Huang, J. Bechtold, K. Forster, C.W. Chu, SUPERCONDUCTIVITY ABOVE 90 K IN THE SQUARE-PLANAR COMPOUND SYSTEM ABA2CU3O6+X WITH A = Y, LA, ND, SM, EU, GD, HO, ER, AND LU, Phys. Rev. Lett., 58 (1987) 1891-1894.

[154] D.W. Murphy, S. Sunshine, R.B. Vandover, R.J. Cava, B. Batlogg, S.M. Zahurak, L.F. Schneemeyer, NEW SUPERCONDUCTING CUPRATE PEROVSKITES, Phys. Rev. Lett., 58 (1987) 1888-1890.

[155] J.M. Tarascon, W.R. McKinnon, L.H. Greene, G.W. Hull, E.M. Vogel, OXYGEN AND RARE-EARTH DOPING OF THE 90-K SUPERCONDUCTING PEROVSKITE YBA2CU3O7-X, Phys. Rev. B, 36 (1987) 226-234.

[156] L. Soderholm, K. Zhang, D.G. Hinks, M.A. Beno, J.D. Jorgensen, C.U. Segre, I.K. Schuller, INCORPORATION OF PR IN YBA2CU3O7-DELTA - ELECTRONIC EFFECTS ON SUPERCONDUCTIVITY, Nature, 328 (1987) 604-605.

[157] C.R. Fincher, G.B. Blanchet, CE AND TB SUBSTITUTION FOR Y IN YBA2CU3O7 THIN-FILMS, Phys. Rev. Lett., 67 (1991) 2902-2905.

[158] A. Kebede, C.S. Jee, J. Schwegler, J.E. Crow, T. Mihalisin, G.H. Myer, R.E. Salomon, P. Schlottmann, M.V. Kuric, S.H. Bloom, R.P. Guertin, MAGNETIC-ORDERING AND SUPERCONDUCTIVITY IN Y1-XPRXBA2CU3O7-Y, Phys. Rev. B, 40 (1989) 4453-4462.

[159] M. Akhavan, The question of Pr in HTSC, Physica B, 321 (2002) 265-282.

[160] J.J. Neumeier, T. Bjornholm, M.B. Maple, I.K. Schuller, HOLE FILLING AND PAIR BREAKING BY PR IONS IN YBA2CU3O6.95+/-0.02, Phys. Rev. Lett., 63 (1989) 2516-2519.

[161] K. Segawa, Y. Ando, Intrinsic Hall response of the CuO2 planes in a chain-plane composite system of YBa2Cu3Oy, Phys. Rev. B, 69 (2004) 104521.

[162] D. Matthey, N. Reyren, J.M. Triscone, T. Schneider, Electric-field-effect modulation of the transition temperature, mobile carrier density, and in-plane penetration depth of NdBa2Cu3O7-delta thin films, Phys. Rev. Lett., 98 (2007) 057002.

[163] A.S. Dhoot, S.C. Wimbush, T. Benseman, J.L. MacManus-Driscoll, J.R. Cooper, R.H. Friend, Increased T-c in Electrolyte-Gated Cuprates, Adv. Mater., 22 (2010) 2529-2533.

[164] S. Smadici, J.C.T. Lee, S. Wang, P. Abbamonte, G. Logvenov, A. Gozar, C.D. Cavellin, I. Bozovic, Superconducting Transition at 38 K in Insulating-Overdoped La2CuO4-La1.64Sr0.36CuO4 Superlattices: Evidence for Interface Electronic Redistribution from Resonant Soft X-Ray Scattering, Phys. Rev. Lett., 102 (2009) 107004.

[165] J.L. Peng, E. Maiser, T. Venkatesan, R.L. Greene, G. Czjzek, Concentration range for superconductivity in high-quality Pr2-xCexCuO4-y thin films, Phys. Rev. B, 55 (1997) R6145-R6148.

[166] W. Jiang, S.N. Mao, X.X. Xi, X.G. Jiang, J.L. Peng, T. Venkatesan, C.J. Lobb, R.L. Greene, ANOMALOUS TRANSPORT-PROPERTIES IN SUPERCONDUCTING ND1.85CE0.15CUO4+/-DELTA, Phys. Rev. Lett., 73 (1994) 1291-1294.

[167] Y. Lee, C. Clement, J. Hellerstedt, J. Kinney, L. Kinnischtzke, X. Leng, S.D. Snyder, A.M. Goldman, Phase Diagram of Electrostatically Doped SrTiO3, Phys. Rev. Lett., 106 (2011) 136809.

[168] D.H. Lee, Z.Q. Wang, S. Kivelson, QUANTUM PERCOLATION AND PLATEAU TRANSITIONS IN THE QUANTUM HALL-EFFECT, Phys. Rev. Lett., 70 (1993) 4130-4133.

[169] Y. Dubi, Y. Meir, Y. Avishai, Unifying model for several classes of two-dimensional phase transition, Phys. Rev. Lett., 94 (2005) 156406.

[170] A. Kussmaul, J.S. Moodera, P.M. Tedrow, A. Gupta, 2-DIMENSIONAL CHARACTER OF THE MAGNETORESISTANCE IN ND1.85CE0.15CUO4-DELTA THIN-FILMS, Physica C, 177 (1991) 415-420.

[171] L. Li, J.G. Checkelsky, S. Komiya, Y. Ando, N.P. Ong, Low-temperature vortex liquid in La2-xSrxCuO4, Nature Physics, 3 (2007) 311-314.

[172] T. Valla, A.V. Fedorov, J. Lee, J.C. Davis, G.D. Gu, The ground state of the pseudogap in cuprate superconductors, Science, 314 (2006) 1914-1916.

[173] V.J. Emery, S.A. Kivelson, IMPORTANCE OF PHASE FLUCTUATIONS IN SUPERCONDUCTORS WITH SMALL SUPERFLUID DENSITY, Nature, 374 (1995) 434-437.

[174] S. Dukan, Z. Tesanovic, SUPERCONDUCTIVITY IN A HIGH MAGNETIC-FIELD - EXCITATION SPECTRUM AND TUNNELING PROPERTIES, Phys. Rev. B, 49 (1994) 13017-13023.

[175] M. Hosoda, Y. Hikita, H.Y. Hwang, C. Bell, Transistor operation and mobility enhancement in top-gated LaAlO3/SrTiO3 heterostructures, Applied Physics Letters, 103 (2013) 103507.

[176] P.D. Eerkes, W.G. van der Wiel, H. Hilgenkamp, Modulation of conductance and superconductivity by top-gating in LaAlO3/SrTiO3 2-dimensional electron systems, Applied Physics Letters, 103 (2013) 201603.

[177] B. Forg, C. Richter, J. Mannhart, Field-effect devices utilizing LaAlO3-SrTiO3 interfaces, Applied Physics Letters, 100 (2012) 053506.

[178] V.T. Tra, J.W. Chen, P.C. Huang, B.C. Huang, Y. Cao, C.H. Yeh, H.J. Liu, E.A. Eliseev, A.N. Morozovska, J.Y. Lin, Y.C. Chen, M.W. Chu, P.W. Chiu, Y.P. Chiu, L.Q. Chen, C.L. Wu, Y.H. Chu, Ferroelectric Control of the Conduction at the LaAlO3/SrTiO3 Heterointerface, Adv. Mater., 25 (2013) 3357-3364.

[179] W.N. Lin, J.F. Ding, S.X. Wu, Y.F. Li, J. Lourembam, S. Shannigrahi, S.J. Wang, T. Wu, Electrostatic Modulation of LaAlO3 /SrTiO3 Interface Transport in an Electric Double-Layer Transistor, Advanced Materials Interfaces, 1 (2013) 1-7.

[180] Y.J. Shi, S. Wang, Y. Zhou, H.F. Ding, D. Wu, Tuning the carrier density of LaAlO3/SrTiO3 interfaces by capping La1-xSrxMnO3, Applied Physics Letters, 102 (2013) 071605.

[181] M. Huijben, G. Koster, M.K. Kruize, S. Wenderich, J. Verbeeck, S. Bals, E. Slooten, B. Shi, H.J.A. Molegraaf, J.E. Kleibeuker, S. van Aert, J.B. Goedkoop, A. Brinkman, D.H.A. Blank, M.S. Golden, G. van Tendeloo, H. Hilgenkamp, G. Rijnders, Defect Engineering in Oxide Heterostructures by Enhanced Oxygen Surface Exchange, Advanced Functional Materials, 23 (2013) 5240-5248.

[182] Y.W. Xie, Y. Hikita, C. Bell, H.Y. Hwang, Control of electronic conduction at an oxide heterointerface using surface polar adsorbates, Nature Communications, 2 (2011) 494.

[183] K. Au, D.F. Li, N.Y. Chan, J.Y. Dai, Polar Liquid Molecule Induced Transport Property Modulation at LaAlO3/SrTiO3 Heterointerface, Adv. Mater., 24 (2012) 2598-2602.

[184] H.L. Lu, Z.M. Liao, L. Zhang, W.T. Yuan, Y. Wang, X.M. Ma, D.P. Yu, Reversible insulator-metal transition of LaAlO3/SrTiO3 interface for nonvolatile memory, Scientific Reports, 3 (2013) 2870.

[185] C. Cen, S. Thiel, G. Hammerl, C.W. Schneider, K.E. Andersen, C.S. Hellberg, J. Mannhart, J. Levy, Nanoscale control of an interfacial metal-insulator transition at room temperature, Nature Materials, 7 (2008) 298-302.

[186] C. Cen, S. Thiel, J. Mannhart, J. Levy, Oxide Nanoelectronics on Demand, Science, 323 (2009) 1026-1030.

[187] A. Ron, Y. Dagan, One-Dimensional Quantum Wire Formed at the Boundary between Two Insulating LaAlO3/SrTiO3 Interfaces, Phys. Rev. Lett., 112 (2014) 136801.

[188] C.W. Schneider, S. Thiel, G. Hammerl, C. Richter, J. Mannhart, Microlithography of electron gases formed at interfaces in oxide heterostructures, Applied Physics Letters, 89 (2006) 122101.

[189] N. Banerjee, M. Huijben, G. Koster, G. Rijnders, Direct patterning of functional interfaces in oxide heterostructures, Applied Physics Letters, 100 (2012) 041601.

[190] P.P. Aurino, A. Kalabukhov, N. Tuzla, E. Olsson, T. Claeson, D. Winkler, Nano-patterning of the electron gas at the LaAlO3/SrTiO3 interface using low-energy ion beam irradiation, Applied Physics Letters, 102 (2013) 201610.

[191] R. Pentcheva, W.E. Pickett, Avoiding the Polarization Catastrophe in LaAlO3 Overlayers on SrTiO3(001) through Polar Distortion, Phys. Rev. Lett., 102 (2009) 107602.

[192] K. Shibuya, T. Ohnishi, M. Lippmaa, M. Kawasaki, H. Koinuma, Single crystal SrTiO3 field-effect transistor with an atomically flat amorphous CaHfO3 gate insulator, Applied Physics Letters, 85 (2004) 425-427.

[193] Z.Q. Liu, D.P. Leusink, X. Wang, W.M. Lu, K. Gopinadhan, A. Annadi, Y.L. Zhao, X.H. Huang, S.W. Zeng, Z. Huang, A. Srivastava, S. Dhar, T. Venkatesan, Ariando, Metal-Insulator Transition in SrTiO3-x Thin Films Induced by Frozen-Out Carriers, Phys. Rev. Lett., 107 (2011) 146802.

[194] M. Huijben, G. Rijnders, D.H.A. Blank, S. Bals, S. Van Aert, J. Verbeeck, G. Van Tendeloo, A. Brinkman, H. Hilgenkamp, Electronically coupled complementary interfaces between perovskite band insulators, Nature Materials, 5 (2006) 556-560.

[195] J.S. Kim, S.S.A. Seo, M.F. Chisholm, R.K. Kremer, H.U. Habermeier, B. Keimer, H.N. Lee, Nonlinear Hall effect and multichannel conduction in LaTiO3/SrTiO3 superlattices, Phys. Rev. B, 82 (2010) 201407.

[196] R. Ohtsuka, M. Matvejeff, K. Nishio, R. Takahashi, M. Lippmaa, Transport properties of LaTiO3/SrTiO3 heterostructures, Applied Physics Letters, 96 (2010) 192111.